NKS-370
ISBN 978-87-7893-455-0

Experimental and Analytical Investigations of Debris Bed Formation, Spreading, Coolability, and Steam Explosion in Nordic BWRs

Pavel Kudinov[1]
Alexander Konovalenko[1]
Dmitry Grishchenko[1]
Sergey Yakush[2]
Simone Basso[1]
Nazar Lubchenko[3]
Aram Karbojian[1]

[1]Division of Nuclear Power Safety (NPS) Royal Institute of Technology (KTH)
Stockholm, Sweden
[2]Institute for Problems in Mechanics of the Russian Academy of Sciences
Moscow, Russia
[3]Massachusetts Institute of Technology
Cambridge, Massachusetts, USA

June 2016

Abstract

In case of severe accident in Nordic type BWRs core melt is fragmented in a deep water pool. There is uncertainty if formed bed if core debris will be coolable or if energetic steam explosion can threaten containment integrity. The goal of the project is to reduce uncertainties in debris coolability and steam explosion impact.

DECOSIM code has been developed for analysis of porous debris coolability and further validated against COOLOCE data. Debris bed cooling in post-dryout regime was addressed. Analytical models for prediction of the maximum temperature of the debris and relative size of the dry zone as a function of overheating parameter is proposed and validated against DECOSIM simulations. DECOSIM code was extended to in-vessel coolability analysis. The parameter ranges corresponding to coolable and non-coolable configurations were obtained for initially dry and quenched debris configuration.

Scaling approach and universal semi-empirical closure have been developed for prediction of particulate debris spreading using PDS-C tests. The approach has been validated against experimental data with different particle mixtures. The model for prediction of particulate debris spreading was implemented in the DECOSIM code.

An approach for analysis of steam explosion in Nordic BWR and sensitivity of steam explosion impulse to the uncertain modeling and scenario parameters has been proposed. TEXAS-V code is used for analysis. Obtained database of impulses TEXAS is used for development of a computationally efficient surrogate model that can be used in extensive uncertainty analysis.

Key words

Nordic BWR, severe accident, debris bed formation, coolability, steam explosion

NKS-370
ISBN 978-87-7893-455-0
Electronic report, Junu 2016
NKS Secretariat
P.O. Box 49
DK - 4000 Roskilde, Denmark
Phone +45 4677 4041
www.nks.org
e-mail nks@nks.org

Experimental and Analytical Investigations of Debris Bed Formation, Spreading, Coolability, and Steam Explosion in Nordic BWRs

Final Report from the NKS-R DECOSE activity

(Contract: NKS_R_2012_100)

Pavel Kudinov[1], *Alexander Konovalenko*[1], *Dmitry Grishchenko*[1], *Sergey Yakush*[2], *Simone Basso*[1], *Nazar Lubchenko*[3], *Aram Karbojian*[1]

[1]Division of Nuclear Power Safety (NPS), Royal Institute of Technology (KTH), Stockholm

[2]Institute for Problems in Mechanics of the Russian Academy of Sciences, Moscow, Russia

[3]Massachusetts Institute of Technology, Cambridge, Massachusetts, USA

June, 2016
Stockholm

Contents

List of Figures

List of Tables

Executive Summary

Assessment of effectiveness of severe accident management strategy adopted in Nordic type BWRs is main motivation of this work. It is assumed that core melt ejected from the vessel will fragment, quench and form a coolable debris bed in a deep water pool below the vessel. However, there is a risk that formed debris bed will not be coolable. It is also possible that energetic steam explosion will occurs in the process of melt fragmentation in the pool. The goal of the project is to reduce uncertainties in assessment of (i) debris bed properties and coolability, (ii) steam explosion impact.

DECOSIM code has been developed for analysis of porous debris coolability. DECOSIM was further validated against COOLOCE data for different configurations: (i) cylindrical debris bed with open side walls (COOLOCE-10), (ii) conical bed on a cylindrical base (COOLOCE-12). The code was further developed to address debris bed cooling in post-dryout regime. An analytical model for prediction of the maximum temperature of the debris for the known size of the dry zone is proposed based on the analysis of DECOSIM calculations. Also, a model describing the relative size of the dry zone as a function of overheating parameter is proposed and validated against DECOSIM simulations. Good agreement of both analytical models with the DECOSIM data is demonstrated.

DECOSIM code was extended to in-vessel problems by implementing models for complex geometries, as well as taking into account the effect of congesting structures available in the lower plenum (CRGTs and IGTs). Simulations of initially quenched and initially dry debris beds were carried out, the parameter ranges corresponding to coolable and non-coolable configurations were obtained. Development of dryout and subsequent reheating and remelting of solid material is studied.

Boiling and two-phase flow inside the bed is a source of mechanical energy which can help to spread the debris bed by so called “self-leveling” phenomenon. However, to be effective in providing a coolable geometrical configuration, self-leveling time scale has to be smaller than the time scale for drying out and onset of re-melting of the bed. In this work a new scaling approach for particulate debris spreading has been proposed. Based on the scaling and on the PDS-C experimental data a universal semi-empirical closure has been developed for prediction of particulate debris spreading. Validity of the closure for arbitrary shaped and

multi-size particles to be confirmed in the future PDS-C tests. The model for prediction of particulate debris spreading was implemented in the DECOSIM code allowing calculations of the debris bed spreading phenomena with possible feedbacks between dryout and spreading effectiveness.

In this work we also develop an approach for analysis of steam explosion in Nordic BWR and sensitivity of steam explosion impulse to the uncertain modeling and scenario parameters. TEXAS-V code is used for analysis. First results indicate that the most influential parameters are triggering time, jet diameter, and melt release velocity. More work is necessary for selection and justification of the parameter ranges and clarification of their potential inter-dependencies. Obtained database of impulse and pressure as a function of the TEXAS input parameters is used for development of a computationally efficient surrogate model that can be used in extensive uncertainty analysis. Further work is necessary for refinement of the surrogate model and development of a robust approach to identification and classification of the failure domains in multidimensional space of input parameters.

1 Motivation

In this work we continue research work which was presented in the previous NKS reports [38], [39], [40]. The project is motivated by Severe Accident (SA) Mitigation Strategy adopted in several designs of light water reactors (LWR) and specifically in Nordic type BWRs. The LWR SA management strategy considered hereafter is based on ex-vessel melt coolability in the reactor cavity filled up with water. It is assumed in the design that, in case of severe core melt accident, reactor pressure vessel (RPV) lower head can fail and molten core materials (corium) can be poured into a several meters deep reactor cavity filled with water. It is assumed further that decay heat can be removed from the debris bed by natural circulation. However, coolability of such bed is contingent upon the properties of the debris bed, such as particle size distribution, porosity and geometrical configuration of the bed. A tall, mound shape debris bed can be hardly coolable, while the same mass of the debris can be easily cooled if the bed is spread uniformly over the area of the reactor cavity [76], [73].

Generally, the SA management strategy has to be proven robust (insensitive to scenarios and conditions of melt release from the vessel). Yet, there is apparent significant influence of the accident scenario on the success of the SA management strategy. Specifically, melt release mode defines conditions and effectiveness of melt fragmentation, spreading and thus coolability. There are several characteristic modes of vessel failure and melt release that might result in completely different ex-vessel melt configurations. It is instructive to note that even within one scenario of accident progression the melt is expected to be released in more than one shot with different (a) sizes of the vessel breach, (b) different melt compositions (oxidic or metallic), (c) melt superheats. Respective configuration of the debris bed can be completely fragmented particles (small vessel breach, small superheat of the melt), mixture of liquid and solid particles promoting formation of non-coolable “cakes” (medium size breach) and mostly liquid melt (large size breach, large melt superheat). A prove of the robustness of the management strategy implies systematic and consistent analysis of different scenarios of melt release modes, their consequences for the ex-vessel melt arrest and coolability and associated epistemic and aleatory uncertainties. It is expected that some melt release scenarios will result in formation of non-coolable debris configurations threatening containment integrity.

2 Background Motivation and Goals

Although the strategy of melt quenching in a pool is known for decades and has been a subject for intensive research since ’80s, the main questions persist: whether or not decay heated porous debris bed can be cooled by natural circulation in the reactor cavity pool; and is there a threat to containment integrity due to energetic steam explosion, which can occur during melt pouring into water.

The APRI (Accident Phenomena of Risk Importance) research program was initiated at the Royal Institute of Technology (KTH) to help bring to the resolution the long standing severe accident issues: ex-vessel coolability and steam explosion for the Swedish-type BWRs. Advanced experimental infrastructure for tests with high melting temperature core melt simulant materials was developed at the division of Nuclear Power Safety (NPS) during last two decades with continuous support from Swedish nuclear power utility and safety authority. The focus of the previous APRI-7 (2009-2011) and current APRI-8,9 (2012-2017) at NPS-KTH is development of understanding and predictive capabilities for the debris bed formation and coolability phenomena in the process of melt pouring into coolant. In APRI-9 the focus is on the application of Risk Oriented Accident Analysis Methodology (ROAAM) that marries probabilistic and deterministic approaches. This methodology developed by Professor Theofanous [65] has been applied to successfully resolve different severe accident issues in existing light water reactor (LWR) plants, and development of severe accident strategies in advanced LWR designs [66]. When applied to the Nordic BWR plants, the tight coupling between severe accident threats (steam explosion and basemat melt-through due to debris un-coolability) and high sensitivity of the SAM effectiveness to timing of event (e.g., vessel failure) and characteristics (e.g., melt release conditions) present new challenges in decomposition, analysis and integration. Therefore further development of the methodology called ROAAM+ was undertaken [31]. The aim of ROAAM+ is to develop full models for detailed analysis of severe accident phenomena and surrogate models for extensive uncertainty and risk analysis.

The research program on debris bed formation (DEFOR) carried out in the framework of APRI projects includes experimental studies [32], [33], [34], [18], [35], [37], [17], [38], [42], [43], [6], [36] in the DEFOR facility and comprehensive analytical research [69], [38], [41], [10], [29], [26], [68], [71], [27], [70], [11], [30], [43], [44], [14], [28]. Sophisticated

experimental techniques and multiphysics computational approaches were developed over the last years to understand and model the process of particle bed formation when a melt jet is released in a pool of water. The pool depth and water subcooling can be varied and so can be the melt jet height and the volume discharged into the water pool. The melt materials and compositions employed can be varied also, e.g. ceramic and glass type melts at temperatures up to 1500°C with different melt viscosities can be employed.

Particulate debris spreading is important element of DEFOR program on debris bed formation phenomena that can affects the shape of the bed and thus its coolability. Experiments on particulate debris spreading (PDS) due to self levelling and during sedimentation in the pool (PDS-P) have been developed at KTH. The goal of the test (PDS-C) is to provide data for development and validation of the models that can be applied for analysis of debris spreading in prototypic accident conditions.

COOLOCE facility at VTT [61], [62] has been used in the past for analysis of debris bed coolability. As a pool type facility, it can be used not only for analysis of coolability of different 2D and 3D geometries of the debris bed.

DECOSIM is a thermo-hydraulic code developed at KTH for simulation of debris bed formation and coolability [68], [69], [38]. In the framework of this work, validation of DECOSIM code is being performed against the COOLOCE data. The work is concerned with further development of the code for prediction of (i) debris coolability in post-dryout regime, and (ii) debris bed spreading.

3 DECOSIM Code Development and Validation.

3.1 Overview of DECOSIM Code

DECOSIM is a thermohydraulic code being developed at KTH for simulation of debris bed formation and coolability [68], [69], [38]. In the framework of DECOSE project, validation of DECOSIM code is being performed against the existing COOLOCE data.

DECOSIM has been developed to take into account not only the flows in the porous medium, but also natural convection flows in the pool, where turbulence models and discrete particle models apply [70], [71]. In this work, only a subset of all models was used: the space beyond the debris bed was filled with an artificial porous medium with low drag, so that the flow in the whole computational domain was calculated from the filtration equations. Also, saturated conditions are assumed in the debris bed and above it, so that the governing equations to be solved are the continuity equations for each phase.

Under the assumption of saturated conditions, the criterion employed to detect the local dryout is based on the analysis of the void fraction distribution, rather than the temperature field. A special algorithm for finding the dryout boundary has been developed and implemented in DECOSIM. For each given shape and properties of the debris bed (input parameters), a set of calculations was carried out in which the specific heat power released in the porous material was varied. First, two values of the specific heat power were set by the user, the higher of which results in the dryout, and the lower of which corresponds to steady-state cooling (no dryout). Then, the next value of the specific heat power was taken as the arithmetic mean of the two powers, and simulation was run with this new power to find out if dryout occurs or now. Depending on the outcome of the simulation, either the lower, or the upper boundary of the heat power interval was set to the last heat power, and the procedure was repeated. This algorithm is similar to the well-known bisection algorithm for finding the root of a function, the iterations are repeated until the upper and lower boundaries of the interval become close enough (i.e., their difference become smaller than some prescribed tolerance).

To speed up calculations, the intermediate solutions were not run to convergence; rather, empirical rules based on the observations of the behavior of the maximum void fraction in the debris bed were formulated and implemented in the code to decide if dryout is going to occur or not. This enabled the dryout boundary to be found much more efficiently than in the original version of the algorithm where all intermediate solutions were run to convergence.

It should be noted that the capability to solve the energy equations for the liquid and gas phases has been recently implemented in DECOSIM, together with the solver for heat transfer in the solid phase. These new capabilities will be utilized in the further validation studies, including the simulations of debris bed coolability in an initially subcooled water pool.

3.2 Governing Equations and Numerical Solver

Consider a debris bed submerged in a water pool. Transient distributions are sought for the volume fractions α_i, superficial velocities $\mathbf{j}_i$ of liquid and gas phases (subscripts *L* and *G*, respectively), and pressure P.

The phase continuity and momentum equations are

$$\frac{\partial \rho_G \alpha_G}{\partial t} + \nabla\left(\rho_G \mathbf{j}_G\right) = \Gamma, \qquad \frac{\partial \rho_L \alpha_L}{\partial t} + \nabla\left(\rho_L \mathbf{j}_L\right) = -\Gamma \tag{3.1}$$

$$-\nabla P + \rho_G \mathbf{g} = \frac{\mu_G}{K K_{rG}} \mathbf{j}_G + \frac{\rho_G}{\eta \eta_{rG}} |\mathbf{j}_G| \mathbf{j}_G \tag{3.2}$$

$$-\nabla P + \rho_L \mathbf{g} = \frac{\mu_L}{K K_{rL}} \mathbf{j}_L + \frac{\rho_L}{\eta \eta_{rL}} |\mathbf{j}_L| \mathbf{j}_L \tag{3.3}$$

Here, $\mathbf{g}$ is the gravity acceleration, ρ_i and μ_i are the densities and viscosities of the liquid and gas phases ($i = L, G$). The right-hand sides of Eqs. (3.2) and (3.3) contain the phase drag due to porous medium with linear and quadratic terms (with the absolute, K, η, and relative, K_{ri}, η_{ri}, permeabilities and possibilities). Commonly, saturated conditions are assumed in the debris bed, with the volumetric evaporation rate being $\Gamma = Q / \Delta H_{ev}$, where Q is the heat release rate per unit volume of debris bed, ΔH_{ev} is the latent heat of evaporation (i.e., decay heat goes to water evaporation). Under this assumption, the fluid properties ρ_i and μ_i are

functions of the pressure P. The properties of water in liquid and vapor states (densities ρ_i, enthalpies h_i, viscosities μ_i, thermal conductivities λ_i) as functions of pressure and temperature are implemented as polynomials according to IAPWS-IF97 formulation ("Steam tables") [15].

The drag force due to solid debris (see the first and second terms on the right-hand sides of Eqs. (3.3) is characterized by the permeability K and passability η depending on the properties of the porous medium. For monodisperse spherical particles, these are related to the porosity ε and particle diameter *d* [12]:

$$K = \frac{\varepsilon^3 d^2}{150(1-\varepsilon)^2}, \qquad \eta = \frac{\varepsilon^3 d}{1.75(1-\varepsilon)} \tag{3.4}$$

These relations can also be used for particles of arbitrary shapes, provided that d is substituted by a properly averaged effective mean particle diameter. The relative permeabilities K_{ri} and passabilities η_{ri} are functions of the void fraction α, they are commonly described by power-law relations:

$$\begin{aligned} K_{rL} &= (1-\alpha)^{nL}, \quad \eta_{rL} = (1-\alpha)^{mL} \\ K_{rG} &= \alpha^{nG}, \qquad \eta_{rG} = \alpha^{mG} \end{aligned} \tag{3.5}$$

In Reed's model [48], the interphase drag is neglected, the exponents in the relative permeabilities are $nL = nG = 3$, and those in the relative passabilities are $mL = mG = 5$.

In order to be able to calculate the post-dryout state of debris bed, full energy formulation must be employed, rather than the model of saturated water-vapor mixture which is sufficient for modelling the pre-dryout stage. Therefore, energy equations for the liquid and vapor phases, as well as for the solid particles of debris bed material were added to the model and implemented in DECOSIM. Namely, the energy equations are

$$\varepsilon\rho_i\alpha_i \frac{d_i h_i}{dt} = \varepsilon\alpha_i \frac{d_i P}{dt} + \nabla\left(\varepsilon\alpha_i\lambda_i\nabla T_i\right) + \Gamma_i\left(h_i^I - h_i\right) + \gamma_i\dot{Q}_{si} + \dot{Q}_i^I \tag{3.6}$$

$$(1-\varepsilon)\rho_s C_s \frac{\partial T_s}{\partial t} = \nabla\left(\lambda_{eff}\nabla T_s\right) + \dot{Q}_d - \dot{Q}_{sl} - \dot{Q}_{sv} \tag{3.7}$$

The evaporation rate $\Gamma = \Gamma_v = -\Gamma_l$ is determined by the heat balance at the interphase surface

$$\Gamma = -\frac{\dot{Q}_l^I + \dot{Q}_v^I + \dot{Q}_w^I}{h_v^I - h_l^I} \tag{3.8}$$

where the heat fluxes to the interface are

$$\dot{Q}_l^I = A\beta_l\left(T^I - T_l\right), \dot{Q}_v^I = A\beta_v\left(T^I - T_v\right), \dot{Q}_w^I = \left(1-\gamma_l\right)\dot{Q}_{sl} \tag{3.9}$$

where the interface temperature T^I is equal to the saturation temperature at the local pressure (pure vapor is assumed in the bubbles), i.e., $T^I = T_{sat}\left(P\right)$. The phase enthalpies at the interface are taken according to the direction of phase transition:

$$h_l^I = \begin{cases} h_l, & \Gamma > 0 \\ h_{l,sat}, & \Gamma \le 0 \end{cases}, \quad h_v^I = \begin{cases} h_v, & \Gamma < 0 \\ h_{v,sat}, & \Gamma \ge 0 \end{cases} \tag{3.10}$$

In the numerator of Eq. (3.8), Q_w^I is the heat flux from the solid particles which goes directly to the interface when the liquid becomes superheated. The fraction of heat from solid particles which goes to heating of liquid phase, γ_l, is assumed to vary linearly from 1 for saturated liquid to 0 when the liquid superheat reaches the maximum allowable value $\Delta T_{\max} = 5\,\mathrm{K}$:

$$\gamma_l = \begin{cases} 1, & T_l \le T_{sat} \\ \dfrac{T_l - T_{sat}}{\Delta T_{\max}}, & T_{sat} \le T_l \le T_{sat} + \Delta T_{\max} \\ 0, & T_l > T_{sat} + \Delta T_{\max} \end{cases} \tag{3.11}$$

In the bubble regime ($\alpha_v \le 0.3$), the specific interphase surface area and heat transfer coefficients for the liquid and vapor phases in Eq. (3.9) are evaluated from

$$\begin{aligned} A &= \varepsilon\frac{6\alpha_v}{D_b}, \quad \beta_l = \frac{\lambda_l}{D_b}\left(2 + 0.6\,\mathrm{Re}_{b,l}^{1/2}\,\mathrm{Pr}_l^{1/3}\right), \\ \beta_v &= 2\frac{\lambda_v}{D_b}, \quad \mathrm{Re}_{b,l} = \frac{\rho_l\left|U_l - U_v\right|D_b}{\mu_l} \end{aligned} \tag{3.12}$$

The bubble diameter D_b is evaluated from

$$D_b = 1.35\left(\frac{\sigma}{g\left(\rho_l - \rho_v\right)}\right)^{1/2} \tag{3.13}$$

The Reynolds number $\mathrm{Re}_{b,l}$ is based on the relative velocity magnitude and properties of the continuous phase (liquid).

For higher void fractions ($0.3 \le \alpha_v \le 1$), annular regime is assumed, with water being the wetting phase in direct contact with the solid particles, in which case the specific interface area and heat transfer coefficients are

$$A = \varepsilon \frac{4\alpha_v^{1/2}}{D_p}, \quad \beta_l = \frac{\mathrm{Nu}_l \lambda_l}{D_p}, \quad \beta_v = \frac{\mathrm{Nu}_v \lambda_v}{D_p} \tag{3.14}$$

The Nusselt numbers for the gas phase is calculated as $\mathrm{Nu}_v = 2 + 0.6\,\mathrm{Re}_r^{1/2}\,\mathrm{Pr}_v^{1/3}$, where Re_r is the Reynolds number based on the relative velocity of the phases. For the liquid, a constant Nusselt number $\mathrm{Nu}_l = 10$ is assumed.

The source terms $\dot{Q}_{si}$ describing heat transfer from the solid particles to the liquid and gas phases are evaluated as

$$\dot{Q}_{sl} = \chi \cdot A_s \beta_{sl} \left(T_s - T_l\right), \dot{Q}_{sv} = \left(1-\chi\right) \cdot A_s \beta_{sv} \left(T_s - T_v\right) \tag{3.15}$$

where A_s is the specific surface area of porous particles (per unit of total volume), β_{si} are the heat transfer coefficients for the liquid and vapor phases, respectively. It is assumed that, as long as the void fraction α_v is below the critical value $\alpha_{dry} \approx 0.95$, all particles are covered with liquid water, so that all heat is transferred only to the liquid phase ($Q_{sv} = 0$). For higher void fractions, some part of the particle surface becomes dry, and direct heating of vapor by particles commences. A simple linear ramping of the heat transfer coefficients is applied at $\alpha \ge \alpha_{dry}$, so that $Q_{sl} = 0$ at $\alpha_v = 1$ (this provides physically sound reduction to the case of single-phase vapor exchanging heat with the porous particles in the post-dryout conditions):

$$\chi = \min\left(\frac{1-\alpha}{1-\alpha_{dry}}, 1\right) \tag{3.16}$$

The specific surface area in Eq. (3.15) is $A_s = 6(1-\varepsilon)/D_p$, the vapor heat transfer coefficient is

$$\beta_{sv} = \frac{\lambda_v}{D_p}\left(2 + 0.6\,\mathrm{Re}_{p,v}^{1/2}\,\mathrm{Pr}_v^{1/3}\right), \quad \mathrm{Re}_{p,v} = \frac{\rho_v U_v D_p}{\mu_v} \tag{3.17}$$

The heat transfer coefficient between liquid and solid particles depends on the particle superheat with respect to the saturation temperature $T_s - T_{sat}$. When the wall temperature is

lower than T_s, the heat flux from particles to liquid is obtained from Eq. (3.15), with the heat transfer coefficient

$$\beta_{sl} = \frac{\lambda_l}{D_P}\left(2 + 0.6\,\mathrm{Re}_{p,l}^{1/2}\,\mathrm{Pr}_l^{1/3}\right) \tag{3.18}$$

When the wall temperature is above T_s, the heat flux is obtained from $\dot{Q}_{sl} = \chi \cdot A_s \beta_{sl}\left(T_s - T_{sat}\right)$ with the heat transfer coefficient depending on the boiling regime ("boiling curve"). Nucleate boiling occurs for superheats below the critical value $0 \le T_s - T_{sat} \le \Delta T_{nucl}$, the heat transfer coefficient is described by Rhosenow's correlation

$$\beta_{sl} = \mu_l \Lambda \left[\frac{g\left(\rho_l - \rho_v\right)}{\sigma}\right]^{1/2}\left[\frac{C_l}{C_{sf}\,\Lambda\,\mathrm{Pr}_l^{1.7}}\right]^3 \left(T_s - T_{sat}\right)^2 \tag{3.19}$$

where $\Lambda = h_{v,sat} - h_{l,sat}$, C_l is the specific heat capacity of liquid, while $C_{sf} = 0.006 - 0.013$ is a constant depending of the surface-fluid combination; in the calculations it was assumed that $C_{sf} = 0.01$.

For film boiling at high superheat, $T_s - T_{sat} \ge \Delta T_{film}$, Bromley's correlation is applied, with the convective heat transfer coefficient

$$\beta_{sl}^{conv} = 0.67\left[\frac{\lambda_v^3 \rho_v g\left(\rho_l - \rho_v\right)\left(\Lambda + 0.4 C_{pv}\left(T_s - T_{sat}\right)\right)}{D_p \mu_v \left(T_s - T_{sat}\right)}\right]^{1/4} \tag{3.20}$$

The radiative heat transfer coefficient becoming important at high debris temperature is

$$\beta_{sl}^{rad} = \varepsilon_p \sigma_{SB} \frac{T_s^4 - T_{sat}^4}{T_s - T_{sat}} \tag{3.21}$$

where ε_p is the particle surface emissivity, $\sigma_{SB} = 5.67 \cdot 10^{-8}$ W/m^{2}K^4 is the Stefan-Boltzmann constant. The total heat transfer coefficient β_{sl} is obtained from

$$\beta_{sl}^{4/3} = \left(\beta_{sl}^{conv}\right)^{4/3} + \beta_{sl}^{rad}\beta_{sl}^{1/3} \tag{3.22}$$

In the intermediate region $\Delta T_{nucl} \le T_s - T_{sat} \le \Delta T_{film}$, linear interpolation is performed between β_{sl} evaluated from Eq. (3.19) with $T_s - T_{sat} = \Delta T_{nucl}$, and β_{sl} obtained from Eqs. (3.20)–(3.22) with $T_s - T_{sat} = \Delta T_{film}$. The boundaries of the nucleate and film boiling regimes were set to $\Delta T_{nucl} = 20$ K and $\Delta T_{film} = 120$ K.

The decay heat power in the solid material energy equation (3.7) is expressed in terms of the specific decay heat power as $\dot{Q}_d = (1-\varepsilon)\rho_s W$. A simple model is employed for the effective heat conductivity of porous medium: $\lambda_{eff} = (1-\varepsilon)\lambda_s$.

In DECOSIM, all transport equations are discretized on a staggered orthogonal grid in the 2D axisymmetric geometry. On each time step, the momentum equations are solved first to find out the preliminary velocity components of each phase. The velocity corrections are expressed in terms of pressure and volume fraction corrections, with the phase change terms taken into account implicitly. They are then substituted into the phase continuity and energy equation which are solved in a fully coupled manner by an efficient ILUT-preconditioned PGMRES solver from SPARSKIT package. Global iterations are performed on each time step until convergence with prescribed accuracy is reached. The time step is varied adaptively, depending on convergence success or failure.

DECOSIM has been validated with respect to various separate effects, including two-phase drag in porous media and coolability of flat and axisymmetric (cone-shaped) ex-vessel debris beds in configurations. The models and closures involved are similar to those of WABE/MEWA code [7] with which some cross-code verifications have been carried out. At the moment, no reactor-scale experiments are available to enable integral validation of this (or similar) codes.

3.3 Search Algorithm for Determination of Coolability Boundary

To study the debris bed coolability, an algorithm for automatic search for the dryout boundary is required. A straightforward algorithm is the following: the heat release rate (HRR) is gradually increased with some step, and for each HRR transient simulation is run for a long enough time period. The minimum HRR causing the dryout is considered to be the boundary. The dryout criterion is based on the monitoring the void fraction in the debris bed. Dryout was detected if the void fraction in any cell of the grid reached the critical value (0.95–0.975), after that the heat release rate was ramped to zero because evaporation becomes inefficient for such high void fractions.

This approach has several drawbacks. Firstly, it requires long and useless calculations far from dryout, when the flow reaches the steady state. Secondly, it can miss the dryout HRR, since the time between the HRR increase and actual dryout can be very long, especially for a flat layer (see [15]). Thirdly, the accuracy of the dryout boundary detection is of the order of HRR step, and to increase the accuracy it is required to use smaller steps in HRR and, therefore, more simulations are required.

To improve the efficiency, an algorithm was proposed which makes possible an automatic search of the dryout boundary. Its main idea is to vary the HRR using the bisection algorithm and use certain semi-empirical criteria to determine whether the current state of the debris bed is likely to lead to steady state cooling, or to dryout. In what follows, the algorithm is described in detail.

The debris bed is initially filled with water in the saturated conditions. The heat released in the porous material causes the production of water vapor, which results in the development of water and vapor flows. The void fraction in the bed increases gradually, and, finally, two scenarios are possible: either the debris bed is coolable (steady-state conditions are attained), or dryout can occur at some point. Theoretically, the final state can only be checked in an infinitely long calculation (because the time to dryout can be quite long and is not known beforehand). To make the algorithm efficient, criteria were proposed for the following:

1. Convergence of all fields (velocities, pressure, volume fractions) in the debris bed to steady-state distributions with some tolerance.
2. The maximum void fraction in the debris bed.

These criteria were chosen as they are close to the physical meaning of steady-state cooling and dryout. Other criteria checked during the coolability simulations are the convergence of all fields on the whole grid, which happened to give almost the same results as that inside the bed, and the average void fraction.

After some trial runs, the following parameters were chosen for the search:

1. To check if the fields converged to some steady state, they were averaged over the last ten steps in order to reduce the effect of possible fluctuations of the numerical nature. The averaged values were compared every 10 seconds. Then, for each of the seven monitored variables the maximum change was found and normalized. For normalization, the pressure and volume fractions were divided by the maximum value of the corresponding field in the bed; the velocity components were divided by the absolute values of the superficial velocity vector. The highest value of the normalized increments was compared to the steady state criterion (SSC); if it happened to be lower than SSC, the debris bed was assumed to be in its steady state.

   The SSC was chosen after several runs on the test problems. It strongly depends on the time between criterion checks, since the larger is the time interval the smaller should be the criterion. It should be noted that high SSC (10^{-3} or higher) leads to significant misses of the dryout, especially for flat debris bed. Very low SSC (10^{-6} and lower) leads to high computation time, and sometimes the problem doesn't converge to meet such an accuracy criterion at all. After all trials, the following formula was chosen for the SSC:

$$\mathrm{SSC} = \min\left(10^{-4}, 10^{-5} \cdot \frac{\text{HRR Dry} - \text{HRR Wet}}{\text{target HRR accuracy}}\right)$$

   where HRR Dry and HRR Wet are the currently available boundaries of the Dryout HRR (DHRR).

2. The maximum void fraction (AMax) is a very useful criterion for the assessment of the states close to DHRR. It was shown that, for example, for a flat debris bed without bottom water injection the maximum void fraction for steady-state cooling is approximately equal to 0.8. Any higher values lead to gradual increase in the void fraction and, finally, to dryout. For non-flat configurations, or in the presence of water inflow from below, the maximum void fraction in the coolable state can reach 1.0, but it very quickly increases with the increase in HRR. Thus, the value of 0.95 was chosen as the critical value, indicating dryout in the bed.

Another important issue is to determine if the state became coolable after the HRR has been decreased. Simulations show that decrease of the AMax below 0.92 from the dryout state always indicate rewetting and show that current HRR corresponds to coolable state. But this criterion is not very efficient since the process of rewetting may take very long time, and it is hard to determine if the state is coolable or not since the fields are not converged to the steady state. To prevent this, after 500 s the current HRR is decreased, however, no conclusion is made about the state of the bed.

The full algorithm based on these two criteria is shown in Figure 1. The input data for the algorithm are the initial heat release rate, and the wet-state HRR (optional). In the initial state, DECOSIM runs until the steady state is reached, or dryout occurs. If the steady state is reached, the current value of HRR is considered as "wet" and the HRR is increased by a factor of 1.3. This multiplier was chosen since large HRR increase can lead to states far from the wet state, which converge very slowly, while small multipliers lead to slow convergence if the initial HRR is far below the dryout boundary.

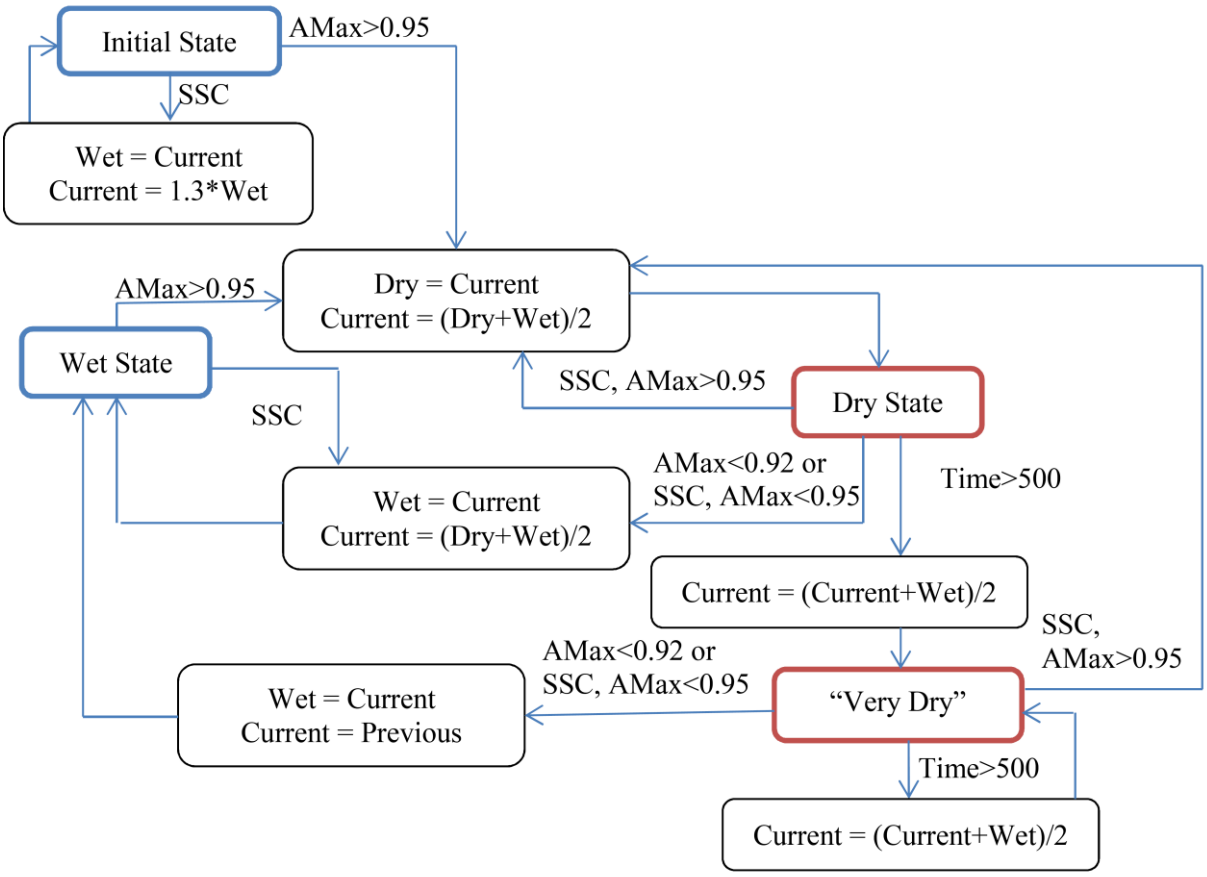

Figure 1: Bisection search algorithm for the dryout boundary.

After the first dryout has occurred, the main part of bisection algorithm is executed, in which there are two known states corresponding to coolable and non-coolable bed, and their arithmetic mean is used as the next current HRR to be checked. After each change of wet and dry limits, their difference is compared with the user-defined target HRR accuracy. Once the difference becomes smaller than the prescribed HRR accuracy, the average of the wet and dry-state HRR is taken as the coolability boundary.

Before the algorithm was applied to real problems, its sensitivity to computational parameters was studies in test calculations. There are three main parameters of the algorithm which may affect the final result: the steady state criterion, dryout and ramping void fractions, and initial values of heat release rate.

All data given below are obtained for the conical COOLOCE configuration with system pressure of 1.1 bar using Reed's model [48]. The grid had 31×57 cells, and the cell size was 1.0×1.0 cm. It should be noted that the method was also tested on many other configurations, including real pool simulations with different particle diameters, porosities, system pressure, and shape of the bed.

Before the algorithm was applied to validation simulations, its sensitivity to computational parameters was studies in the test calculations. There are three main parameters of the algorithm which may affect the final result: the steady state criterion, dryout and ramping void fractions, and initial values of heat release rate.

All data given below are obtained for the conical COOLOCE configuration with system pressure of 1.1 bar using Reed's model. The grid had 31×57 cells, and the cell size was 1.0 cm×1.0 cm. It should be noted that the method was also tested on many other configurations, including real pool simulations with different particle diameters, porosities, system pressure, and shape of the bed.

Dependence on Steady State Criterion (SSC)

The dependence on SSC is non-monotonic and is significantly affected by all input parameters and starting HRR values. There were found many parameters and starting points for calculations which misinterpreted the state as steady using the criterion $10^{-2} - 10^{-3}$. It was

shown that, in order to obtain the boundary with precision ~1%, it is enough to take steady state criterion equal to 10^{-4}.

Dependence on dryout and ramping void fractions

The results of changing the void fractions are shown in the figure. As was noted above, the maximum void fraction in the bed at steady state increases quickly with increase of the HRR. One can see from the table that the difference in results is higher than target HRR accuracy, however, it is still quite small.

Dryout void fraction	Ramping void fraction	DHRR, W/kg
0.93	0.965	199.5
0.95	0.975	200.8
0.97	0.985	201.8

Dependence on initial HRR

The algorithm is almost insensitive to the initial heat release rates. The results are shown in the table; one can see that their difference is less than target HRR accuracy.

Initial HRR, W/kg	Initial wet HRR, W/kg	DHRR, W/kg
250	130	200.8
223	115	200.6
220	190	200.8
240	170	200.9

Grid convergence

The grid convergence was also checked on the conical COOLOCE configuration with system pressure of 1.1 bar using Reed model. The grid was uniform in first 5 cases (see the Table below), the values of DHRR are shown in Figure 2.

Cell size, cm	Grid size	Grid Type	DHRR, W/kg
2.0	16×29	uniform	216.1
1.0	31×57	uniform	200.8
0.70	45×85	uniform	189.8
0.40	77×143	uniform	184.7
0.20	154×286	uniform	183.4
2.0-0.70	31×40	non-uniform, 1/3 dense	192.9

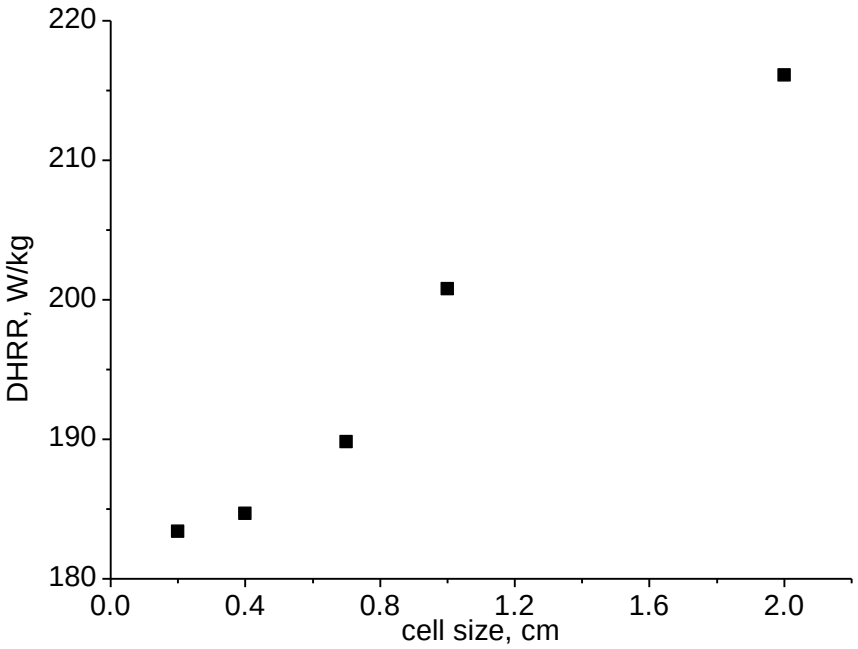

Figure 2: Grid convergence results: dependence of dryout heat release rate on cell size.

One can see that the difference in DHRR values obtained on grids with cell sizes 0.70 cm and 0.20 cm (the finest grid) is within 4%. However, simulations on the finest grid and require too much computational time because of large number of cells. To reduce the computational cost, a non-uniform grid was used with the refined area near the tip of the cone, since this region determines the coolability of the debris bed. The dryout heat release rate obtained on this grid is almost the same as on third grid, at the same time, the number of cells is three times smaller.

3.4 DECOSIM Simulations of COOLOCE Experiments

3.4.1 Parameters of DECOSIM Simulations

In the current validation studies, the data from the COOLOCE experiments performed at VTT in 2010-2013 (see [61], [62], [54], [55], [56], [57], [58]) were used. Simulations were carried with Reed's model [48] for the phase drag in the porous medium. Parameters of the calculations are listed in Table 1.

Table 1: Parameters used in DECOSIM simulations of COOLOCE experiments.

Fixed Parameters		
Water pool geometry	Radius:	0.306 m
	Height:	0.57 m
Cylindrical Geometry (COOLOCE-3,4,5) (impermeable side wall)	Height:	0.27 m
	Diameter:	0.31 m
	Surface area:	0.07548 m^2
	Volume:	0.02038 m^3
Conical Geometry (COOLOCE-6,7)	Height:	0.27 m
	Diameter:	0.50 m
	Volume:	0.01767 m^3
Cylindrical Geometry (COOLOCE-10) (open side wall)	Height:	0.27 m
	Diameter:	0.305 m
	Surface area:	0.0730 m^2
	Volume:	0.0197 m^3
Cone on Cylindrical Base Geometry (COOLOCE-12)	Height of conical part:	0.135 m
	Height of cylindrical part:	0.135 m
	Diameter of cylindrical part:	0.250 m
	Volume:	0.00884 m^3
Friction model	Reed	
Variable Parameters		
System pressure	P_{sys}:	1.1-6.95 bar
Particle diameters	d	0.8–1.07 mm
Porosity	ε	37–40%

The system pressure was varied in accordance with the conditions of each COOLOCE experiment. The debris bed porosity and mean particle diameter, however, were varied in order to take into account the existing uncertainties in the properties of the debris bed. The debris bed particles used in the COOLOCE tests were spherical beads of Zirconium silicate whose sizes vary between 0.8 mm to 1 mm. The porosity of the debris bed reported by VTT was 37%. However, measurements performed in POMECO-FL facility for the same particles gave a higher value of porosity close to 40%, while the mean particle diameter determined from the particle size distribution analysis was higher than 0.8 mm.

In the current simulations, the baseline debris bed properties were taken to be the lowest values of particle diameter $d = 0.8$ mm and porosity $\varepsilon = 37\%$. It was obtained that this case gives underestimates the dryout boundary in comparison with the COOLOCE experiments. Therefore, simulations were repeated with the porosity determined from POMECO-FL tests (40%) and the particle diameter 0.89 mm, as well as for the porosity reported by VTT (37%) and particle diameter 1.07 mm. In the latter cases, the effective particle diameter was found from the best agreement of DHF predictions from one-dimensional debris bed model with COOLOCE experiments performed for cylindrical debris bed.

Simulations of COOLOCE-10 and COOLOCE-12 experiments were carried out for the particle diameter 0.9 mm and porosity 40%.

3.5 Summary of Results

The simulation cases and the results obtained for cylindrical debris bed are summarized in Table 2 (for cylindrical debris bed with impermeable side walls) and Table 3 (for conical debris bed). For the conical debris bed, simulations have only been performed so far for two combinations of particle diameter and porosity, and only one point was obtained for the third combination.

The respective dependencies of the calculated dryout heat power on the system pressure are plotted in Figure 3 (for cylindrical debris bed, presented as the dryout heat flux DHF, W/m^2) and Figure 4 (for conical debris bed). On the same graphs, results of numerical simulations by MEWA code reported in [59] are plotted for comparison, with the respective particle

diameters and porosities indicated in the legends. Note that in [59] MEWA simulations of the cylindrical debris bed were carried out with Reed's model for the drag in porous medium [48], the same as used in the current DECOSIM simulations. However, for the conical debris beds, the model by Tung and Dhir [67] with the modifications for small particles proposed in [51] was used; this model takes into account the interphase drag which is neglected in Reed's drag model [48].

Table 2: DECOSIM simulations of COOLOCE experiments: cylindrical debris bed with impermeable walls.

Case No.	**Experiment**	**Pressure P_{sys}, bar**	**Experimental dryout power, kW**	**Calculated dryout power, kW**	**Comments**
1	COOLOCE-3	1.1	19.0	11.5	$d = 0.8$ mm, $\varepsilon = 37\%$
	COOLOCE-3R		20.4	19.0	$d = 0.89$ mm, $\varepsilon = 40\%$
				19.2	$d = 1.07$ mm, $\varepsilon = 37\%$
2	COOLOCE-4	1.6	23.4	14.7	$d = 0.8$ mm, $\varepsilon = 37\%$
				22.8	$d = 0.89$ mm, $\varepsilon = 40\%$
				23.0	$d = 1.07$ mm, $\varepsilon = 37\%$
3	COOLOCE-4	1.9	26.1	16.0	$d = 0.8$ mm, $\varepsilon = 37\%$
	COOLOCE-4bR	1.95	26.2	24.8	$d = 0.89$ mm, $\varepsilon = 40\%$
				24.9	$d = 1.07$ mm, $\varepsilon = 37\%$
4	COOLOCE-5	3.0	31.9	20.1	$d = 0.8$ mm, $\varepsilon = 37\%$
				30.6	$d = 0.89$ mm, $\varepsilon = 40\%$
				30.6	$d = 1.07$ mm, $\varepsilon = 37\%$
5	COOLOCE-5	4.0	34.6	23.1	$d = 0.8$ mm, $\varepsilon = 37\%$
				34.8	$d = 0.89$ mm, $\varepsilon = 40\%$
				34.7	$d = 1.07$ mm, $\varepsilon = 37\%$
6	COOLOCE-5	4.95	37.2	25.5	$d = 0.8$ mm, $\varepsilon = 37\%$
				38.1	$d = 0.89$ mm, $\varepsilon = 40\%$
				37.9	$d = 1.07$ mm, $\varepsilon = 37\%$
7	COOLOCE-5	6.95	42.3	29.6	$d = 0.8$ mm, $\varepsilon = 37\%$
				43.8	$d = 0.89$ mm, $\varepsilon = 40\%$
				43.4	$d = 1.07$ mm, $\varepsilon = 37\%$

Experimental data from COOLOCE tests are presented in Figure 3 and Figure 4 by the black points. Also, in Figure 3, an experimental point is plotted (green dot) corresponding to the measurement of dryout heat flux in POMECO-HT experiment [64] performed for the same spherical beads as in COOLOCE experiments.

Table 3: DECOSIM simulations of COOLOCE experiments with conical debris bed.

Case No.	**Experiment**	**Pressure P_{sys}, bar**	**Experimental dryout power, kW**	**Calculated dryout power, kW**	**Comments**
8	COOLOCE-6	1.1	26.0	18.0 27.8 28.1	$d = 0.8$ mm, $\varepsilon = 37\%$ $d = 0.89$ mm, $\varepsilon = 40\%$ $d = 1.07$ mm, $\varepsilon = 37\%$
9	COOLOCE-7	1.6	31.8	22.6 34.0 –	$d = 0.8$ mm, $\varepsilon = 37\%$ $d = 0.89$ mm, $\varepsilon = 40\%$ $d = 1.07$ mm, $\varepsilon = 37\%$
10	COOLOCE-7	2.0	36.0	25.5 38.2 –	$d = 0.8$ mm, $\varepsilon = 37\%$ $d = 0.89$ mm, $\varepsilon = 40\%$ $d = 1.07$ mm, $\varepsilon = 37\%$
11	COOLOCE-7	3.0	42.9	31.5 46.7 –	$d = 0.8$ mm, $\varepsilon = 37\%$ $d = 0.89$ mm, $\varepsilon = 40\%$ $d = 1.07$ mm, $\varepsilon = 37\%$

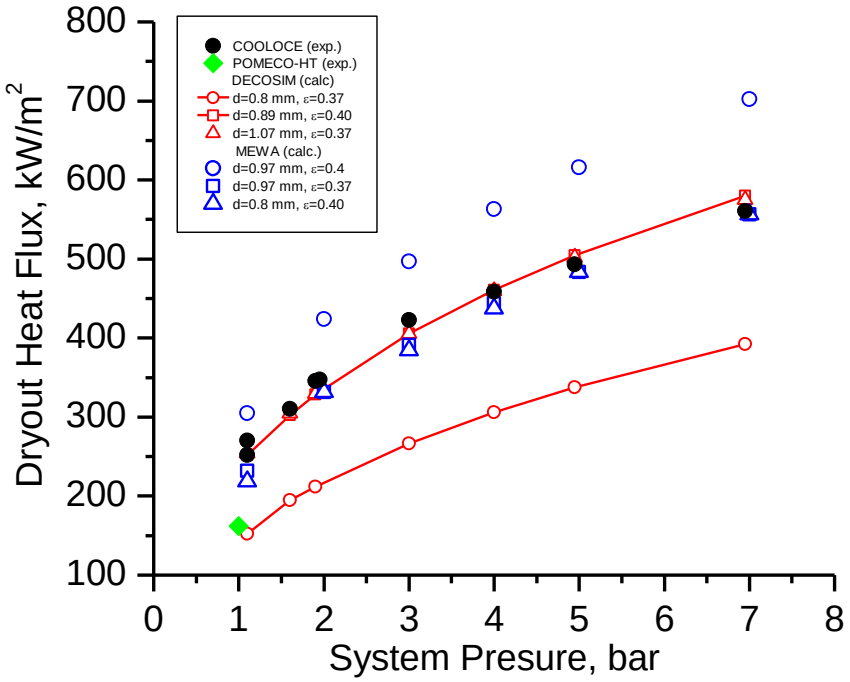

Figure 3: Comparison of calculated dryout heat power as function of system pressure (cylindrical debris bed) with COOLOCE experiments.

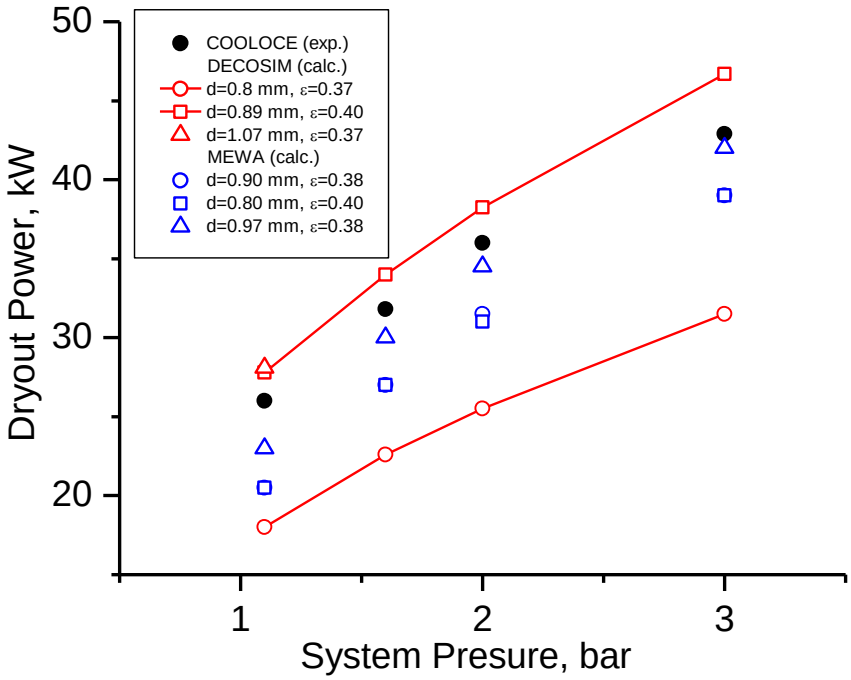

Figure 4: Comparison of calculated dryout heat power as function of system pressure (conical debris bed) with COOLOCE experiments.

In Table 4, results of DECOSIM simulations for cylindrical debris bed with open side walls are presented together with the corresponding data of COOLOCE-10 experiments. In order to evaluate the effect of side flooding on the dryout power, simulations were also performed on exactly the same numerical mesh, but with impermeable side walls (similar to the conditions of experiments and calculations presented in Table 2). The reason for performing this second set of simulations was that the pressures in COOLOCE-10 experiments were different from those in the experiments from Table 2, so that some form of interpolation would be required to obtain the ratio of dryout powers for open and impermeable side walls. Thus, in Table 4 for each experiment two values of dryout power are given, as well as their ratio $r = W_{open} / W_{imperm.}$.

One can see that simulations gave overestimated values for the dryout power in comparison with the experiments, especially taking into account that experimental values are the control powers which include not only the power necessary to boil water, but also the losses which are estimated to be about 10-20% of the control power.

No doubt, better agreement can be achieved by taking lower porosity and particle diameters (e.g., porosities of 37% and particle diameters of 0.87 mm are quoted in [57], [58], and the dryout boundary is known to be very sensitive to these parameters for sub-mm particles). However, of much higher interest is the accuracy of prediction of the ratio of powers with open and impermeable walls $r = W_{open} / W_{imperm.}$

The corresponding values are presented in Table 4 for DECOSIM simulations; also, similar values are evaluated from the results of COOLOCE-10 experiment (with open walls) and those presented in Table 2 (with impermeable walls). One can see that simulations give the value of approximately r=1.45, while in the experiments the average ratio is close (albeit, somewhat higher), r=1.5. This ratio is very important in the context of development of a surrogate model for debris bed coolability because it essentially depends on the debris bed geometry, namely, for a cylindrical bed, on the diameter-to-height ratio.

Table 4: DECOSIM simulations of COOLOCE-10 experiments, cylindrical debris bed with open side wall.

Case No.	**Experiment**	**Pressure P_{sys}, bar**	**Experimental dryout power, kW**	**Calculated dryout power, kW**	**Comments**
1	COOLOCE-10a	1.3	34.1 r=1.55	39.0 (open) 26.8 (imperm.) r=1.46	d = 0.9 mm, ε = 40%
2	COOLOCE-10b	2.0	40.1 r=1.53	50.6 (open) 35.6 (imperm.) r=1.42	d = 0.9 mm, ε = 40%
3	COOLOCE-10c	3.0	46.2 r=1.45	55.5 (open) 39.6 (imperm.) r=1.40	d = 0.9 mm, ε = 40%

Table 5, results of DECOSIM simulations for a cone-on-base shaped debris bed are presented, with corresponding data from COOLOCE-12 experiments [58]. One can see that the results are in very good agreement, although, reservations on the experimental power and high sensitivity of the results to porosity and particle diameter (see discussion of results presented in Table 4) must be kept in mind.

Table 5: DECOSIM simulations of COOLOCE-12 experiments, conical debris bed with on cylindrical base.

Case No.	**Experiment**	**Pressure P_{sys}, bar**	**Experimental dryout power, kW**	**Calculated dryout power, kW**	**Comments**
1	COOLOCE-12a	1.085	17.05	14.1	d = 0.9 mm, ε = 40%
2	COOLOCE-12b	1.98	19.65	19.1	d = 0.9 mm, ε = 40%
3	COOLOCE-12c	2.95	22.95	23.1	d = 0.9 mm, ε = 40%
4	COOLOCE-12d	3.81	25.59	26.0	d = 0.9 mm, ε = 40%

3.6 Discussion of Results

The following conclusions can be derived from the experimental and simulation results presented in Figure 3 and Figure 4.

There is a clear discrepancy between the experimental dryout heat fluxes obtained in COOLOCE and POMECO-HT facilities at the atmospheric pressure. The dryout heat flux of 270 kW/m^2 was measured in COOLOCE facility at the system pressure 1.1 bar (see [54], [59]), while in POMECO-HT facility a significantly lower value of DHF 161.8 kW/m^2 was obtained [64] for the same material, though at a slightly lower system pressure 1.0 bar (see experimental point in Figure 3). The difference is of the order of 100 kW/m^2, or about 40% of the higher DHF value. The following possible reasons for this discrepancy can be named:

1. Difference in the system pressures (1.1 vs 1.0 bar). Judging from the experimental behavior of DHF as a function of system pressure, as well as simulations presented in Figure 3, this can be ruled out as the factor responsible for the difference in DHFs (e.g., two-fold increase in DHF can be reached only by increasing the system pressure from 1 to 5 bars).
2. Differences in debris bed properties. Experiments in both facilities were carried out with similar (although, technically, not the same) particles, Zirconium-silicate beads. The particles were purchased from the same manufacturer [2]. The size distributions analyzed by VTT and KTH teams turned out to be somewhat different, with the average particles size estimated by VTT and KTH are 0.97 and 0.95 mm respectively, with the standard deviation 0.07 mm. The porosity estimated (although not measured directly) by VTT was 0.37 [61], whereas in the POMECO-HT facility the porosity obtained from the measured filled volume, density of material and the weight of the bed was found to be 0.371 [64]. The figures quoted imply that the properties of debris beds in both facilities were close enough and, per se, cannot be the main reason for the difference in measured DHFs.
3. Differences in geometry and heater arrangement. In COOLOCE facility, the debris bed was cylindrical (0.31 m in diameter, top surface area 0.07548 m^2, height 0.27 m, total volume 20 litres) and immersed in a water pool. In POMECO-HT facility, the debris bed was square in plan (0.2 m side, top surface area 0.04 m^2, height 0.25 m, total volume 10 litres), its side walls were thermally insulated. Therefore, the geometries seem to be comparable. However, the heaters in COOLOCE facility are

6.3 mm thicker and are oriented vertically, with the top 40 mm of the bed being unheated. In POMECO-HT, on the contrary, the heaters are 3mm thick and horizontal. It is estimated that the heaters occupy 2.5% of debris bed volume in COOLOCE, and 0.7% in POMECO-HT. It can be argued that vertical heaters can effectively create local "channels" in the debris bed providing pathways for vapor evacuation from the bed, which can explain higher dryout heat fluxes observed in COOLOCE facility. Also, effects of anisotropy of debris bed properties due to the presence of heaters are not clear at the moment.

The simulations carried out by DECOSIM code with the porosity 37% and effective particle diameter 0.8 mm determined from POMECO-FL experiments gave the dryout heat flux at the atmospheric pressure close to that measured in POMECO-HT facility (see the bottom curve in Figure 3). This might imply that the experimental conditions in POMECO-HT were close to those assumed in simulations (homogeneous debris bed with uniform heating of the material over the volume).

The dependence of DHF on system pressure from COOLOCE experiments can be reproduced quite accurately if either the effective particle diameter or debris bed porosity is increased. For a cylindrical debris bed, good agreement is achieved in DECOSIM simulations for the particle diameter 0.89 mm and porosity 0.4, see Figure 3. The results obtained are consistent with MEWA simulation results reported in [59] where larger particle diameters and porosities were found to be necessary to reproduce the experimental data on DHF.

For the conical debris bed, DECOSIM simulations with the baseline parameters (particle diameters of 0.8 mm and porosity 37%) underestimate the dryout heat flux, see Figure 4. On the other hand, simulations with the particle diameter 0.89 mm and porosity 0.4 overestimate the dryout heat flux by about 8%.

It is interesting to note that, despite the difficulty in predicting the absolute values of dryout heat flux due to high sensitivity of results to the values of debris bed porosity and particle diameter, the relative improvement of debris bed coolability for conical debris bed in comparison with flat (or cylindrical, behaving effectively as a flat) debris bed is captured quite well in the simulations. As an example, consider the results of recent DECOSIM simulations [73] performed for prototypic reactor conditions, rather than for small-scale

COOLOCE experiments. As the reference case, the following parameters were taken: $d = 1.5$ mm, $\varepsilon = 0.4$ pressure above the water level 1 bar, hydrostatic head of water at the cone tip 0.602 bar, mass of melt released is $M = 256$ t. Calculations were carried out in a cylindrical pool of the diameter $D_p = 12$ m, the density of corium was taken $\rho = 8285.1$ kg/m^3. The slope angle of the bed θ was varied from zero to 45°, and depending on the slope angle, the debris bed was either conical (for large enough θ), or was comprised of a cone on a cylindrical base.

In Figure 5, the ratio of the dryout heat fluxes DHF for a conical debris bed, and the dryout heat flux for a flat debris bed with the same properties, DHF_0, is plotted. This ratio characterizes the relative improvement of coolability of non-flat debris bed due to side ingress of water into the bed. On the same graph, points are shown for the slope angle $\theta = 47°$ of four COOLOCE experiments corresponding to system pressures of 1.1, 1.6, 1.9, and 3.0 bar. In the latter case, the experimental value of dryout heat flux for the cylindrical bed was taken as DHF_0. One can see that the agreement is quite reasonable, which can be regarded as partial validation of DECOSIM code and, as well, as an indication that the relative increase in DHF due to shape effects are captured correctly.

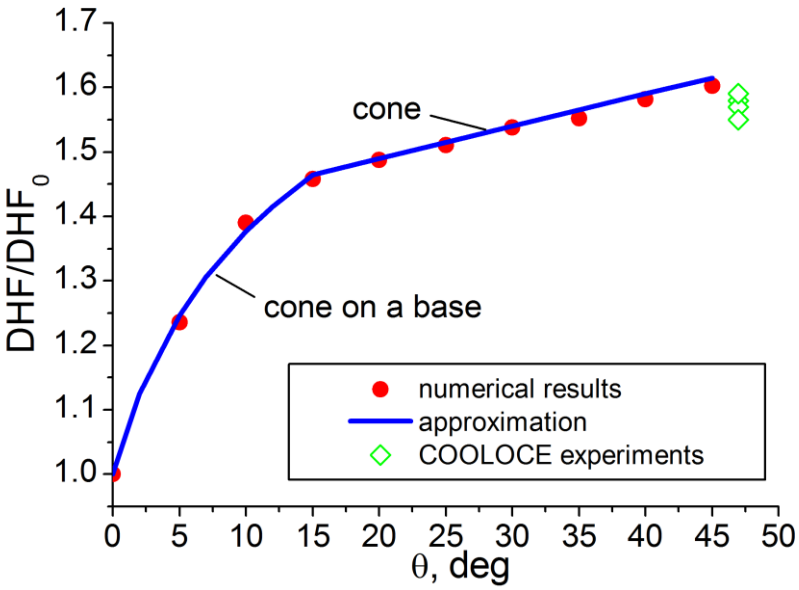

Figure 5: Dependence of ratio DHF/DHF_0 on the slope angle.

3.6.1 Simulations of Debris Bed with Closed Top

COOLOCE-11 experiment [60] is different from the other experiments performed in VTT in that the debris bed top was impermeable in order to simulate effect of agglomeration. It was shown in MEWA simulations carried out in [60] that calculations give lower dryout power than that for top flooding, while the dryout power obtained in COOLOCE-11 experiments was higher (better coolability). Since DECOSIM is based on the similar models as those in MEWA, it was decided not to repeat simulations, but to study sensitivity of dryout power to conditions in the top part of the bed and look for the reasons which could have led to the discrepancy in the dryout powers in the experiment and simulations.

The heat-releasing volume was of height 0.23 m, the top 0.04 m were filled with a passive (not heat-releasing) porous material. Simulations were carried out for the system pressure of 2 bar, the heating power of 30 kW corresponded to the experimental power. It was suggested that the above differences between the experiments and simulations [60] were caused by an imperfect contact between the porous medium and the top lid. The configurations shown in Figure 6 were considered, with the following conditions in the top layer of the debris bed:

- The top layer had the nominal porosity 0.4 and particle diameter 0.97mm (same as in the heated part of the bed);
- Porosity of the top layer was increased to 0.5, particle diameter was 0.97 and 1.2 mm;
- Top layer had a reduced by half height of 0.02 m, above it there was free space up to the top plate.

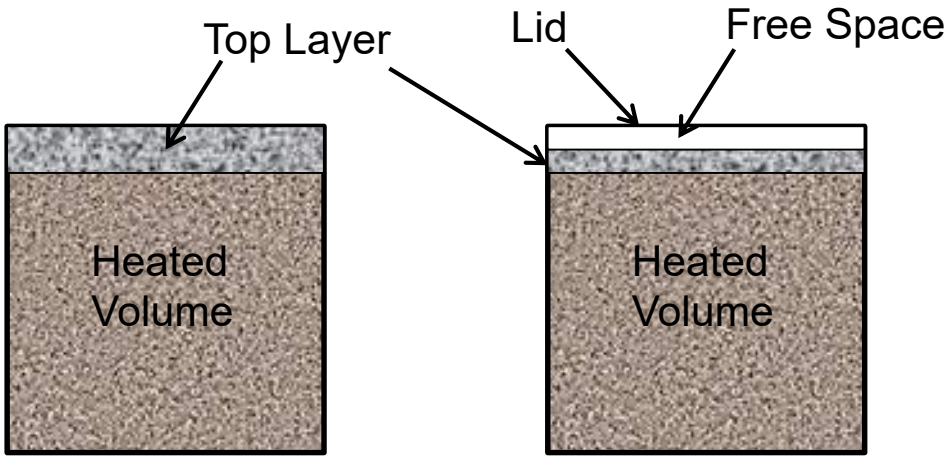

Figure 6: Configurations used in DECOSIM simulations of the closed-top debris bed.

The results obtained in the simulations are summarized in Table 6.

Table 6: Summary of DECOSIM results for closed-top debris bed.

Top Layer Parameters	**Results**
Nominal porosity and particle diameter (d=0.97mm, ε=0.4)	Dryout under the lid, steady temperature escalation
Increased porosity, nominal particle diameter (d=0.97mm, ε=0.5)	Dryout under the lid, temperature stabilized at 20K superheat w.r.t. saturation temperature
Increased porosity and particle diameter (d=1.2 mm, ε=0.5)	Dryout under the lid, no superheat in the dry zone
Reduced porous layer height, free space above it up to the lid	Dryout under the lid, no superheat in the dry zone

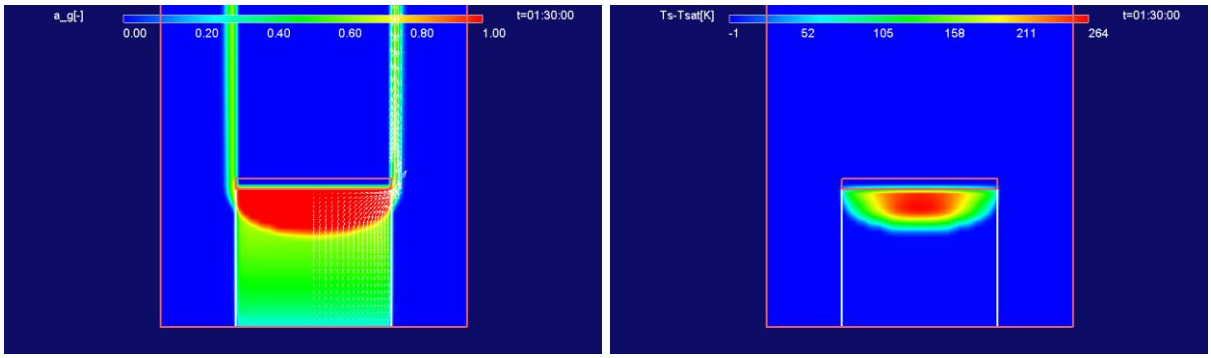

Figure 7: Void fraction (left) and particle temperature (right) in debris bed with nominal parameters of the top layer (d=0.97mm, ε=0.4).

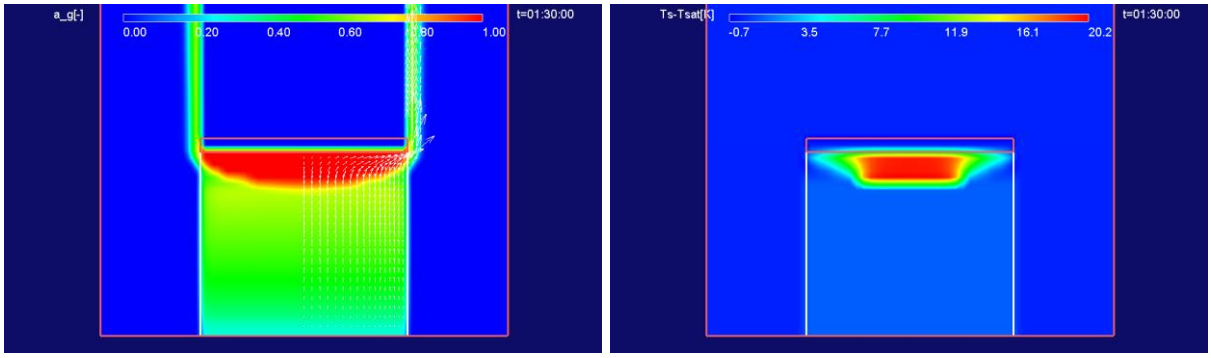

Figure 8: Void fraction (left) and particle temperature (right) in debris bed with increased porosity and nominal particle diameter (d=0.97mm, ε=0.5).

The spatial distributions of void fraction and particle temperature in the debris bed in the four cases listed in Table 6 are presented in Figure 7 – Figure 10. All distributions correspond to

time 1h 30 min. Note that distributions in Figure 7 are unsteady (temperature is increasing with time), while in Figure 8 – Figure 10 the distributions are steady-state.

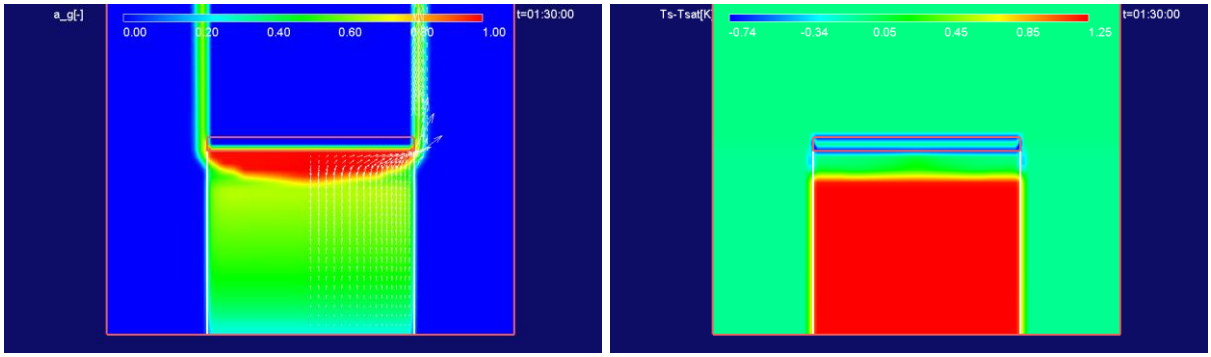

Figure 9: Void fraction (left) and particle temperature (right) in debris bed with increased porosity and particle diameter (d=1.2 mm, ε=0.5).

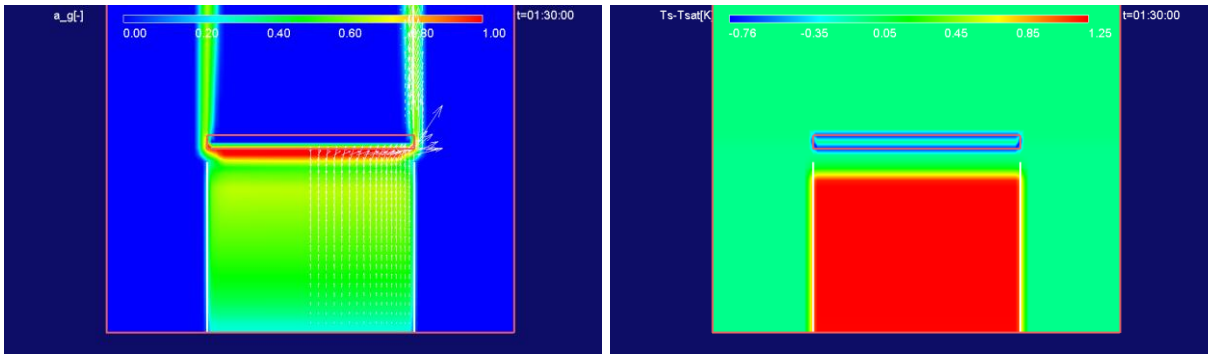

Figure 10: Void fraction (left) and particle temperature (right) in debris bed with d=0.97mm, ε=0.4.

The following conclusions can be drawn from simulations of COOLOCE experiments:

- Simulations show that dryout conditions are very sensitive to particle diameter and porosity of the bed.
- Generally, reasonable agreement between simulations and experiments was achieved
- For the side-only flooding, results are very sensitive to conditions in the top (unheated) layer.
- It is necessary to compare not only the absolute dryout powers (subject to uncertainties), but also ratio of dryout powers which depends on the shape and characterizes 2D effects.

3.7 Simulation of Post-dryout Debris Bed

Once some zone in a debris bed dries out, the temperature of solid material starts to grow due to the continuing decay heat release. However, there are heat transfer mechanisms which provide cooling to the solid particles even in the absence of water evaporation. Among them is heat transfer to the gas phase, heat conduction in the particulate debris, radiative heat transfer (which can become effective at high enough temperatures of the solid material). These heat transfer mechanisms can provide stabilization of solid material temperature at some level above the water saturation temperature. Therefore, an important question concerning the post-dryout behavior of debris bed is whether the temperature in the dry zone can reach some critical levels at which remelting of debris and thermal attack on the basemat of reactor containment can occur.

Post-dryout behavior of debris beds was studied on the basis of numerical simulations by DECOSIM code; also, an analytical model for post-dryout debris bed heat transfer was developed [74]. Two debris bed geometries were studied in simulations by DECOSIM code: a mound-shaped debris bed and a conical bed, resting on the basemat of a water pool of 9 m in diameter. The computational domain was 6 m high, on its top boundary a constant system pressure $P_{sys} = 3$ bar was maintained. The conical debris bed was of height $H = 3$ m, the diameter of its base was 6 m. The mound-shaped debris bed was of the height 2.5 m, the diameter of its base was 6 m, and that of the top was 2 m. For each geometry, several cases were calculated, with the main variable parameters being the mean particle diameter D_p ranging from 1 to 3 mm, and the specific decay heat power W ranging from 150 to 250 W/kg. The simulation matrix is summarized in Table 7, with the case acronyms comprised of geometry (C is for conical, M is for mound-shaped debris bed), particle diameter d* (in millimeters), and decay heat specific power W* (in W/kg).

Numerical grids used in the simulations had 30 cells in the radial direction (uniform grid, 15 cm cells) and 51 cells in the vertical direction (non-uniform, with the minimum cell size of 7 cm near the top boundary of the debris bed). The computational domain and numerical grids are shown in Figure 11, with the debris bed shape shown by the white line.

Table 7: DECOSIM simulations of post-dryout debris beds.

Case	**D_p, mm**	**W, W/kg**	**$T_{s,max}$, K**	**$T_{s,max}$-T_{sat}, K**	**Z_{bot}/Z_{top}, m**	**ξ, [–]**
Conical, H = 3 m						
C-d1-W150	1	150	*1334.0*[a]	*947.0*[a]	0.3/2.8	0.89
C-d2-W150	2		559.8	173.4	1.8/2.8	0.36
C-d1-W200	1	200	*1699.1*[a]	*1311.7*[a]	0.05/2.8	0.89
C-d2-W200	2		781.5	395.0	1.37/2.8	0.51
C-d3-W200	3		512.5	126.1	2.1/2.8	0.25
Mound-shaped, H = 2.5 m						
M-d1-W150	1	150	*1300.0*[a]	*912.5*[a]	0.23/2.4	0.90
M-d2-W150	2		476.7	89.9	1.95/2.45	0.20
M-d1-W200	1	200	*1646.5*[a]	*1258.9*[a]	0.05/2.4	0.98
M-d2-W200	2		654.9	268.5	1.4/2.45	0.43
M-d3-W200	3		419.0	32.4	2.30/2.45	0.06
M-d1-W250	1	250	*1978.7*[a]	*1590.3*[a]	0/2.4	1
M-d2-W250	2		994.5	608.1	1.0/2.45	0.59
M-d3-W250	3		546.6	160.2	1.70/2.45	0.31

[a] *Temperature stabilization did not occur, values at time 4000 s are given*

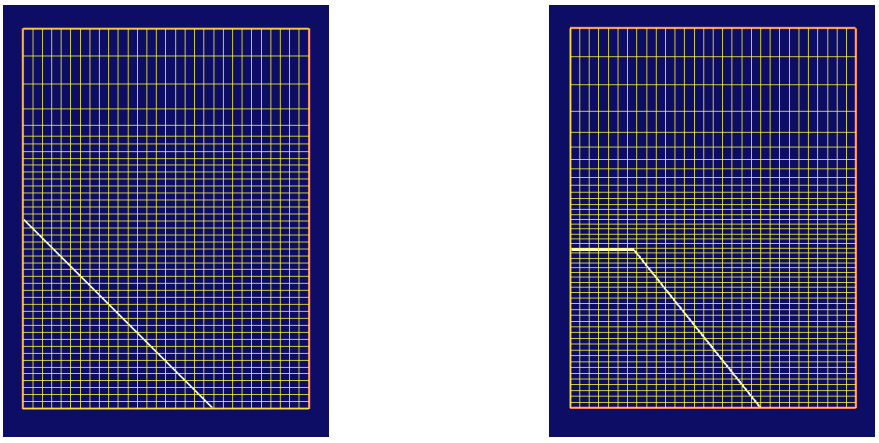

(a) (b)

Figure 11: Computational domain and numerical grid used for simulations of conical (a) and mound-shaped (b) debris bed.

Simulations started from the initial conditions of quenched debris bed, the initial temperatures of the solid material and water in the pool were set to the local saturation temperature, and the initial void fraction was set to zero. Calculations were carried out for the period of 5000 s which was sufficient for the establishment of steady-state temperature in the dryout zone in most of the cases where stabilization was observed.

In Figure 12, the time histories of the maximum temperature of the solid material are shown for the cases presented in Table 7, the cases where temperature stabilization occurred are shown in bold. It can be seen that the time of dryout occurrence (visible as the time at which the temperature curve deviates from the initial saturation temperature) is of the order of few minutes and is determined by the decay heat. In all the cases with particle diameters of 3 mm, temperature stabilization occurred, while for the smallest particles (1 mm) steady temperature rise is observed at a rate proportional to specific power W.

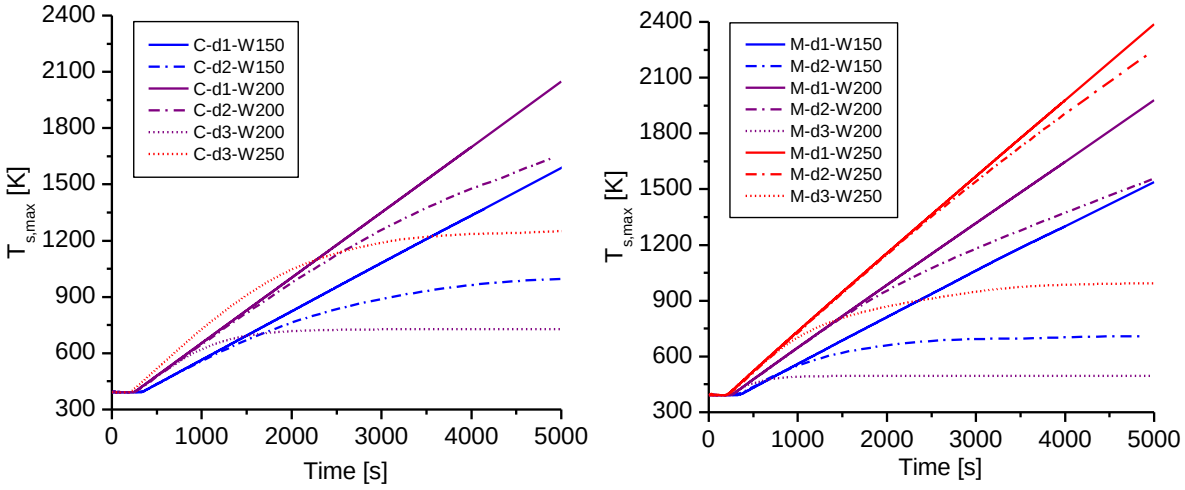

(a) (b)

Figure 12: Time histories of the maximum temperature of solid particles in conical (a) and mound-shaped (b) debris bed

Typical spatial distributions of the void fraction and temperature of the solid material in post-dryout conical and mound-shaped debris beds are shown in Figure 13 and Figure 14, respectively. In Figure 15, the vertical distributions of void fraction (left) and vapor temperature (right) on the axis of symmetry are shown for all the cases from Table 7 in which stabilization of the dry zone was obtained. One can see that the temperature distribution in the dry zone is nearly linear, the fact which will be used in the following section to derive an analytical model for the dry zone.

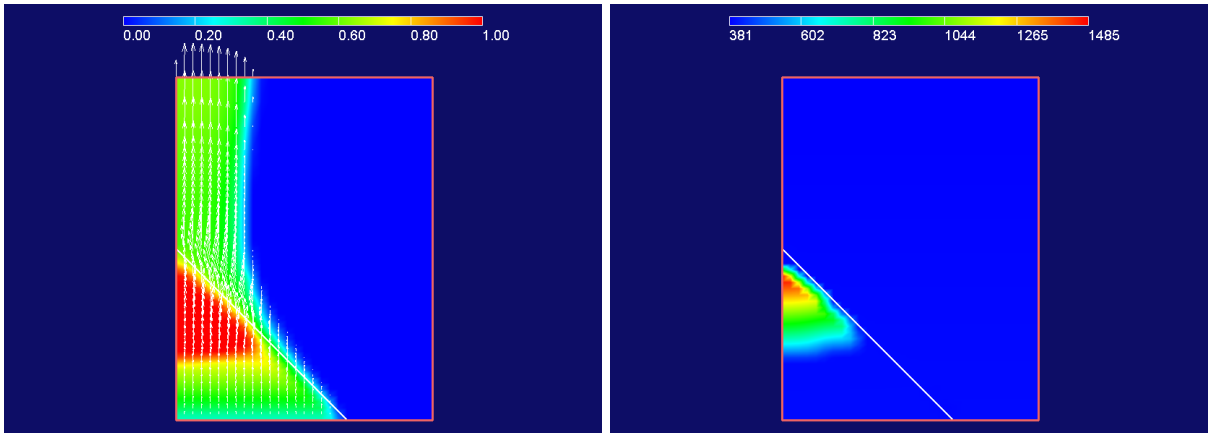

Figure 13: Void fraction (left) and solid particle temperature (right) in the post-dryout cone-shaped debris bed ($W = 200$ W/kg, $D_p = 2$ mm) at time 4000 s

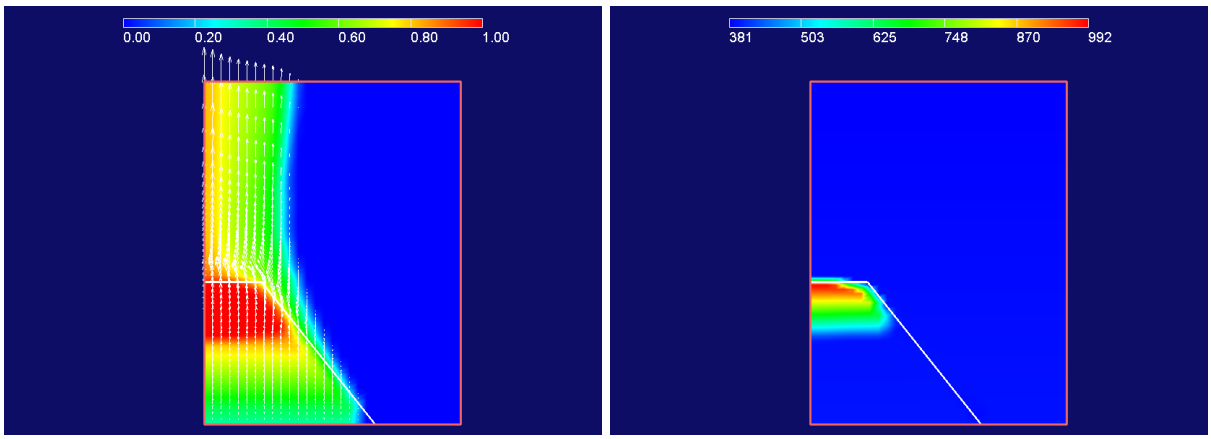

Figure 14: Void fraction (left) and solid particle temperature (right) in the post-dryout mound-shaped debris bed ($W = 250$ W/kg, $D_p = 3$ mm) at time 4000 s

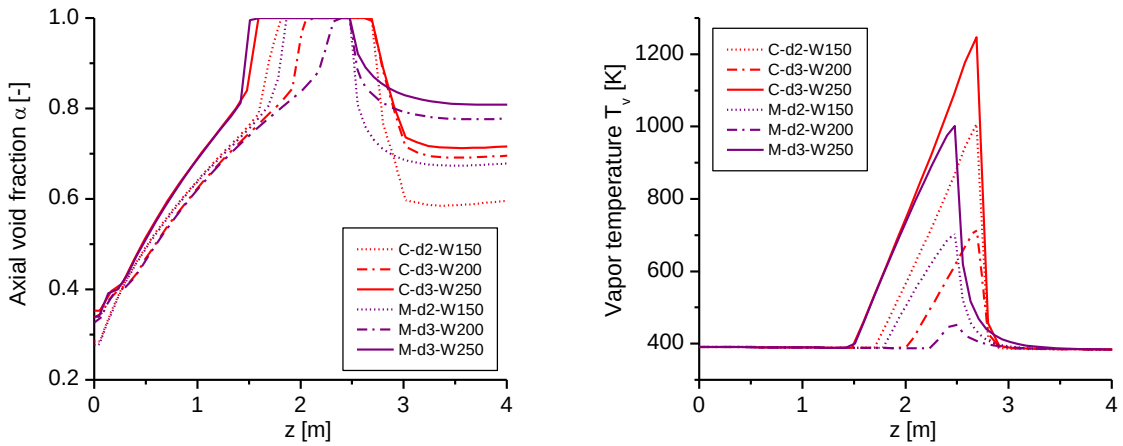

Figure 15: Void fraction (left) and vapor temperature (right) distributions along the axis of symmetry for the cases where temperature stabilization was obtained (see Table 7)

The vertical distributions of void fractions on the axis of symmetry presented in Figure 15, were used to determine the vertical coordinates of the top and bottom boundaries of the dry zone (Z_{top} and Z_{bot}, respectively), as well as the fraction of debris bed height occupied by the dry zone $\xi = \left(Z_{top} - Z_{bot} \right) / H$.

The numerical results obtained by DECOSIM indicate that in the cases where dryout occurs in the debris bed

- Dryout zone is located in the top part of the debris bed;
- Vapor flows through the dry zone vertically upwards;
- Temperatures of solid particles and vapor increase in the vertical direction almost linearly, the difference between them being few degrees;
- Maximum temperatures of solid particles and vapor are attained in the top part of the dry zone;
- Vapor cooling is capable of stabilization of solid material temperature, provided that its flowrate through the dry zone is sufficient.

These observations imply that the dry zone has relatively simple structure which can be described by an analytical model.

In the model, one-dimensional mass and energy conservation equations were formulated for the single-phase vapor flow in the dry zone, with the mass flux determined by the total evaporation rate in the wet zone underneath the dry one. Steady-state solution was considered, and the maximum temperature reached at the top boundary of the debris bed was found. The analytical model allows one to obtain a formula relating the critical fraction of debris bed taken by the dry zone ξ_* to the critical maximum temperature T_* (for example, the temperature at which oxidation starts, or melting temperature of the material):

$$T_* = T_{sat} + \frac{\Lambda}{C_P} \frac{\xi_*}{1-\xi_*} \quad \text{or} \quad \xi_* = \frac{C_P \left(T_* - T_{sat} \right)}{\Lambda + C_P \left(T_* - T_{sat} \right)}$$

The function $T_* \left(\xi_* \right)$ is plotted in Fig. 6 by the solid line, the saturation temperature taken equal $T_{sat} = 390\,\mathrm{K}$. The dashed lines correspond to two characteristic values of the critical temperature. It follows from Figure 16 that the material in the dry zone can be reheated to the

temperature of 1500 K at which zirconium oxidation begins if the dry zone takes at least half the height of the debris bed. Corium remelting temperature 2800 K can be reached if the dry zone takes at least 70% of the debris bed height. This last case corresponds to massive dryout of the debris bed. Temperature escalation in smaller dry zones will be stabilized due to large flowrate of vapor generated under the dry material which is sufficient to remove the decay heat from the porous material.

The points in Figure 16 correspond to the results of numerical simulations carried out by DECOSIM for conical and mound-shaped debris beds (see Table 7). Evidently, the analytical formula predicts quite well the maximum temperature rise in the debris bed. Importantly, the results in Figure 16 are practically independent of debris bed shape and involve only few parameters, which reduce the uncertainties in the estimation of post-dryout behavior of debris beds. In the further work, relationship between the relative size of the dry zone and debris bed properties has to be obtained in order to apply the theory presented in the current work in the context of surrogate model for debris bed coolability and analysis of severe accidents risks. Note that recently these results were confirmed independently by MEWA simulations performed at VTT.

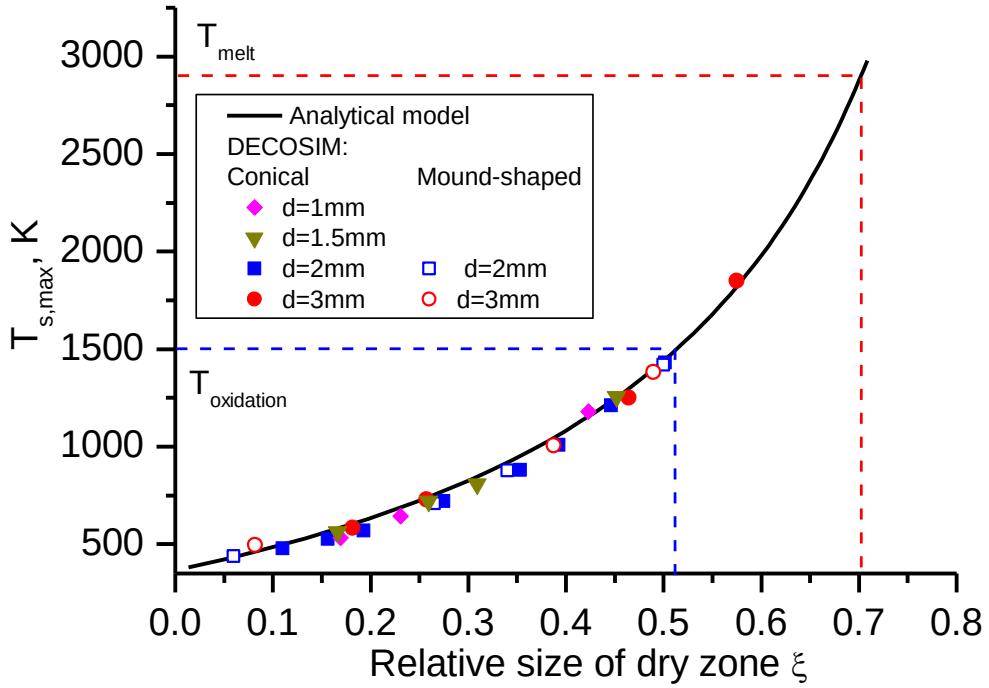

Figure 16: Dependence of the critical temperature on the relative size of dry zone

To verify the assumptions of the analytical model against the numerical predictions, vertical distributions of vapor temperature in the dry zone presented in Figure 15 (right) are replotted in Figure 17 in non-dimensional form $\theta(\zeta)$, with $\theta = C_p(T - T_{sat})(1-\xi)/\Lambda\xi$ being the non-dimensional excess temperature, $\zeta = (Z - Z_{bot})/(Z_{top} - Z_{bot})$ being the non-dimensional vertical coordinate spanning the interval [0,1] in the dry zone.

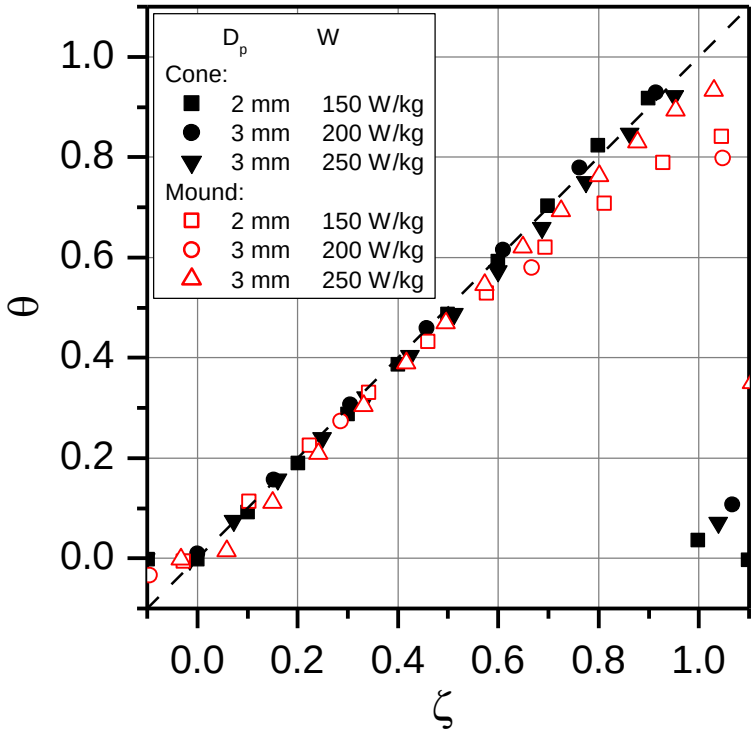

Figure 17: Vertical profiles of vapor temperature in the dry zone in non-dimensional coordinates

Evidently, the temperature rise in the dry zone agrees quite well with the analytical mode which predicts that in the dry zone $\theta = \zeta$ (diagonal line shown by the dashed line). Some deviations from the analytical model are visible near the top boundary of the debris bed, which can be attributed to quenching of the topmost cells by water ingress (while the analytical model predicts that dry zone extends up to the debris bed top). Also, grid effects might have contributed to some smearing of temperature distributions, especially for small-size dry zones covering only a few grid cells.

The relative size of dry zone ξ was plotted for each geometry against the decay heat power W, see Figure 18. Each set of data points exhibits linear behavior (see the straight lines), so that $\xi = a(W - W_0)$, where a is the proportionality coefficient, W_0 is the heating power at which the corresponding line intersects the ξ-axis. The latter can be interpreted as the dryout power, since it corresponds to the specific power W at which the dryout zone vanishes. Introduce the overheating parameter $\psi = (W - W_0)/W_0$, i.e., the ratio of the excess heating power and the dryout power. Then $\xi = aW_0(W - W_0)/W_0 = b\psi$, $b = aW_0$.

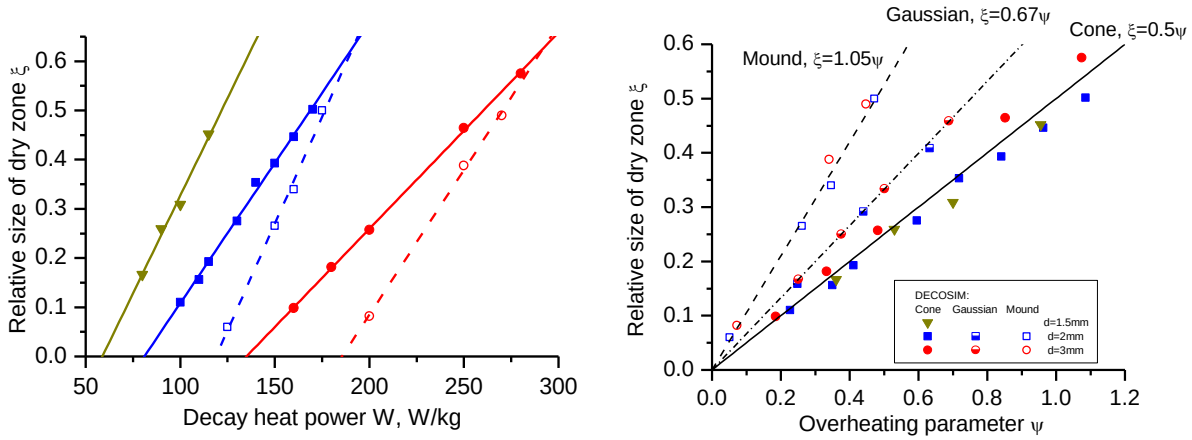

(*a*) (*b*)

Figure 18: Dependence of the relative size of dry zone on decay heat power W (*a*) and overheating parameter ψ (*b*). The legend applies to both Figures.

Parameters which describe the dependency of the dry zone size on the decay heat power obtained for different configurations are summarized in Table 3-8; in the rightmost column, the dryout heat flux calculated as $DHF = \rho_s(1-\varepsilon)W_0H$ is given. An important feature is that, although the proportionality coefficient a and dryout power W_0 exhibit significant variation between the configurations and apparent dependency on the particle size (that affect resistance to the flow), their non-dimensional product $b = aW_0$ is nearly constant for each debris bed shape and fairly insensitive to the particle size. To illustrate this, the data from Figure 18a is replotted in Figure 18b in terms of the overheating parameter ψ, see Eq. 30, with the best-fit linear approximations shown (the point scatter is within 3% for the mound-shaped debris bed, and within 8% for the cone-shaped bed, the latter is mostly due to the input of 3 mm particles).

The results obtained allow us to formulate a surrogate model for post-dryout behavior of ex-vessel debris beds to be used in ROAAM+ framework. Also, important estimates can be obtained from the models developed. To reach the oxidation temperature 1500 K, it is necessary to have the relative dry zone size of about $\xi \approx 0.5$ (see Figure 16). For the cone-shaped debris bed, this means the overheating about $\psi \approx 1$, or the actual heat flux HF must exceed DHF by a factor of 2 (see Figure 18b). Accordingly, for the mound-shaped bed, the overheating parameter must be about $\psi \approx 0.5$, or the heat flux HF must be 50% higher than DHF. Remelting occurs at the relative dry zone size about $\xi \approx 0.7$ (see Figure 16); for the cone-shaped bed this means that HF is 2.4 times higher than DHF; for the mound-shaped bed HF is 70% higher than DHF.

Table 8: DECOSIM simulations of post-dryout debris beds.

d, mm	a , kg/W	b , [-]	W_0, W/kg	DHF, MW/m^2
Cone-shaped, H=3 m				
1.5	0.00793	0.467	58.8	0.876
2	0.0057	0.462	81	1.208
3	0.00399	0.539	135	2.013
Mound-shaped, H=2.5 m				
2	0.00867	1.030	119.9	1.49
3	0.00589	1.093	185.6	2.31
Gaussian-shaped, H=2.5 m				
2	0.00625	0.651	104.2	1.30
3	0.00417	0.667	159.9	1.98

3.8 Implementation of Particle Spreading Model

In PDS-C experiments (see Section 4.2), a correlation for the particle flux as a function of local slope angle, gas flowrate, and debris bed properties was obtained in the non-dimensional form. These correlations were implemented in DECOSIM in order to enable simulations of debris beds with evolving (due to particle spreading) geometry.

A subroutine for dynamic redistribution of particles was implemented in DECOSIM. On each time step, particle fluxes are evaluated at the boundaries between the top surface of debris bed, and particulate matter is redistributed accordingly along the debris bed top, ensuring proper emptying/filling of top cells and packing to provide the given debris bed porosity

Implementation of particle spreading algorithm in DECOSIM was verified against the 1D numerical model which solves the equation for debris bed height which is, essentially, a debris mass conservation equation. In these verification studies, to provide compatible spreading conditions, two-phase flow simulations were switched off in DECOSIM, and the superficial vapor velocity at the debris bed top was obtained from the (constant) volumetric evaporation rate and current debris bed height: $U_g = \Gamma h / \rho_v$, where Γ is the volumetric evaporation rate, h is the local height, ρ_v is the vapor density. Good agreement between the maximum debris bed heights as functions of time calculated by DECOSIM and that from 1D model was demonstrated, as well as the shapes of debris bed at selected times were found to practically coincide. In Figure 19, the results of DECOSIM simulations of debris bed spreading are presented, demonstrating the change in debris bed shape with time.

Few preliminary fully coupled DECOSIM simulations of debris bed were performed in which the superficial gas velocity and gas parameters involved in the correlation for the lateral particle flux were obtained from the two-phase flow model. Simulations were carried out with and without particle spreading taken into account, with the following parameters:

- Conical debris bed, slope angle 30^o
- Total mass of corium 143 t.
- Relocation time 1.5 h (used for specific decay heat power calculation).
- Porosity 40%.
- Particle diameter of 1, 1.5, and 2.0 mm.

Maximum temperatures of solid material were compared in the cases with and without particle spreading, see Figure 20.

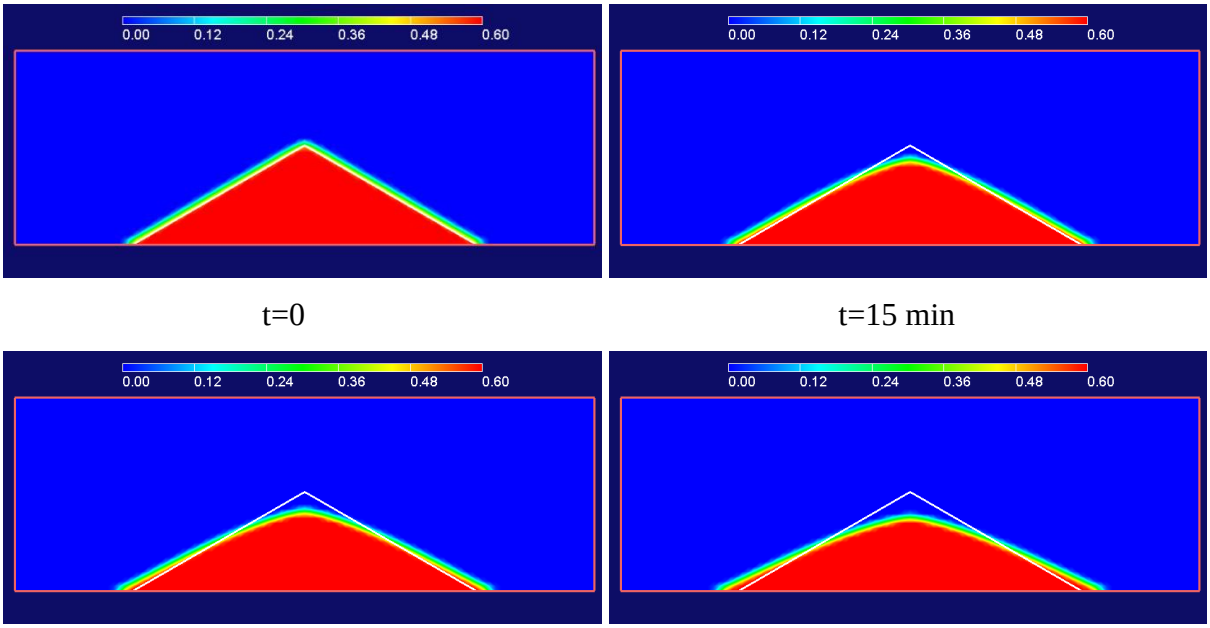

Figure 19: Self-levelling of debris bed (volume fraction of particles, d=1mm, W=160 W/kg)

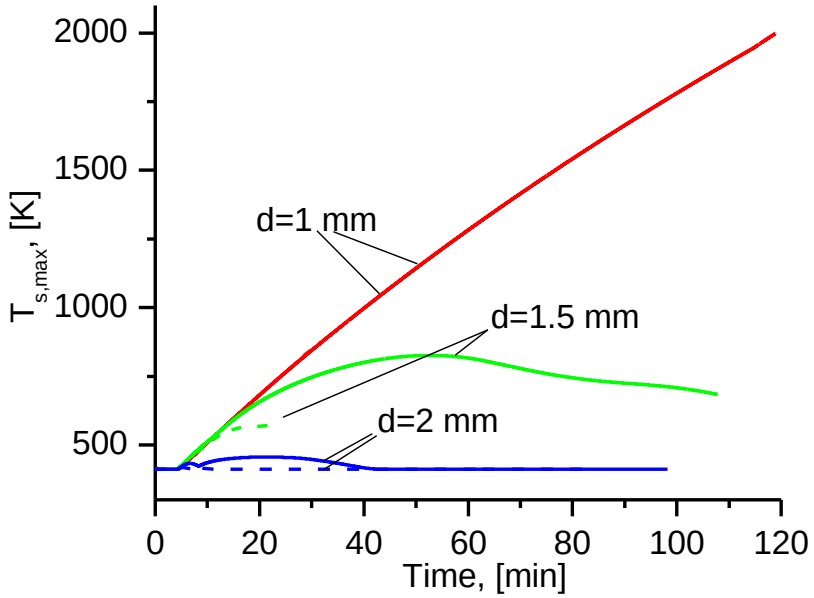

Figure 20: Maximum temperatures of solid particles. Solid lines: no spreading, dashed lines: spreading

The following conclusions can be drawn:

- For 1 mm particles, debris bed is non-coolable, temperature escalation is observed with or without particle spreading.
- For 1.5 mm particles temperature stabilization is observed, for spreading debris bed (dashed lines) the maximum temperature is stabilized at a lower level.
- For 2 mm particles, debris bed is coolable, regardless of particle spreading.

Further studies are necessary in order to quantify the effect of the dry zone on debris bed spreading and coolability. However, results on the effect of initial state (dry or wet) on the particle spreading were obtained in DECOSIM simulations. The time histories of debris bed height are plotted in Figure 21

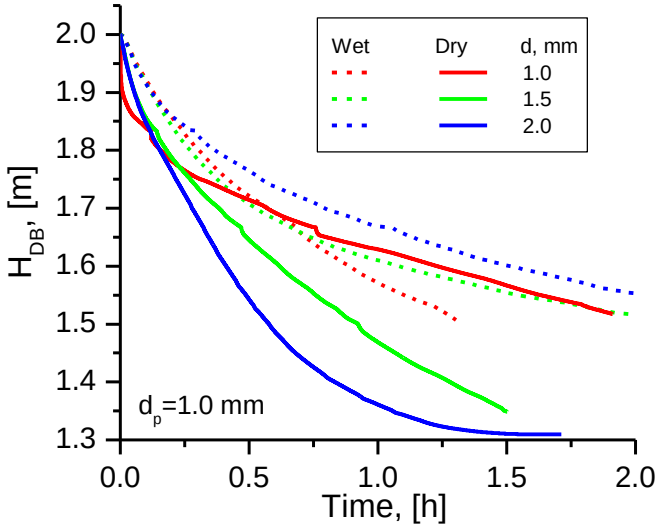

Figure 21: Height of initially dry and wet debris beds

Self-leveling reduces bed height by 20-35%. For initially dry debris beds large (2 mm) particles are spread faster than smaller ones (1 mm). This occurs because the superficial gas velocity is higher near the debris bed tip, as illustrated in Figure 22. Active water evaporation during reflooding increases gas flow through the hot dry zone, which results in faster leveling of debris bed tip for 2 mm particles.

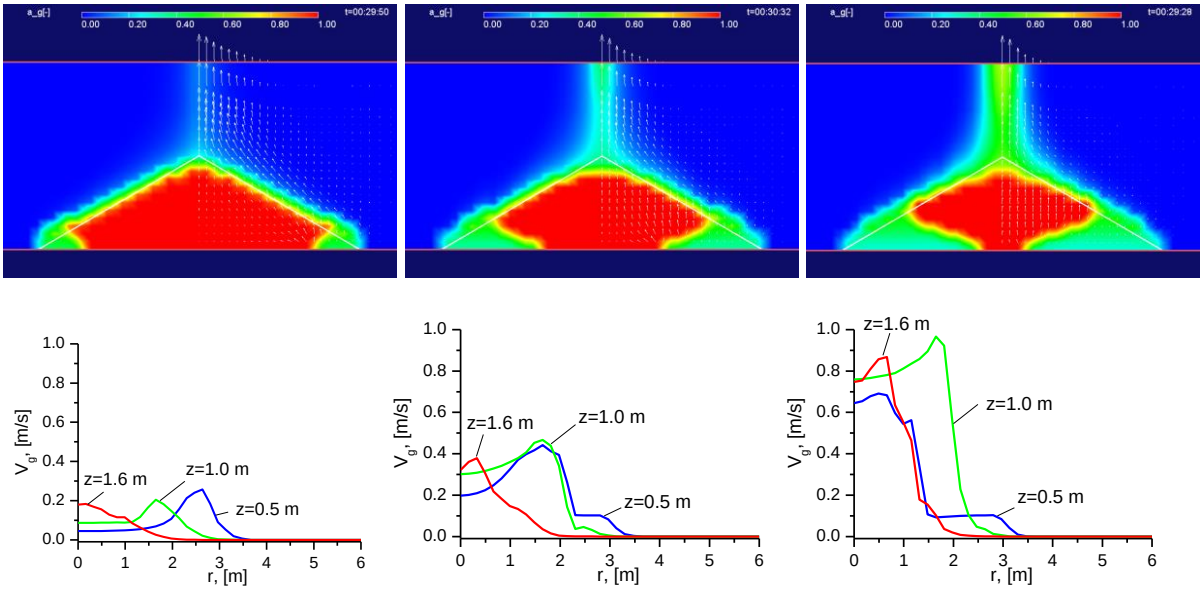

Figure 22: Void fractions after 30 min in initially dry debris beds with particle diameters 1,1.5, and 2 mm (left-to-right)

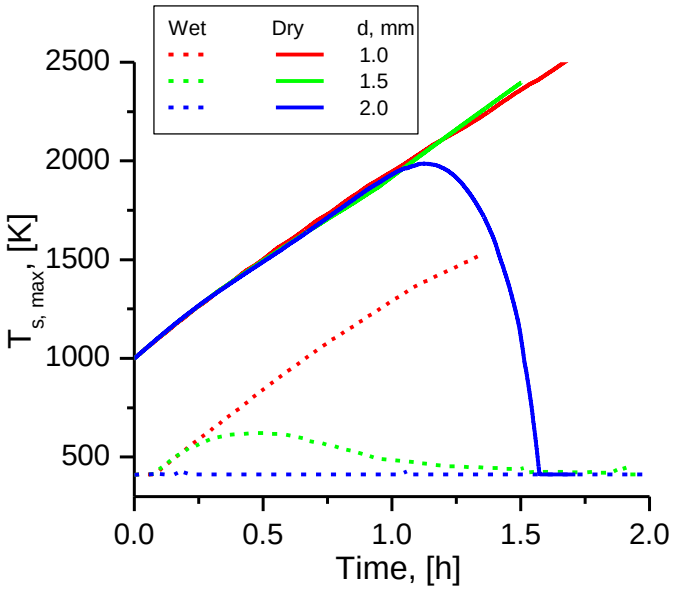

Figure 23: Maximum temperatures of solid particles.in initially dry and wet debris beds

The temperature time histories presented in Figure 23 show that for initially dry debris bed, material reheating proceeds at the same rate, reflooding observed only for 2 mm particles. Initially wet debris bed is coolable, or is reflooded for particles larger than 1 mm.

3.9 Application of DECOSIM to In-vessel Debris Beds

Being based on a generic set of conservation equations, DECOSIM can also be applied to modeling of debris beds formed in the reactor pressure vessel. This research activity extends the research area to problems and scenarios when heat-releasing porous debris bed can be expected to be formed due to molten corium fragmentation inside RPV [75].

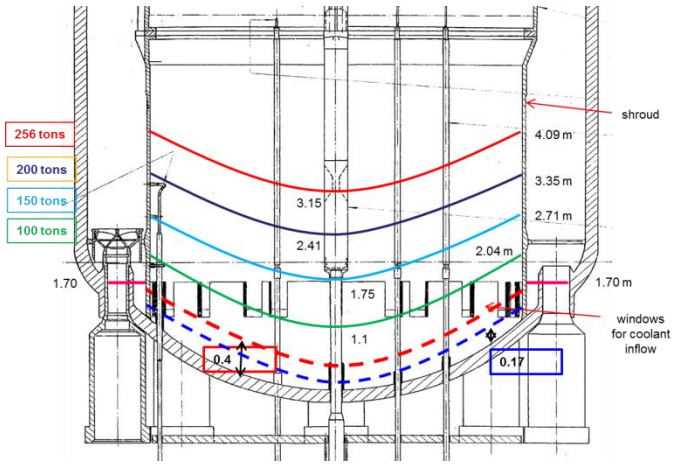

Figure 24: Sketch of reactor pressure vessel geometry and assumed debris bed shape.

From the risk perspective, it is important to quantify or bound the uncertainties associated with the in-vessel debris bed coolability, reheating and remelting. Coolability of a porous in-vessel debris bed, its possible reflooding or heating up and remelting were studied using DECOSIM code. The results obtained were analyzed with respect to the possible vessel failure modes. Vessel geometry of a reference design of Nordic-type BWRs used in simulations is sketched in Figure 24.

More than a hundred of control rod guide tubes (CRGTs) and instrumentation guide tubes (IGTs) are located in the vessel lower head. On one hand, they can be used to provide water inflow into the in-vessel debris bed, but, on the other hand, if cooling is absent or ineffective, the tubes can fail providing flow path for the escape of corium from the vessel. The presence of these tubes was taken into account in the mathematical model by allowing for the volume taken by the tubes, as well as for their heat capacity affecting the temperature increase rate.

Simulations were carried out for the following debris bed properties:

- Particle diameter $d = 1 - 3$ mm;

- Porosity $\varepsilon = 40\,\%$;
- Total mass of debris bed: $M = 100 - 200$ t;

Scenario-dependent parameters:

- System pressure: 3 bar (was set on the top of the computational domain located 4 m above the RPV bottom point).

Due to uncertainty in the initial state of the debris bed, two cases were considered: i) initially quenched (wet) debris bed at the saturation temperature, heated by the decay heat, and ii) initially hot dry debris bed at the initial temperature 1000 K, possessing significant initial latent heat.

For initially quenched debris bed, simulations have shown that debris bed coolability is strongly affected by the particle diameter. For 3 mm particles, the debris bed was coolable for all melt masses and relocation times; local dryout did not occur and cooling of the material was provided by water evaporation, so that the maximum temperature of the solid particles was maintained close to the local saturation temperature. For 2 mm particles, the local dryout was observed for the largest mass of debris bed $M = 200\,\text{t}$ at the relocation time $t_r = 1.5\,\text{h}$, however, in this case the maximum deviation of particle temperature from the saturation temperature was about 50 K, and after about 1 hour the dry zone was reflooded again, after which the solid material temperature remained close to saturation. For 1 mm particles, debris bed coolability depends on the total mass M and relocation time t_r. Results of simulations are summarized in where time histories of the maximum temperature of solid material are shown for 1 mm particles; also, one curve (dotted line) is also shown for 2 mm particles in the above-mentioned case where temporary dryout occurred in the debris bed. Solid lines correspond to the relocation time $t_r = 1.5\,\text{h}$, dashed lines were obtained for $t_r = 3.0\,\text{h}$.

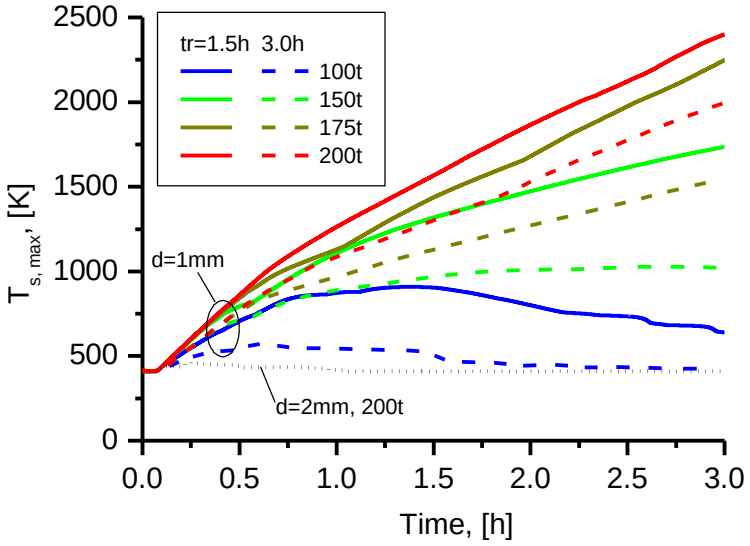

Figure 25: Time histories of maximum temperature of solid material in initially quenched debris bed.

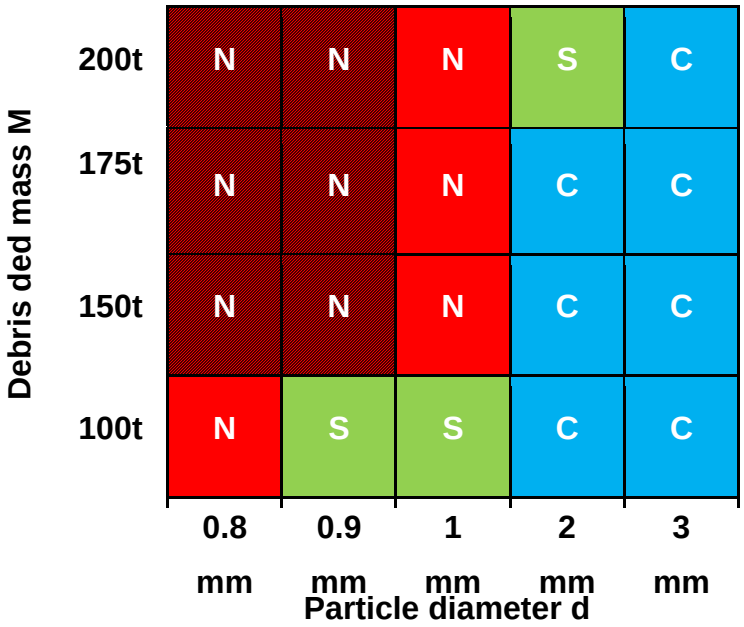

Figure 26: Summary of coolability results for initially quenched debris bed. N: non-coolable with temperature escalation, S: dryout with temperature stabilization, C: coolable (no dryout, or dryout followed by reflooding)

Coolability results for initially wet (quenched) debris beds are shown in Figure 26. where color coding is use to mark the cases where temperature escalation (red), temperature stabilization (green), or “no dryout” or “dryout followed by reflooding” (blue) was observed

within 3 hours after core relocation. The calculated solid particle temperature distributions at time 10800 s after relocation are shown in for debris bed masses of 200, 150, and 100 t, with the debris bed shape shown by the white lines. In all cases the particle diameter was $d = 1\,\text{mm}$, the relocation time for the smallest and largest debris masses was $t_r = 1.5\,\text{h}$, while for the intermediate mass of 150 t results are shown in the case of $t_r = 3.0\,\text{h}$

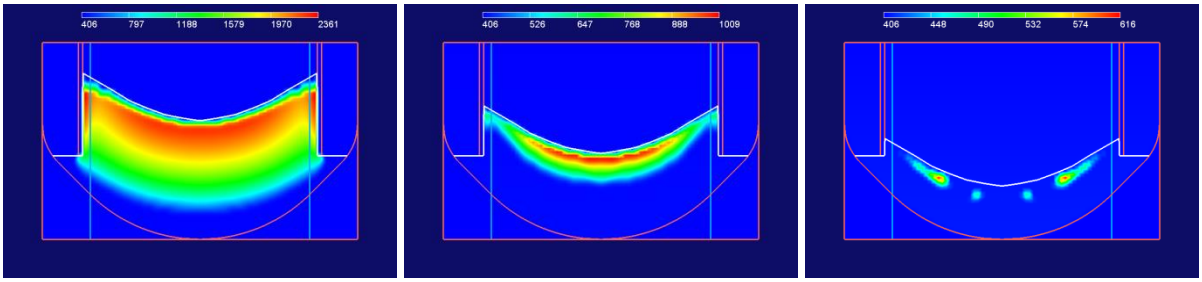

Figure 27: Particle temperature in initially quenched debris bed at time 10800 sec after relocation. Left: $M = 200\,\text{t},\ d = 1\,\text{mm},\ t_r = 1.5\,\text{h}$; Middle: $M = 150\,\text{t},\ d = 1\,\text{mm},\ t_r = 3.0\,\text{h}$; Right: $M = 100\,\text{t},\ d = 1\,\text{mm},\ t_r = 1.5\,\text{h}$

It can be seen from Figure 27 that for the initially quenched debris bed dryout develops in the upper zone of the debris bed where the vapor flowrate is the highest and, therefore, water penetration into it is more difficult. In the large debris bed, the dry zone is gradually reheated because vapor flow through it is insufficient for removal of the decay heat from solid particles; it can also be seen that the sizes of the dry zone are gradually increasing. For smaller debris beds, temperature stabilization or gradual decrease occur due to vapor cooling and gradual decrease in the decay heat power.

For initially dry debris bed, six cases are considered: debris beds with masses of $M = 100$ and 150 t and particle diameters of 1 and 2 mm, as well as debris mass $M = 200\,\text{t}$ and particle diameters 2 and 3 mm; relocation time $t_r = 1.5\,\text{h}$. In each case, the debris bed had initial temperature of 1000K and was initially filled with vapor at the same temperature as solid material. The space above the debris bed is filled with saturated water.

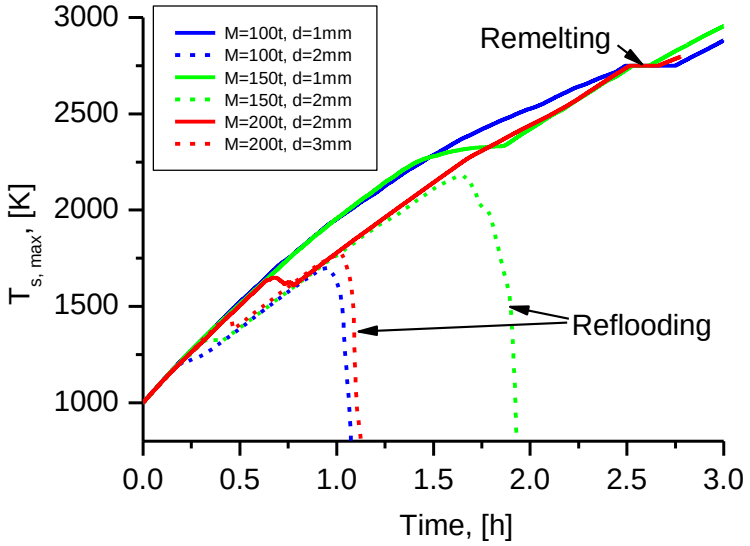

Figure 28: Time histories of maximum temperature of solid material in initially dry debris bed with initial temperature 1000 K.

In Figure 28, time histories of maximum temperature of solid material are presented for the six simulated cases. It can be seen that initially the temperature rise rate is exactly the same in all cases, and the maximum temperature rise occurring near the shroud where no congesting structures is available; the jump in the temperature rise rate clearly visible for 2 and 3 mm particles at times between 0.25 and 0.75 hours occurs because these regions are getting quenched by the incoming water, and afterwards the maximum temperature is reached in the congested volume where the temperature rise rate is lower. For larger particles, as can be seen from the dashed lines in Figure 28, total reflooding of the debris bed occurs after 1–2 hours, and the maximum temperature of solid material falls down to the saturation temperature. For 1 mm particles, as well as for 2 mm particle and corium mass of 200 t, high drag prevents incoming water from reflooding the whole volume of the debris bed, and steady temperature rise can be observed to the levels where remelting of the material can occur. The time to reach remelting is approximately 2.5 h after core relocation or 4 h after SCRAM.

The temperatures of solid particles at time 10800 sec after relocation (top row) and the corresponding melt fraction (bottom row) are shown for different masses of debris bed in Figure 29. Evidently, in the last two cases, remelting and high temperatures are reached in the bottom part of the debris bed in the vicinity of the vessel wall. Thus the welding points of CRGTs and IGTs penetrations can fail, resulting in possibly early opening of the flow path for

the melt ejection from the lower head. For the first case, with melt mass 200 t and particle diameter 2 mm, liquid melt starts to accumulate in the top part of the bed, while the vessel and penetrations can fail later then in the other two cases.

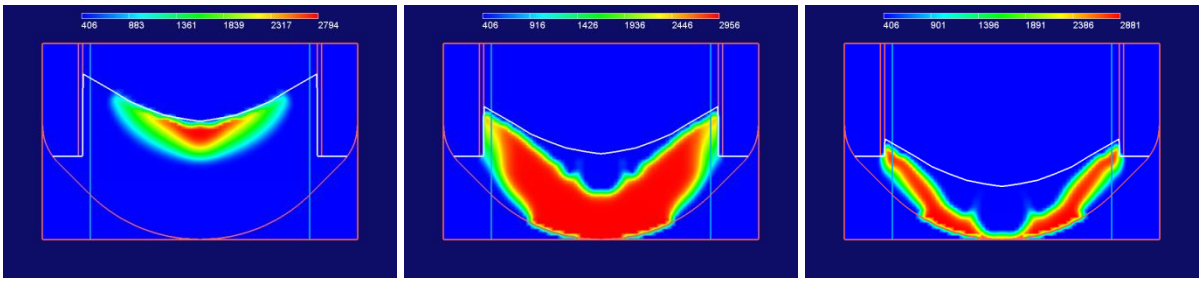

Particle temperatures

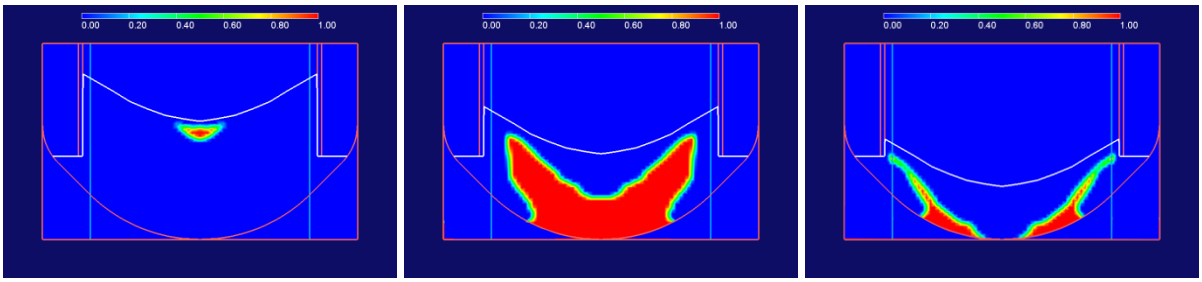

Melt fractions

Figure 29: Particle temperature (top row) and melt fraction (bottom row) in initially dry debris bed at time 10800 sec after relocation. Left: $M = 200\,t,\ d = 2\,mm,\ t_r = 1.5\,h$; Middle: $M = 150\,t,\ d = 1\,mm,\ t_r = 1.5\,h$; Right: $M = 100\,t,\ d = 1\,mm,\ t_r = 1.5\,h$

The simulation results show that post-dryout behavior of a non-coolable in-vessel debris bed can result in different scenarios:

- Temperature escalation and material remelting in the upper part of debris bed, and delayed contact of liquid melt with reactor wall or CRGTs and IGT welds;
- Temperature escalation and remelting of debris bed in the direct proximity of the RPV wall leading to possible earlier failures of CRGTs and/or IGTs.

Accordingly, in the former case one can expect formation of melt pool in the top part of debris bed, with subsequent downward melting zone propagation. Massive melt release can be an outcome in the case of RPV failure. In the latter case, early failure of CRGTs and IGTs can result in gradual melt release from RPV. In such dripping mode of melt release the risk of formation of agglomerated non-coolable debris bed as well as the risk of energetic steam explosion can be significantly reduced.

4 Investigation of particulate debris spreading

4.1 Introduction

In a Nordic BWR type reactors the lower drywell flooded with water is the last barrier to prevent basemat penetration and escape of fission products into environment in a hypothetical severe accident (SA) with molten corium released from the reactor vessel (RV). Being discharged into several meters deep water pool, the molten corium is subject to fragmentation and quenching. The fragmented particles sedimentation process leads to the formation of a porous debris bed on the pool basemat. The corium debris bed re-melting by the decay heat can be avoided if the latter is removed by the natural circulation and evaporation of the coolant. Both the theoretical and numerical analyses [76], [68], as well as experimental studies [62] for their validation, have been performed in order to determine the time scale of the dryout as well as its influencing factors such as: properties of the debris bed (particles size, bed porosity, bed geometry, etc.) and SA scenario conditions (e.g. system pressure). A typical geometry of the formed debris bed is a mound. The studies performed suggested that geometrical configuration of the debris bed is one of the main factors influencing the bed coolability. A tall debris bed can hardly be coolable and, in contrast, the same mass of the corium material can be easily cooled if the debris is spread uniformly over the whole available basemat area [76].

The shape of the debris bed is affected by particle transport:

i. after settlement on the debris bed (relevant tests nomenclature is PDS-C);
ii. in the water pool above the bed (relevant tests nomenclature is PDS-P).

Debris bed self-leveling occur due to mechanical energy originated from the coolant boiling in the porous bed (see illustration in Figure 30). Pioneering experiments conducted with metallic powders showed that indeed coolant boiling promotes debris self-leveling, influences the horizontal velocity of the vertically falling particles affecting the repose angle of the bed [3]. It should be noted that the pool can remain mostly subcooled in some reactor accident scenarios, it is quite possible that boiling will start rather early in the top part of the hot water plume stemming from the debris bed when hot water will approach to the surface and its temperature can exceed local saturation temperature according to the hydrostatic head. This effect was demonstrated in [72]. In recent studies [20], the influence of two-phase flow on

sedimentation of the different in size particles has been shown experimentally. The relevant numerical approaches and codes employing discrete element analysis are also in the active development [30], [77].

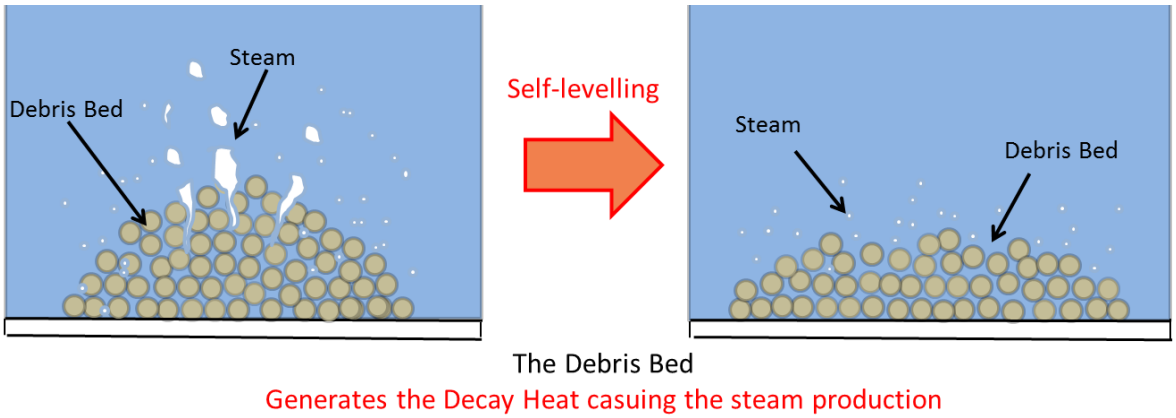

Figure 30: Illustration of self-leveling process

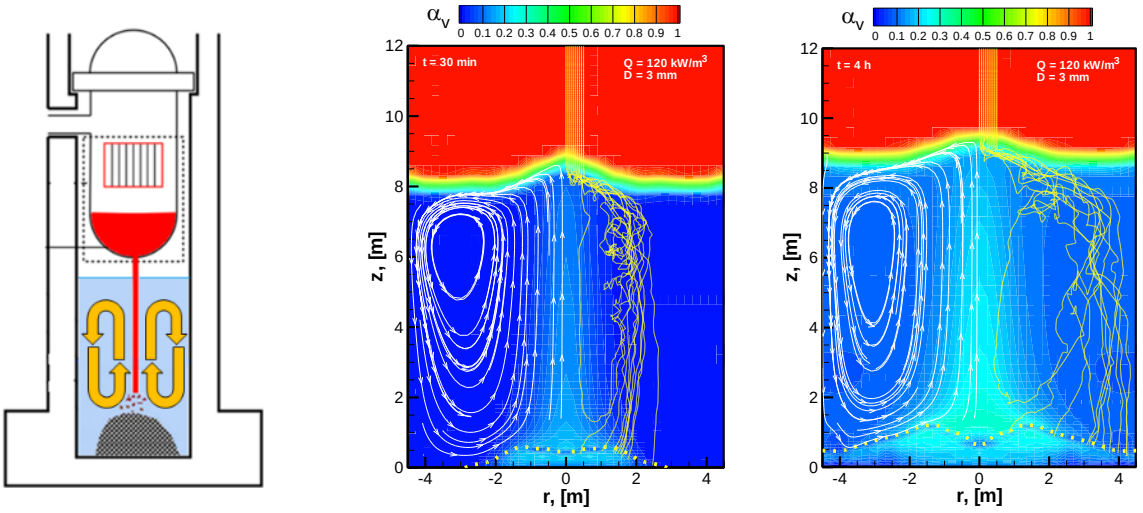

Figure 31: Illustration of the large turbulent currents during corium debris release in RV cavity under SA conditions (a) and simulation of particle trajectories affected by the circulation in the saturated pool at 30 min (b) and 4h (c), after [68].

The effectiveness of the particulate debris bed spreading has been considered in experimental and theoretical studies [78] [79] [8] [21] [5] [4] [53]. As experimental studies showed, the debris self-leveling occurs due to particle motion at the top layer of the debris bed [21]. The large scale turbulent flows (as illustrated in Figure 31a) may affect the particle lateral spreading over the basemat [68] preventing formation of a tall debris bed. Smaller particles are more effectively transported by the flow. In Figure 31(b-c) from [68] the flow field (white

lines on the left), void fraction distribution (color map), particle trajectories (yellow lines) and bed shape (dashed line) are presented for simulation time 30 minutes and 4 hours. The debris bed is spread over the bottom of the pool, despite the fact that all particles are released from a relatively small source near the axis.

In this work a separate effect studies are carried out concerning the particulate debris spreading. The experimental results for debris bed self-leveling and corresponding scaling modeling (PDS-C) as well as first studies on particle spreading in the pool (PDS-P) are presented in the following two sections.

4.2 PDC-C tests: closure scaling model on particular debris spreading

In our previous work [21] several PDS (Particulate Debris Spreading) facilities were used with gas injection provided at the bottom of the debris bed in order to study spreading phenomena at prototypic gas velocities and different length scales and spatial configurations. The most important observations from the earlier PDS tests [21] are:

1. Local slope angle of the debris bed depends on local gas velocity. For instance, Figure 32 shows debris bed shape after gas injection was provided in the central section (indicated by two vertical dashed lines). Remarkably, the slope angle changed only in this middle section, while initial slope angle remained unchanged in the other parts of the bed.
2. The bulk volume of the debris bed is immovable. The particles are moving only in the topmost layer of the bed. Video recording of the debris bed spreading process demonstrated that the thickness of the moving layer is of the order of few particle diameters.

Observed behavior was insensitive to the scale and spatial configuration of the facility, mass of the debris, and gas flux until debris bed fluidization limit is reached. The fact that local gas-coolant-particle interactions in the thin top layer of particles are responsible for spreading suggests that experiments in reduced size laboratory facilities (such as PDS) can be used to capture the key relevant physical phenomena. Experimental closures for particle mass flow rate per unit width of the bed (referred as “particulate flow rate” for the sake of brevity) as a function of local slope angle and gas velocity have been obtained at different test conditions and for different particle types [5] [21]. Using such closures an approach for predicting spreading dynamics of a debris bed with arbitrary initial shape was proposed. However, if the data produced in such tests is expressed in the dimensional form, it can be directly applicable

to estimation of the particle spreading flow rate in accident conditions only if the properties of the particles and coolant (such as particle size distribution, morphology, density, coolant density, viscosity, etc.) are the same as the prototypic ones. Also, for each new type of particles and gas flow conditions, a separate set of experiments is necessary in order to provide data on the dimensional particle flow rate.

The goal of this work is to develop a scaling approach to generalize the experimental data for prediction of the particle flow rate for different kinds of particles and gas flow conditions.

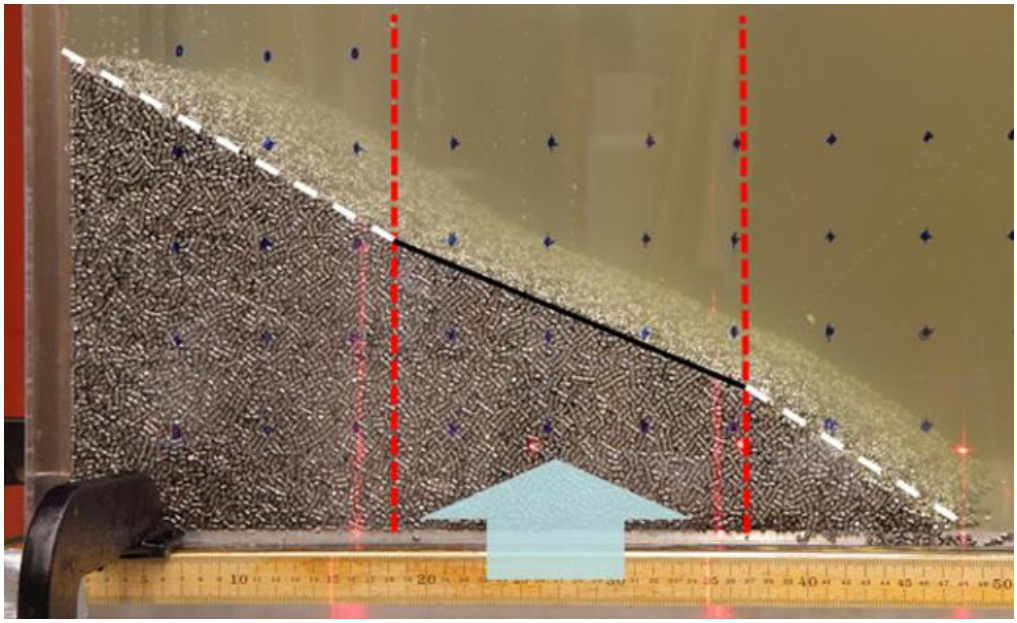

Figure 32: The slope angle of the heap is changed only above the section where gas injection was provided (between the two vertical dashed lines).

4.2.1 Experimental approach and results

Particulate Debris Spreading Closures (PDS-C) experimental facility is designed to study phenomena of particulate debris spreading caused by upward two phase (water and gas) flow. The facility is composed of a vertical rectangular open on top test section, made of acrylic glass with internal dimensions as length L=405 mm, width W=72 mm, height H=915 mm. Gas injection chamber (with dimensions 405x72 mm) is installed at the bottom of the test section and connected to the constant 8 bar pressure compressed air supply system, the schematic shown in Figure 33. A camera is used to record evolution of the heap shape in each experiment. The compressed air at pressure up to 2 bar (set by the pressure regulator) is

supplied through the injection chamber. The top plate of the chamber is a perforated with 287 (7x41) cylindrical orifices 1.5 mm in diameter positioned as a quadratic grid with 10 mm pitch. The plate can provide uniform and constant in time air injection with up to 70 L/s total flow rate, which corresponds to gas superficial velocity of 2.4 m/s. The gas flow rate is regulated by valve-3 and measured by an in-line flow meter Omega FL-505.

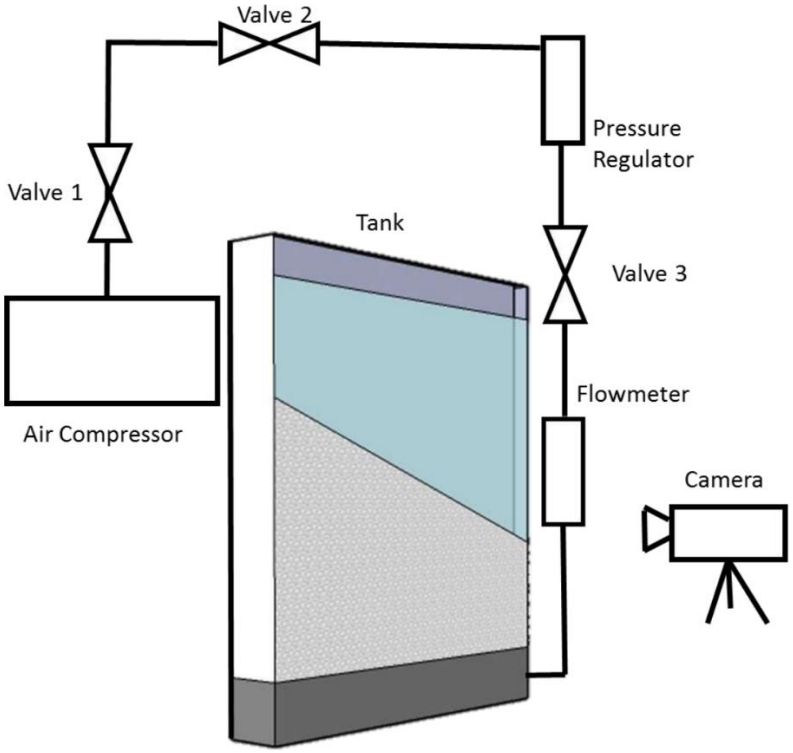

Figure 33: Schematic diagram of the PDS-C facility.

The total volume of particulate debris bed typically used in each test is about 8.5 liters. Different types of particles were used in the test series: stainless steel (SS) cylinders: 3 mm in diameter and 3 mm long; 3 mm in diameter and 6 mm long; SS spheres: 1.5 mm, 3 mm, and 6.0 mm in diameter; and different mixtures of these particles, i.e. a mixture of SS 1.5 mm spheres and SS 3x3 mm cylinders; and a mixture of SS 3 mm spheres and SS 6.0 mm. The properties of the particles are summarized in Table 9.

The experimental procedure for a typical PDS-C test consists of following steps:

1. Particles are loaded into the facility test section.
2. The test section is filled with water up to the level of 550 mm from the top of the air injection plate.
3. The particles bed is shaped as a heap with a slope angle close to the critical angle of repose.

4. The debris bed is held in its initial shape using a stiff stainless steel net when gas injection is activated in order to avoid a “water piston” effect. The effect (also noticed by Cheng et al., 2013) is observed at the start of gas injection when liquid (which initially fills the pores in the bed and the gas chamber) is pushed as a “piston” by the gas injected at high velocity causing rapid motion of the whole debris bed.
5. Gas injection flow rate is gradually adjusted to reach the desired superficial air velocity.
6. Then the net is quickly removed in upward direction allowing particles to start the spreading process.

The runtime of experiments can vary from tens of seconds up to 5 minutes. The entire test is recorded by a video camera. Individual frames are extracted and analyzed later on, using following image processing technics. First, the noise reduction algorithm is applied and frames are converted to black-white images. The Sobel edge detection algorithm is applied in order to detect the top edge of the bed. The image of the bed is split into two parts (left and right) by a centerline. The areas of the left and right parts of the bed (A_l and A_r respectively) under the edge are calculated (Figure 34).

Table 9: Particles properties

Particle	Equivolume sphere diameter (d_p) [mm]	Material density (ρ_p) [kg/m^3]	Angle of repose at $U_g = 0$ (θ^0_{rep}) [°]	Minimum fluidization velocity (U_{mf}) [m/s]	Sphericity (Φ) [-]	Porosity (ε) [-]
SS cylinders 3x3 mm	3.4	7800	33.0	2.44	0.87	0.35
SS cylinders 3x6 mm	4.3	7800	36.5	2.79	0.83	0.36
SS spheres	1.5	7800	22.0	1.43	1.0	0.40
SS spheres	3.0	7800	22.0	2.27	1.0	0.40
SS spheres	6.0	7800	22.8	3.34	1.0	0.40
Mixture 1[a]	2.6	7800	29.5	2.07	0.97	0.33
Mixture 2[b]	2.1	7800	24.5	1.80	0.98	0.34
Mixture 3[c]	4.0	7800	24.0	2.68	1.0	0.36

[a] is composed by SS spheres 1.5 mm (volume fraction 0.25, mass fraction 0.23) and by SS cylinders 3 by 3 mm (volume fraction 0.75, mass fraction 0.77)

[b] is composed by SS spheres 1.5 mm (volume fraction 0.5, mass fraction 0.48) and by SS cylinders 3 by 3 mm (volume fraction 0.5, mass fraction 0.52)

[c] is composed by SS spheres 3.0 mm (volume fraction 0.5, mass fraction 0.5) and by SS spheres 6 mm (volume fraction 0.5, mass fraction 0.5)

The A_l and A_r areas obtained from the frames of the recorded video data, are used to calculate the particle mass flow (Q_p) at given local angle of the heap slope (α) and experimental conditions (gas superficial velocity, particle properties, etc.):

$$Q_p^n = \rho_p \cdot (1-\varepsilon) \cdot \frac{A_n^{t1} - A_n^{t2}}{(t2-t1)}, \tag{4.1}$$

$$\alpha = \frac{1}{2}\text{atan}\left(\frac{A_l^{t1} - A_r^{t1}}{\left(\frac{L}{2}\right)^2}\right) + \frac{1}{2}\text{atan}\left(\frac{A_l^{t2} - A_r^{t2}}{\left(\frac{L}{2}\right)^2}\right)\cdot, \tag{4.2}$$

where n indicates the heap side : $n = l, r$, ρ_p is the particle material density, ε is the porosity of the bed and L the facility length.

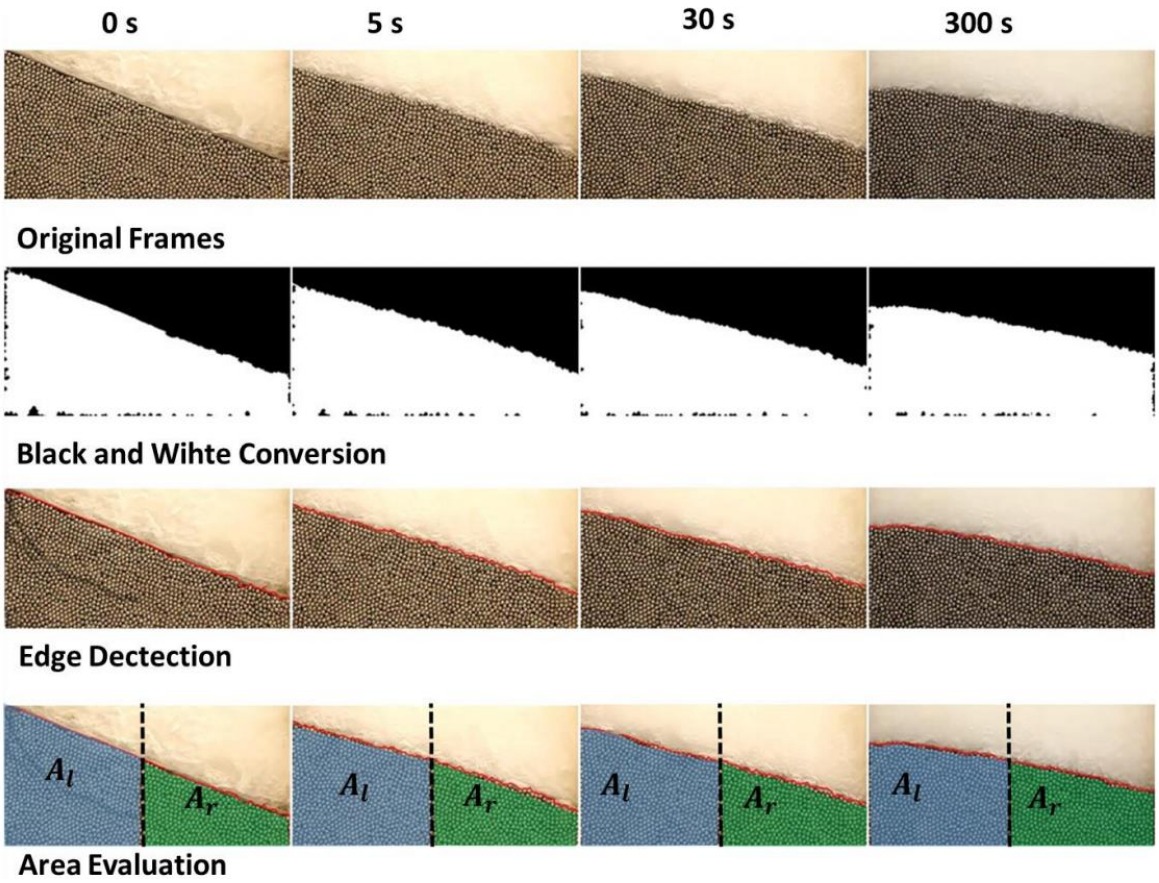

Figure 34: Stages of the video image post-processing technique employed for estimation of the particle flow rate (PDS-C8 test).

The areas calculated from each frame are averaged with 1 second interval in order to reduce the noise in the data due to possible random errors in the edge detection for each individual frame. Then, time intervals $[t1,\ t2]$ are selected automatically to ensure that statistically significant number of particles moves across the centerline during each time interval. We found that ~5 particles crossing the centerline during the time interval is necessary in order to obtain a monotonic dependency of the particle flow on the local slope angle.

The experimental error in the particle mass flow can be estimated as:

$$Q_p^{err} = Q_p^l + Q_p^r, \tag{4.3}$$

When superficial air velocity reaches minimum fluidization velocity (U_{mf}) the force exerted on the bed by the flowing media is sufficient to fluidize the entire bed. Minimum fluidization velocity for 3-phase flow can be calculated by Eq. (4.4), where Re_{gmf} is the so called "gas particle" Reynolds number obtained according to the empirical correlation proposed by Lucas et al. [45] for round particles, since all our particles have a sphericity between 0.8< Φ <1 and reported in Eq. (4.5).

$$U_{mf} = \frac{\mu_g \cdot Re_{gmf}}{\rho_g \cdot d_p} \tag{4.4}$$

$$Re_{gmf} = \sqrt{29.5^2 + 0.0357 \cdot Ar_{lg}} - 29.5 \tag{4.5}$$

In Eq. (4.5) we use the gas phase Archimedes number with liquid-buoyed solids (Ar_{lg}) (Eq. (4.6)) in order to take in account the effect of the liquid phase, as it is proposed by Zhang et al. (1998).

$$Ar_{lg} = \rho_g \cdot (\rho_p - \rho_l) \cdot g \cdot d_p^3/\mu_g^2 \tag{4.6}$$

where μ_g and ρ_g are gas dynamic viscosity and density respectively; ρ_l is the liquid density; d_p is equivolume sphere diameter. In the experiments with mixtures of different particles, d_p

was assumed to be equal to the mean reciprocal diameter as it is suggested by Wen-Ching Yang [77]:

$$d_p = \frac{1}{\sum_{i=1}^{N}\left(v_i/d_{p_i}\right)} \tag{4.7}$$

where v is the volume fraction of respective particles in the solid mixture. The gas injection normalized velocity (Q_g) is defined as a ratio of the gas superficial velocity (U_g) to the minimum fluidization velocity (U_{mf}).

$$Q_g = \frac{U_g}{U_{mf}} \tag{4.8}$$

The experimental matrix is provided in Table 10. For each test condition there were 2 or 3 tests were carried out to ensure repeatability. The particulate flow rate as function of the slope angle was obtained using Eq. (4.1) and Eq. (4.2) for each experiment performed at fixed gas flow rate. An example of such dependency is shown in Figure 35, while in Figure 36 the complete set of the experimental results is reported. For instance, Figure 36 shows the spread of the data due to different test conditions, particle properties as well as experimental error (Eq. (4.3)). Experimental observations suggest that spreading is much faster (especially at high air superficial velocity) at the initial stage of the test, when slope angle is large. Similar observations also have been made by Cheng et al. [9].

Table 10: Test matrix of PDS-C experiments

Particle type	U_g [m/s]	Q_g [-]	Experiment
SS cylinders 3x3 mm	0.34	0.14	PDS-C01
	0.52	0.21	PDS-C02
	0.86	0.35	PDS-C03
	1.38	0.56	PDS-C04
	1.91	0.78	PDS-C05
SS cylinders 3x6 mm	0.17	0.06	PDS-C06
	0.34	0.12	PDS-C07
	0.52	0.18	PDS-C08
	0.69	0.24	PDS-C09
	0.86	0.31	PDS-C10
SS spheres 1.5 mm	0.17	0.12	PDS-C11
	0.34	0.24	PDS-C12
	0.86	0.60	PDS-C13
	1.04	0.72	PDS-C14
SS spheres 3.0 mm	0.17	0.07	PDS-C15
	0.34	0.15	PDS-C16
	0.69	0.30	PDS-C17
	1.56	0.68	PDS-C18
SS Spheres 6.0 mm	0.17	0.05	PDS-C19
	0.52	0.15	PDS-C20
	0.86	0.26	PDS-C21
	1.04	0.31	PDS-C22
	1.21	0.36	PDS-C23
	1.56	0.46	PDS-C24
	1.73	0.52	PDS-C25
Mixture 1	0.69	0.33	PDS-C26
	1.04	0.50	PDS-C27
Mixture 2	0.34	0.19	PDS-C28
	0.69	0.38	PDS-C29
	1.04	0.57	PDS-C30
Mixture 3	0.17	0.06	PDS-C31
	0.34	0.13	PDS-C32
	0.52	0.19	PDS-C33
	0.86	0.32	PDS-C34
	1.21	0.45	PDS-C35
	1.38	0.51	PDS-C36
	1.56	0.58	PDS-C37
	1.73	0.64	PDS-C38

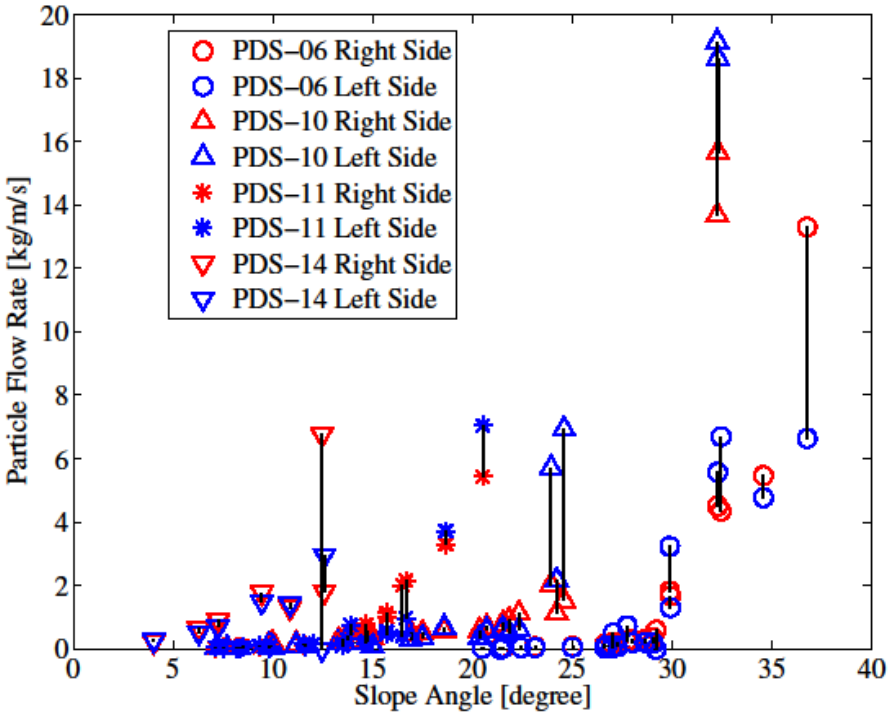

Figure 35: Particulate flow rate per unit width as function of heap slope angle obtained for selected PDS tests.

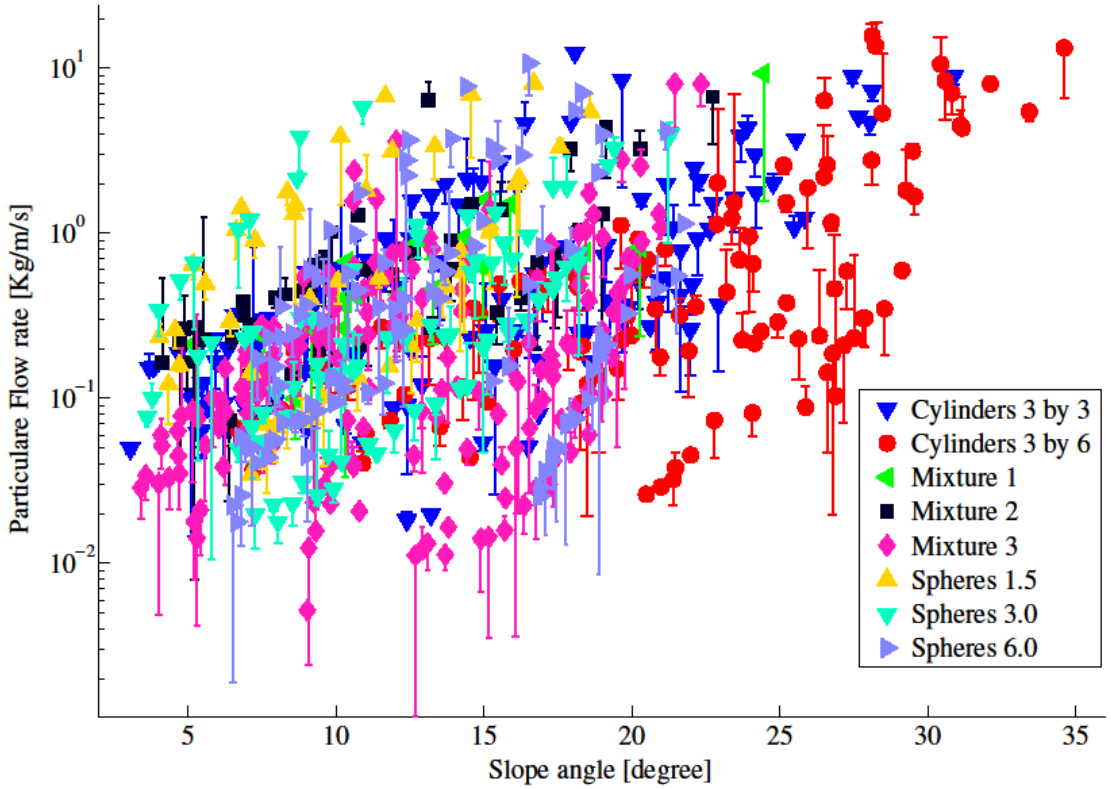

Figure 36: Particle flow rate as a function of slope angle for all the PDS-C experiments.

4.2.2 Development of scaling approach

In this work, our aim is to develop a universal scaling approach for generalizing empirical data on particle spreading rate at different gas injection conditions. Obtained non-dimensional closures for particle spreading rate should be valid for different particle properties.

The self-leveling phenomenon is a particular case of a more general problem of three phase gas–liquid–particle flow. In Figure 37 the main forces acting on the particles are shown schematically: (i) buoyancy (F_B), (ii) aerodynamic drag (F_D), (iii) gravity (F_G), and (iv) inter-particle friction (F_{Fr}). Given that average particle spreading velocity is relatively slow we neglect inertia forces. We also do not consider capillary and cohesion forces, which can become important for very small particles. The two-phase coolant flow drag counteracts with gravity and friction forces leading to spreading and reduction of the repose angle, as shown by Eames and Gilbertson [13]. At some point the drag can overcome the gravity force leading to fluidization of the bed.

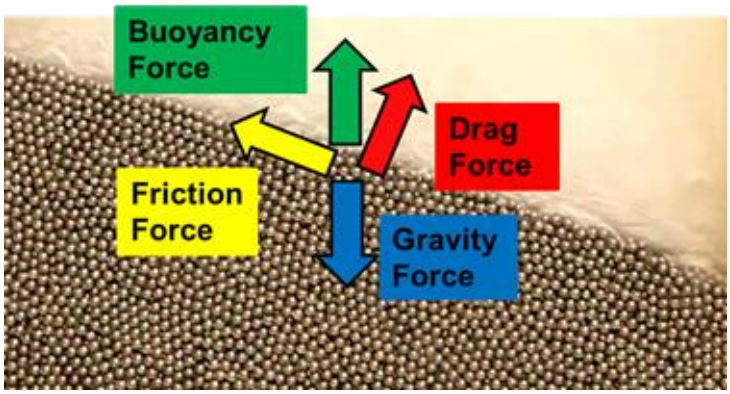

Figure 37: Balance between main forces acting on a particle in the debris bed.

The particle flow rate should be a function of the main forces:

$$Q_p = f(F_D, F_B, F_{Fr}, F_G), \tag{4.9}$$

or, equivalently, a function of the parameters which determine the forces:

$$Q_p = f\left(d_p, U_g, \rho_p, \rho_l, \rho_g, \mu_g, \mu_l, g, \alpha, k_{Fr}\right), \tag{4.10}$$

where α is a local slope angle; $k_{Fr} = \tan\theta_{rep}(Q_g)$ is friction coefficient which is a function of gas flow rate and for the coarse, cohesion-less materials is equal to the tangent of the repose angle [13]:

$$\theta_{rep}(Q_g) = \theta_{rep}^0 - arcsin \left(\frac{C_d(Re)\cdot Q_g|Q_g|}{C_d(Re_{gmf})} sin(\theta_{rep}^0)\right) \quad (4.11)$$

where Q_g is the gas injection normalized velocity (Eq. (4.8)); $\theta_{rep}^0 = \theta_{rep}(0)$ is critical repose angle of a particle heap [49] at $Q_g = 0$; C_d is the aerodynamic drag coefficient; Re and Re_{gmf} are respectively the particle Reynolds number at U_g and at U_{mf}. Eq. (4.10) can be represented with five independent non-dimensional combinations of the parameters

$$F\left(\frac{Q_p}{(\rho_p-\rho_l)\cdot\sigma/\mu_l\cdot d_p}, Q_g, Ar_{lg}, \frac{tan\,\theta_{rep}(Q_g)}{tan\,\theta_{rep}^0}, \frac{tan\,\alpha}{tan\theta_{rep}(Q_g)}\right)=0 \quad (4.12)$$

In this work we use following expression for the normalized non-dimensional particle spreading rate Q_p^*

$$Q_p^* = \frac{Q_p}{(\rho_p - \rho_l)\sigma/\mu_l \cdot d_p} = K \cdot {Q_g}^a \cdot {Ar_{lg}}^b \cdot \gamma^c \cdot \beta^d \quad (4.13)$$

where normalized friction force (γ) and normalized slope angle (β) are:

$$\gamma = \frac{tan\,\theta_{rep}(Q_g)}{tan\,\theta_{rep}^0} \quad (4.14)$$

$$\beta = \frac{tan\,\alpha}{tan\,\theta_{rep}(Q_g)} \quad (4.15)$$

In eq. (4.13) the Ar_{lg} represents the effect of gravitational and buoyancy forces, Q_g the effect of aerodynamic drag and finally γ and β describe friction forces. Larger particles made of denser material will resist to the spreading according to the effect of the Archimedes number in Eq. (4.13) and as it was observed by Cheng et al. [8].

Based on the PDS-C experimental data, the constants K, a, b, c and d are evaluated by performing regression analysis (RA). Two separate RAs were necessary in order to represent different regimes of particle spreading: rapid avalanche and slow particle spreading. The resulting fit coefficients are shown in Table 11.

Table 11: Empirical constants in Eq. (4.13)

Q_p^*	K	a	b	c	d
<0.0024	3.356	1.089	-0.325	2.628	4.306
>0.0024	0.159	0.432	-0.162	1.366	0.876

The dimensionless Eq. (4.13) reflects importance of different forces, which can be expressed as following:

$$Q_p \sim \frac{F_D \cdot F_B}{F_{Fr} \cdot F_G}. \tag{4.16}$$

I.e. the larger gravity and friction forces (larger Ar_{lg} and smaller β in Eq. (4.13)) will reduce particle flow rate, and vice versa, higher drag force and buoyancy (larger U_g and smaller Ar_{lg} in Eq. (4.13)) will increase particulate flow rate.

Finally, the obtained expression is used to verify its capability to predict correctly the dynamics of the heap slope angle. Parameter $R(t)$ is introduced and defined as the ratio between the heap slope angle at time t and the repose angle at zero gas velocity Eq. (4.17) :

$$R(t) = \frac{\alpha(t)}{\theta_{rep}^0} \tag{4.17}$$

Parity plot of predicted and experimental $R(t)$ is presented in Figure 38, here $R(t)$ is shown illustratively at 5% 10% 20% 50% 80% of the total spreading time in the experiment. The data points from all experiments with different particles and particle mixtures are clustered along the diagonal of the plot, suggesting that proposed scaling approach captures most important physical phenomena and can predict the debris bed self-leveling behavior. A greater difference is observed for larger particles. Further experimental studies of the effects of the particle density, particle size and surface tension on Q_p would be necessary to clarify the

reasons. For instance, different ratios between the gravity, drag, fraction and surface tension forces can be studied by using particles of the same dimensions but different densities and morphologies.

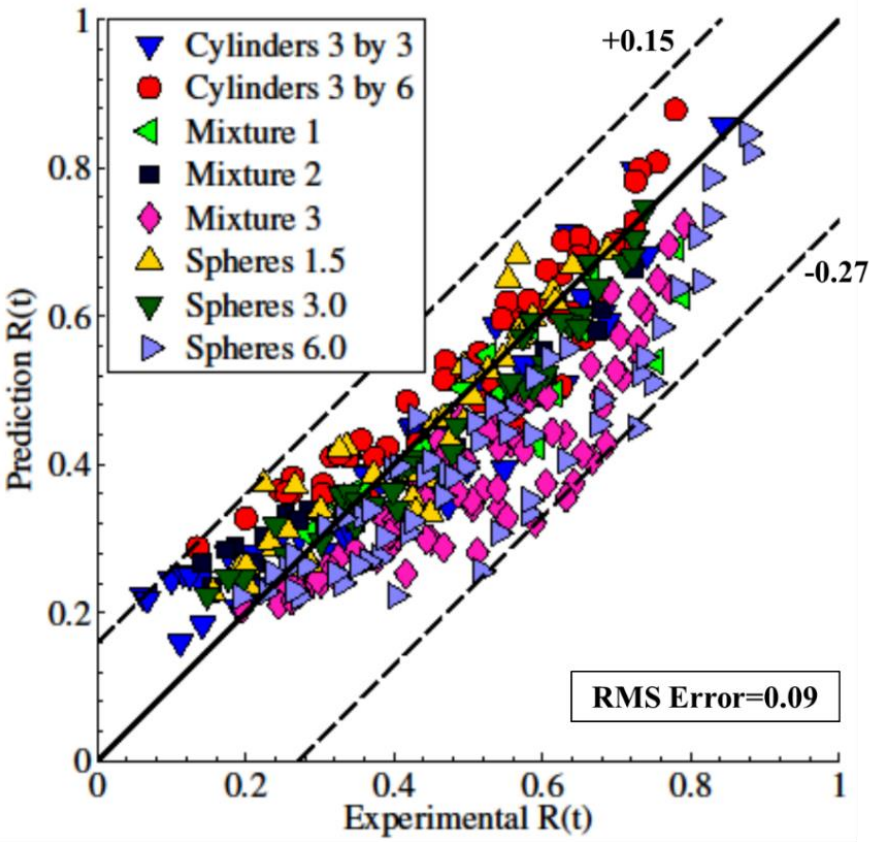

Figure 38: Comparison between predicted and experimental R(t) in the PDS-C experiments. R(t) is calculated at 5%, 10%, 20%, 50% and 80% of the total experimental time. Root mean square (RMS) error is equal to 0.09.

4.3 PDS-P tests: particulate debris spreading in the pool

The goal of this work is to provide experimental data on spreading of solid particles in the pool by large scale two-phase flow currents induced by gas injection from the bottom of the pool. These data are necessary for development and validation of predictive capabilities of computer codes allowing numerical modeling of the debris bed formation at prototypic severe accident conditions. In this work the results from two series of PDS-P tests are provided. Both, center-pool symmetric and side-pool asymmetric air injection configurations are important for model validation. Note, that more comprehensive experimental and scaling study has been performed for side-pool air injection test series.

4.3.1 Preliminary series of test with center-symmetric air injection in the pool

Our experimental approach is to employ a specially designed test section allowing quantifying redistribution of the particles in the pool as function of two-phase turbulent flows created with help of gas injection from the bottom of the pool. The technique is quite similar to that used in studies on self-leveling and spreading of the particulate debris bed in PDS-C (closures) facilities reported in [21] and [5]. Note, that in this work a separate effect studies are performed such that effect of particulate bed self-leveling phenomenon (studied early [21], [5]) is minimized by purposely restricting the particle spreading at the pool bottom. The particle catchers are used for this purpose. The air injection is used in this work to simulate the decay heat-induced steam production at reactor scale. The methodology of scaling of the gas flow rates corresponding to steam production is described in [4]. The effects of water subcooling conditions are not covered in these studies although have been studied numerically in [72]. It is instructive to note that the main purpose of this experiment is to provide data for code validation and not to simulate reactor accident scenarios. It is practically impossible to satisfy simultaneously all important scaling criteria for such multiscale problems as particle spreading in a pool with two-phase flow induced by boiling inside a debris bed. The details on measurements technique, test conditions and measured parameters are provided below.

The PDS-P (particulate debris spreading in the pool) facility consists of following main parts: the particle delivery system, main water tank, the particle collection system, gas supply and flow rate measurement system.

The schematic illustration of the facility (a) and its photographic image are shown in Figure 39. The current design of the PDS-P experimental facility allows performing tests with following varied parameters (see Figure 39 for definition of some parameters):

- Working height $H_{pool}$of the water level in the pool: up to 0.8 m at highest flow or 1.1 m at lower flow rates;
- Working length of the pool L_{pool}: up to 1.3 m;
- Gas injection chamber with adjustable air flow rate Q_g:
    - with a perforated plate having 7x20 cm effective injection area consisting of nozzle matrix providing flow up to 35 L/s (202 m/s in the nozzle or 2.4 m/s superficial velocity for the effective injection area of 0.0144 m^2);
- Particle delivery flow rate ranging between 1 and 5 g/s.

The tank has a fixed width of 72 mm. This dimension is chosen in order to preserve close to 2D geometry for the turbulent currents and particles spreading, i.e. pool width is much less than length and height of the pool. On the other hand the pool width should be kept much larger than the characteristic particle size (3 mm vs 72 mm in reported tests here) in order to minimize influence of the particle-wall interaction.

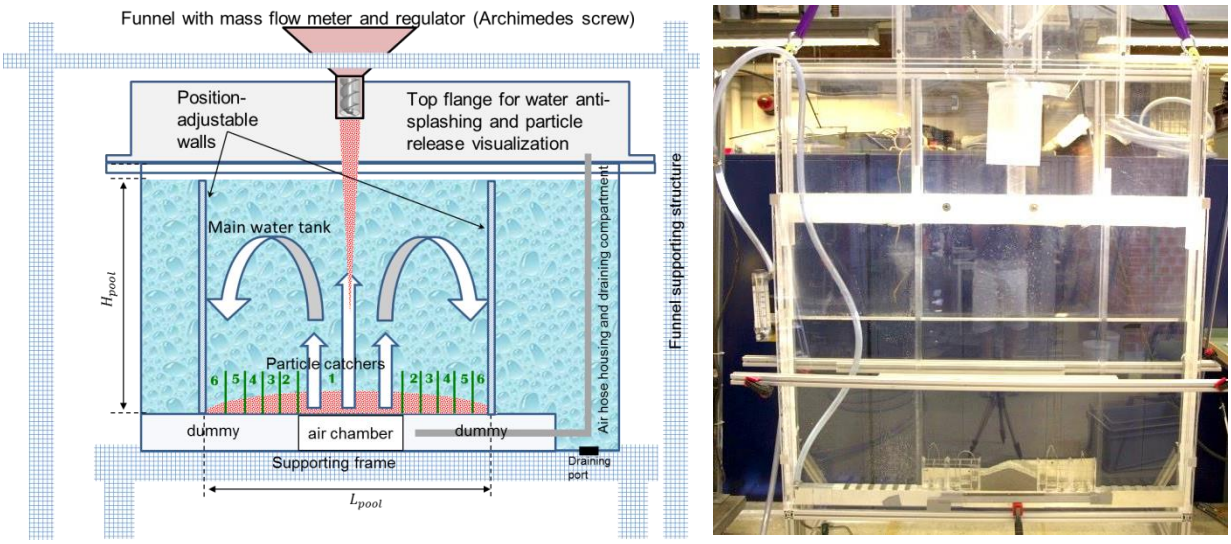

a) b)

Figure 39: PDS-P facility: schematics (a) and test section after experiment (b).

The water tank is made of acrylic (Plexiglas) transparent material having wall thickness of 20 mm. This provides obvious advantage for photographic and video shooting of the tests. Upon air injection into the system the walls of the tank suffers from vibrations and bulging. As a countermeasure to these unwanted effects a pair of strong horizontally aligned aluminum bars are installed as shown Figure 39(b).

The particle delivery system is designed in the form of a funnel having motorized screw inside 20 mm in diameter nozzle. The rotation rate of the screw is below 1 Hz providing low rate particle delivery. Due to technical limitations the particle flux is not controlled very well; however, it is low enough to minimize the particle-particle interaction at the water level and below. This is required for validation of the codes with disabled particle-particle interaction.

All 10 particle catchers are symmetrically positioned with respect to the funnel axis and air injector chamber (a separate catcher No. 1) as schematically shown in Figure 39(a). The positioning and catcher size along the pool length are given in Table 12. Note, there are 11 catchers in total. After each test the filled with particles catchers are extracted from the pool for particle mass measurements.

Table 12: Particle catchers positioning and size. See Figure 39(a) for catcher numbering.

Catcher No.	1 (air chamber)	2	3	4	5	6
Distance from pool center [mm]	0	153	200	250	297	340
Total catcher length [mm]	230	24	40	40	25	40

Tests without particles and assessments of the total void fraction in the pool

The first series of tests performed on PDS-P facility has been performed without particles. The purpose of these tests is to provide data which can be used for validation of the code simulating the two-phase flow in the pool. In particular, a total void fraction α in the pool as function of the gas flow rate Q_g and length of the pool has been quantified. The complete test matrix is shown in Table 13. As seen from the table the total void fraction is measured with acceptable accuracy of a few percent.

Table 13: Test conditions for the experiments performed without particles. The total void fraction $\boldsymbol{\alpha}$ and its uncertainty in the pool are provided.

Test#	pool length L_{pool} [m]	pool depth H_{pool} [m]	Pool area [m^2]	Gas flow rate Q_g [L/s]	Estimated water area above initial level [m^2]	Averaged pool void fraction (measured) α_{meas}	Pool void fraction (interpolated) α_{interp}
NOP01	0.681	0.500	0.341	9.4	0.116	0.25 ±0.027	0.27 ±0.018
NOP02	0.681	0.500	0.341	11.8	0.135	0.28 ±0.042	0.30 ±0.021
NOP03	0.681	0.500	0.341	14.2	0.167	0.33 ±0.003	0.33 ±0.003
NOP04	0.681	0.500	0.341	16.5	0.200	0.37 ±0.001	0.36 ±0.011
NOP05	0.681	0.500	0.341	18.9	0.238	0.41 ±0.021	0.38 ±0.025
NOP06	0.681	0.500	0.341	21.2	0.258	0.43 ±0.005	0.41 ±0.022
NOP07	0.681	0.500	0.341	4.7	0.069	0.17 ±0.011	0.19 ±0.025
NOP08	0.681	0.500	0.341	7.1	0.101	0.23 ±0.017	0.23 ±0.006
NOP09	0.681	0.500	0.341	2.4	0.061	0.15 ±0.022	0.13 ±0.016
NOP10	0.681	0.700	0.477	2.4	0.067	0.12 ±0.008	0.12 ±0.005
NOP11	0.681	0.700	0.477	4.7	0.097	0.17 ±0.006	0.17 ±0.005
NOP12	0.681	0.700	0.477	7.1	0.129	0.21 ±0.010	0.22 ±0.003
NOP13	0.681	0.700	0.477	9.4	0.154	0.24 ±0.006	0.25 ±0.009
NOP14	0.681	0.700	0.477	11.8	0.191	0.29 ±0.007	0.29 ±0.000
NOP15	0.681	0.700	0.477	14.2	0.223	0.32 ±0.016	0.32 ±0.002
NOP16	0.681	0.700	0.477	16.5	0.246	0.34 ±0.012	0.34 ±0.004
NOP17	0.681	0.700	0.477	18.9	0.280	0.37 ±0.019	0.37 ±0.000
NOP18	0.681	0.700	0.477	21.2	0.336	0.41 ±0.008	0.39 ±0.018

The procedure for assessments of the total void fraction in the pool is described as following. Each test has been recorded as a video clip or several photo snapshots. There were three image frames randomly selected and analyzed by image processing. The void fraction from each frame is calculated based on the excess of the area occupied by the two-phase mixture with respect to the original water level. The water surface shaping along the width of the pool is neglected in these 2D-restricted studies. If the water surface edge is a blurred then a middle curve is used to approximate the edge. The typical snapshots of the tests without and with particles are shown in Figure 40 and Figure 42 respectively. The experimental data have been interpolated and resulting $\alpha(Q_g)$ dependence together with analytical fit are shown in Figure 41. These analytical dependencies describe experimental data very well for both 0.5 and 0.7 m

depths of the pool. They are used in characterization of the particles spreading efficacy in the pool provided in the next section.

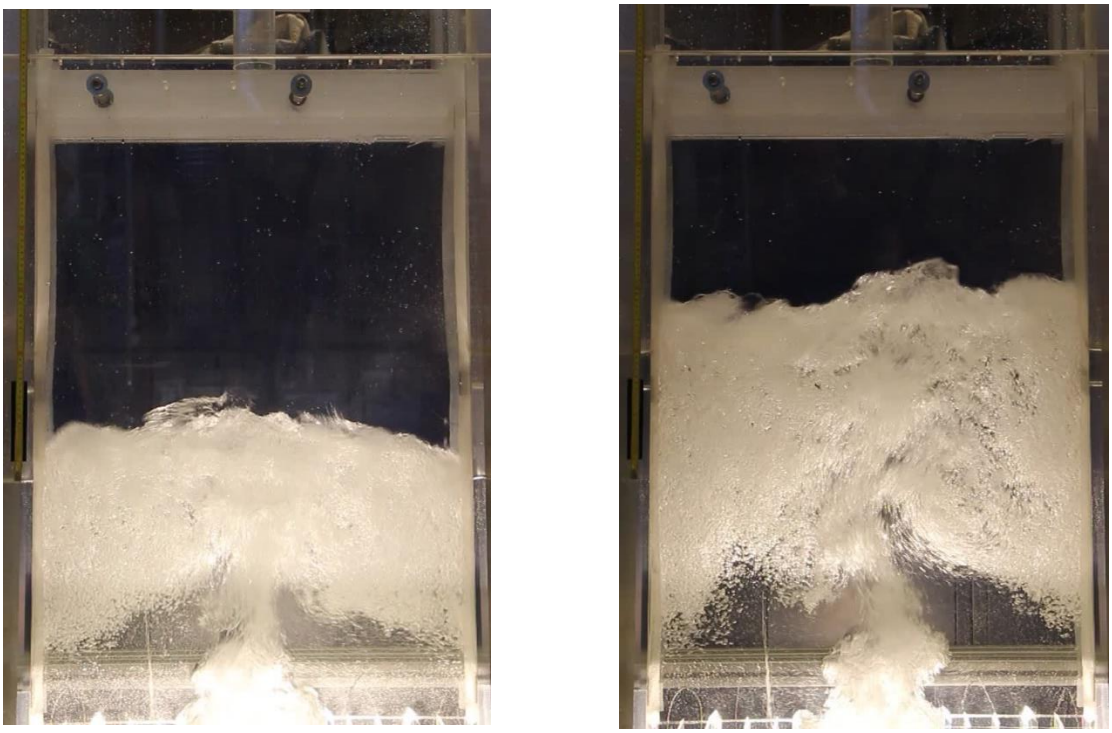

NOP09, 0.5 m NOP10, 0.7 m

Figure 40: Snapshots from PDS-P tests performed with equal lowest gas injection rate (2.36 L/s) and different pool depths depicted at the bottom of each image.

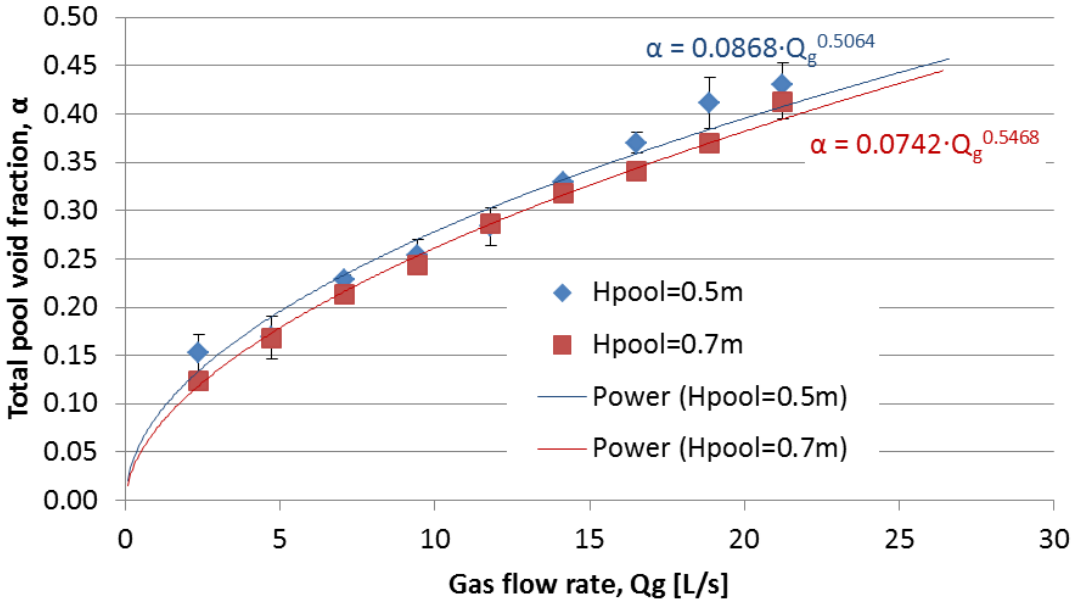

Figure 41: Total void fraction in the pool: measured (symbols) and power fit interpolated (solid curves) data from 0.5 and 0.7 m deep pool. The error bars represent experimental deviation from three measurements (image processing) as described in the text.

The total void fraction measured in these tests should not be confused with the local void fraction. Although it is quite challenging to measure the local void fraction by means of non-intrusive methods there are models which have been successfully validated and used for representation of the void fraction distribution in the pool. An example of such models and relevant experiments can be found in [25]. Despite an axisymmetric pool geometry used in [25] it is believed that an analytical transformation from the 3D axisymmetric to 2D void fraction distribution function is possible. Such transformation would allow assessments of the local void fraction across the water pool.

Tests with particles

Our first series of PDS-P tests with spherical stainless steel particles have been performed in the pool with present turbulent flows. The tests conditions are summarized in Table 14. Due to few failed tests the most of the tests were performed in the 0.7 m deep pool. After each test all particles have been collected from each catcher for accurate weight measurements. The weight of particular material collected from two symmetrically aligned catchers has been averaged out and value of the corresponding mass fraction is calculated.

Table 14: Test conditions for the experiments with stainless steel 3 mm spherical particles.

Test #	Particle size d_p [mm]	H_{pool} [m]	L_{pool} [m]	Particle fall height above water surf. H_{fall} [m]	Q_g [L/s]	Total mass [kg]	Particle pouring time [s]	Average particle mass flow Q_p [g/s]	Note
1	3	0.7	0.681	0.926	0.00	6.824	1480	4.61	
2	3	0.5	0.681	1.126	4.72	0.000	2305		Partly failed
3	3	0.7	0.681	0.926	4.72	6.949	1554	4.47	
4	3	0.5	0.681	1.126	7.08	6.221	2305	2.70	
5	3	0.7	0.681	0.926	7.08	5.516	1539	3.58	
6	3	0.5	0.681	1.126	9.44				Failed
7	3	0.7	0.681	0.926	9.44	5.021	4161	1.21	Not reliable
8	3	0.7	0.681	0.926	14.16	5.146	2778	1.85	
9	3	0.7	0.681	0.926	11.80	5.304	2125	2.50	
10	3	0.7	0.681	0.926	4.72	6.027	1748	3.45	
11	3	0.7	0.681	0.926	7.08	6.246	1836	3.40	

In Figure 42(a-b) the snapshots of the tests with particles performed with lowest (a) and highest (b) gas flow rate are given. Due to extremely low flow rate of the granular material a single particle is hardly distinguishable in the images. A typical image of the filled catchers after the test is illustrated in Figure 42(c).

a) test# 10

b) test# 8

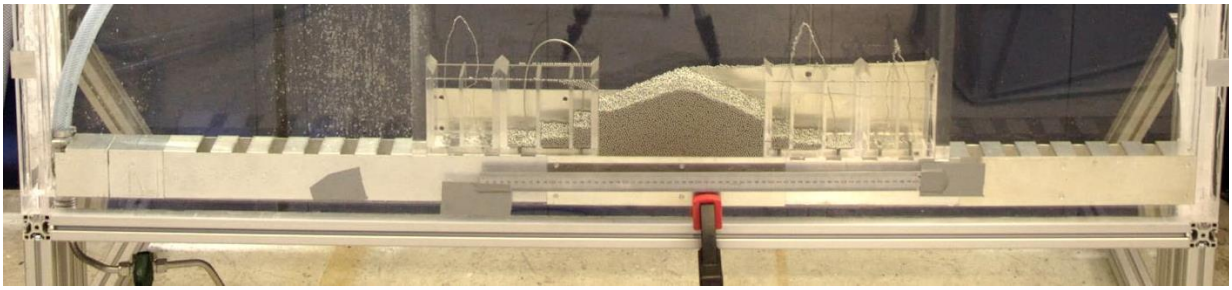

c)

Figure 42: Snapshots from two PDS-P tests: 4.7 L/s (a) and 14.2 L/s (b) air injection rates respectively. Note, images are taken with dissimilar exposure times. Filled catchers with particles after PDS-P experiment (c).

Analysis of the results: characterization of the particles spreading in the pool

In this section the characterization of the efficacy of turbulent flow driven particles spreading is discussed. The assessments on efficacy are necessary to identify most influential physical parameters and test conditions. This information will be used for planning of the separate effect-focused experimental studies as well as for development of the empirical models and experimentally obtained closures (similarly to [5]) which can be scaled up to the reactor SA conditions.

Obtained experimental results can be easily illustrated and compared by plotting of the mass fraction, density of the mass per unit area or average debris height as function of catcher

position (its dimensional or non-dimensional value). From these plots presented in Figure 43 it is seen how the injected air flow rate affects the particles redistribution across catchers. In the general way, the higher gas injection causes closer-to-uniform distribution of the granular material. However, at $Q_g > 7$ L/s a distinctive accumulation of the particles take place in most distant catchers from the center. At this point the two-phase currents are strong enough to relocate particles towards the periphery. The effect is very well pronounced in dimensionless units where relative height of the debris bed can be higher than one in the catchers close to center (Figure 43d).

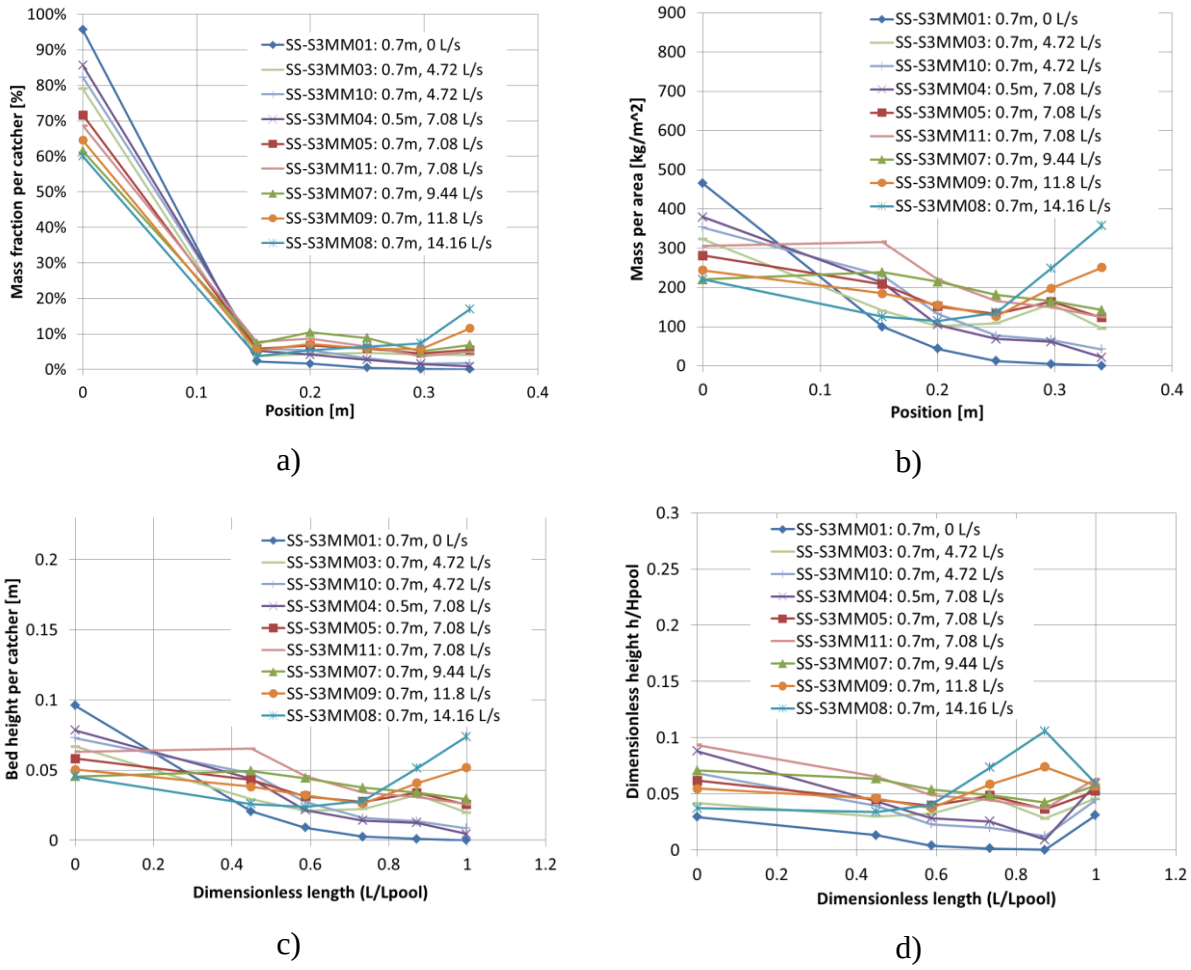

a) b)

c) d)

Figure 43: Tests results represented by dimensional and dimensionless parameters characterizing the debris bed at the bottom of the pool.

The efficacy of the particle spreading in the pool can be represented by an integral parameter S_{eff} computed for each PDS-P test and defined as:

$$S_{eff} = 1 - \frac{\sum_i |\bar{h} - h_i| \cdot \frac{A_i}{A_{tot}}}{\bar{h}}, \tag{4.18}$$

where summation is performed over all catchers, h_i is average debris bed height in i^{th} catcher, A_i is area of the catcher, A_{tot} is total spreading area and mass-averaged bed height across all catchers is:

$$\bar{h} = \sum_i h_i \cdot \frac{A_i}{A_{tot}}, \qquad h_i = \frac{m_i}{\rho_p \cdot (1-p) \cdot A_i} \tag{4.19}$$

where p is particulate bed porosity (typically around 0.38 for round particles) and ρ_p is density of the particles. Taking into account two last expressions we see that $\bar{h}$ is actually independent of the individual catcher area. Note, that enumerator in expression (4.18) is a modified mean of the debris bed deviation from mass-averaged debris bed height $\bar{h}$ given by (4.19). The (4.18) is chosen as an optimal characterization of the particle spreading efficacy in the pool for the main limiting cases:

- One catcher is significantly filled, others are empty: $S_{eff} \to 0$;
- One catcher is empty, others are filled such that $\bar{h} \approx h_i$: $S_{eff} \to 1$;
- Most efficient spreading when $\bar{h} = h_i$: $S_{eff} = 1$.

The S_{eff} parameter has been analysed as function of few non-dimensional measures characterizing the two-phase flow and forces acting on a single particle. Among these parameters the void fraction α, Reynolds Re and Froude Fr numbers as well as ratio of the drag F_d to the gravity F_g forces $P_1 = F_d/F_g$ acting on a single particle in the pool. The Fr number characterizes the momentum of the two-phase flow in the pool (Eq. (4.26) in page 87) whereas Re represent ration of the inertia to viscous forces (Eq. (4.23) in page 86). The parameter P_1 is plotted vs Re and Fr in Figure 44 for all 9 successfully performed tests. The details on how these parameters are defined and calculated can be found in "Supplementary material used in the analysis" subsection.

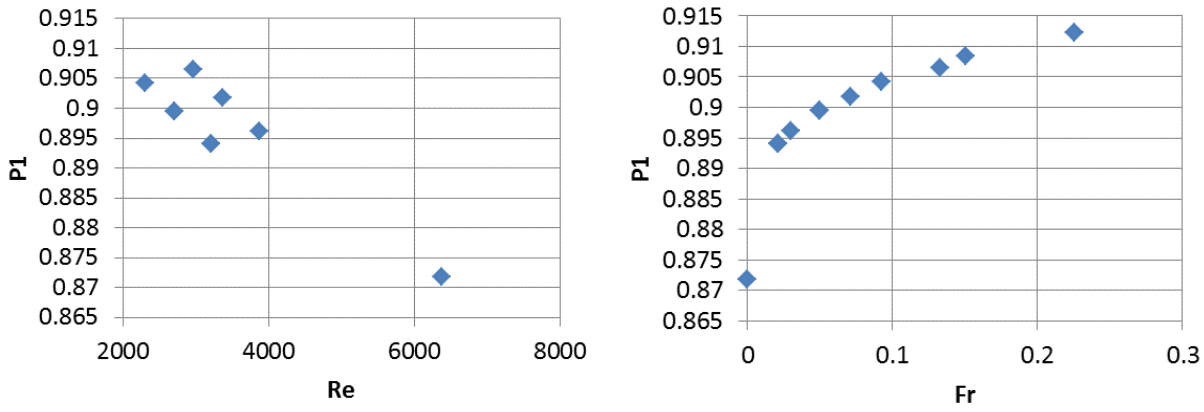

a) b)

Figure 44: $\boldsymbol{P_1}$ parameter as function of Reynolds and Froude numbers.

The resulting dependencies of the estimated S_{eff} as function of dimensionless paramters is presented in Figure 45. In addition a S_{eff} dependence on a mutual measure $P_1 \cdot Fr \cdot \left(2H_{pool}/L_{pool}\right)^2$ is plotted in Figure 45(d). Except for the $S_{eff}(Re)$ in Figure 45(c), the rest of the curves exhibit qualitatively similar behavior with a distinctive maximum. At this maximum, i. e. when gas flow rate reaches some critical value, the $S_{eff} = 90\%$ and the particles spreading is most efficient. After the maximum, the turbulent currents stream particles towards peripheral corners (most distant catchers) far from uniform spreading.

Comparing (a) , (b) and (d) in Figure 45, it is clear that $S_{eff}(\alpha)$ and $S_{eff}(P_1)$ are qualitiviely the same whereas $S_{eff}\left(P_1 \cdot Fr \cdot \left(2H_{pool}/L_{pool}\right)^2\right)$ is a smoother curve with seem to be asymptotic tail on its right side corresponding to higher gas injection rates. In fact, in the latter dependence most of the physical forces acting on the particle are represented: the drag, the buoyancy, the driving momentum provided by the gas injection and the force of gravity (see "Supplementary material used in the analysis" subsection for details). The $H_{pool}/(L_{pool}/2)$ factor is used to scale the experimental results performed at different pool depth and length. In order to evaluate such scaling a sufficient amount of tests have to be performed with varied pool dimensions. This is for the future studies.

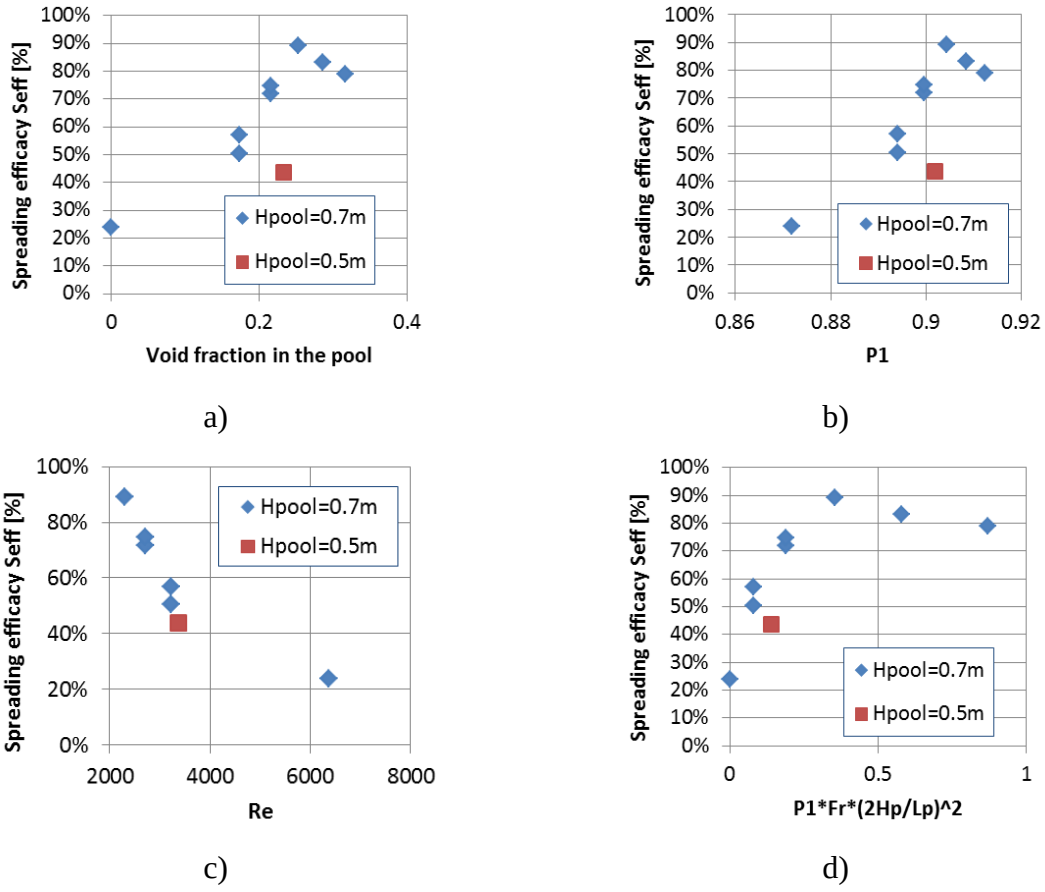

Figure 45: Particle spreading efficacy $\boldsymbol{S_{eff}}$ as function of various non-dimensional measures.

Supplementary material used in the analysis

To evaluate the drag of a particle in two-phase flow, it is more appropriate to calculate separately the drag due to interaction with water $F_{d,w}$, drag due to interaction with gas, $F_{d,g}$, after which calculate the average drag by weighting the two drags by the void fraction α:

$$F_d = (1-\alpha)F_{d,w} + \alpha F_{d,g} \tag{4.20}$$

However, the drag due to interaction with water $F_{d,w}$ is much higher than drag due to interaction with gas $F_{d,g}$ (especially if the gas exists as bubbles), therefore assume that:

$$F_d \cong (1-\alpha)F_{d,w} = (1-\alpha)\frac{1}{2}C_d\rho_c\frac{\pi d_p^2}{4}U_t^2, \tag{4.21}$$

where U_t is terminal velocity of particle in liquid, ρ_c is coolant density and d_p is particle diameter. For the drag coefficient C_d we can write:

$$C_d = \frac{24}{Re} + \frac{4}{\sqrt{Re}} + 0.4, \tag{4.22}$$

with Reynolds number for the particles with velocity relative to liquid defined as:

$$Re = \frac{d_p \cdot \rho_c \cdot U_{r,w}}{\mu_c}, \tag{4.23}$$

with μ_c is liquid dynamic viscosity. The velocity of the particles with respect to liquid in (4.23) is estimated as difference between particle entrance velocity $U_{p,e}$ and coolant velocity U_c:

$$U_{r,w} = U_{p,e} - U_c, \;\; U_c = \sqrt{2g\left(H_{c,max} - H_{pool}\right)}, \tag{4.24}$$

where H_{pool} is depth of the pool and experimentally observed maximum water level $H_{c,max}$ is plotted and analytically represented as in Figure 46.

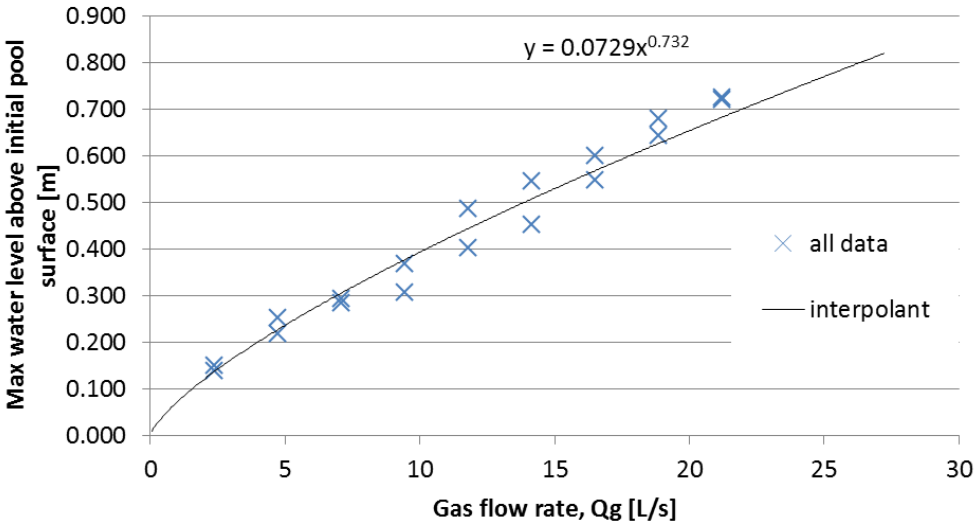

Figure 46: Experimentally observed maximum level $H_{c,max}$ reached by water surface upon gas injection in the pool.

For the terminal velocity of the particle U_t (in Stokes regime and high Re) used in (4.21) it can be shown that:

$$U_t = \sqrt{\frac{4}{3C_d}\frac{\rho_p - \acute{\rho}_c}{\acute{\rho}_c} g d_p}, \tag{4.25}$$

where modified density of the coolant is $\acute{\rho}_c = (1-\alpha)\rho_c$ and particle density $\rho_p = 7800\ \mathrm{kg/m^3}$.

The momentum of the two-phase flow in the pool created by the injection of the gas and buoyancy due to presence of void in the flow is characterized by the Froude number, defined as the ratio of the characteristic velocities:

$$Fr = \left(\frac{U_{g,sf}}{U_b}\right)^2 \tag{4.26}$$

where $U_{g,sf}$ is the gas superficial velocity determined from the volumetric flux, and U_b is the characteristic buoyancy-related velocity:

$$U_{g,sf} = \frac{Q_g}{\text{total injection area}}, \qquad U_b = \sqrt{\acute{g} H_{pool}(1-\alpha)} \tag{4.27}$$

In addition to test matrix (Table 14) the above estimated dimensional and non-dimensional parameters (4.20)-(4.27) are provided in Table 15.

Table 15: Estimated dimensional and non-dimensional parameters per each test with experiments on turbulent flow driven particle spreading in the pool.

Test #	H_{pool} [m]	Particle fall height above water surf. [m]	$U_{p,e}$ [m/s]	U_t [m/s]	Re	C_d	Q_g [L/s]	U_c [m/s]	$U_{g,sf}$ [m/s]	Drag force F_d [N]	P1	Fr
1	0.7	0.926	4.3	0.767	6379	0.454	0	0.000	0.000	9.4E-04	0.87	0.000
2	0.5	1.126	4.7	0.849	3875	0.470	4.72	2.110	0.328	9.7E-04	0.90	0.030
3	0.7	0.926	4.3	0.832	3220	0.478	4.72	2.110	0.328	9.7E-04	0.89	0.021
4	0.5	1.126	4.7	0.870	3370	0.476	7.08	2.448	0.492	9.8E-04	0.90	0.071
5	0.7	0.926	4.3	0.850	2714	0.486	7.08	2.448	0.492	9.7E-04	0.90	0.050
6	0.5	1.126	4.7	0.888	2963	0.482	9.44	2.720	0.656	9.8E-04	0.91	0.133
7	0.7	0.926	4.3	0.866	2307	0.494	9.44	2.720	0.656	9.8E-04	0.90	0.093
8	0.7	0.926	4.3	0.892	1656	0.513	14.16	3.155	0.983	9.9E-04	0.91	0.226
9	0.7	0.926	4.3	0.880	1961	0.503	11.8	2.951	0.819	9.8E-04	0.91	0.151
10	0.7	0.926	4.3	0.832	3220	0.478	4.72	2.110	0.328	9.7E-04	0.89	0.021
11	0.7	0.926	4.3	0.850	2714	0.486	7.08	2.448	0.492	9.7E-04	0.90	0.050

4.3.2 Tests with pool-side air injection

In this work, we report 34 two-phase flow tests performed without particles, and 63 tests performed with particles delivered at a low rate In our previous work, the gas injector was positioned symmetrically between the pool walls [22]. In this work, given that the number of tests was limited and the number of other free parameters was significant, it was decided to place the gas injection near one of the side walls. This resulted in a more stable (not subject to meandering and splashing) bubble plume than in the case of central injection, which is advantageous in view of providing numerical code validation data. Also, the plane pool with side injection can be considered as “one half” of a pool with enforced symmetric conditions. Conditions of all tests are provided in Table I, Table II and Table III respectively of APPENDIX A in [23].

The main goal of PDS-P work is to provide data for code validation. Therefore, selection of experimental parameters is based not only on consideration of severe accident (SA) conditions, but on the merits of experimental data for validation of different models. The

general aim of the tests is to cover possible ranges of different regimes and parameters in order to provide data for understanding of importance of separate effects.

In the experiments, we quantify the distribution of particles along the pool bottom as a function of gas injection parameters. The technique is similar to that used in the studies on self-leveling and spreading of the particulate debris bed in PDS-C facilities reported in [21] and [5]. A detailed description of the measurement techniques is reported in [22]. The test conditions and measured parameters for the new series of the tests are given below.

The PDS-P facility consists of the following main parts: the particle delivery system, main water tank, the particle collection system, gas supply and flow rate measurement system [22]. The general view of the facility is illustrated in Figure 47(a). A snapshot of facility operation is given in Figure 47(b). The tests reported herein were performed with the following variable and fixed parameters (see Figure 47 for definition of some parameters): the depth of water pool, H_{pool}, was either: 0.5, 0.7, or 0.9 m; the pool length, L_{pool}, was either: ~0.5; ~0.9[1] or 1.5 m; the tank width was fixed to 72 mm. These dimensions were chosen in order to preserve close to 2D geometry for the turbulent currents and particles spreading, i.e. the pool width was much smaller than the length and height of the pool. On the other hand, the pool width was much larger than the characteristic particle size in order to minimize the influence of particle-wall interaction. The water tank is made of 20 mm thick acrylic material. Several pairs of rigid bars are installed (as shown in Figure 47) to minimize vibrations and bulging of the tank walls during air injection. The water temperature was kept within 15-18°C.

The gas injection chamber was a rectangular box with the height 60mm, length 200mm, and width 70mm. The air injecting holes in perforated top plate were 1mm in diameter, the pitch size of the holes was 10mm in both directions. The air mass flow rate, Q_g, is adjustable and provides uniform gas injection within the range of 2.2-14.5 g/s. The top limit of the range was selected in order to be able to achieve fluidization of settled debris bed at the highest values of Q_g.

Particles were delivered from the top boundary of the facility at the fixed height of 1.61m above the top of the particle catchers through a funnel equipped with Archimedes screw as

[1] The exact value of 0.894 m is rounded in the legends of the plots to 0.89 m or 0.9 m for the sake of brevity.

shown in Figure 47(a) and schematically in Figure 56. The particle delivery rate was varied in the range between 1 and 5 g/s in order to minimize particle-particle interactions and the effect of the particles on the flow field. Few tests were performed in the same pool flow conditions, but with the particle delivery rate increased ten times. The ultimate particle spreading patterns obtained in all tests were similar, suggesting that there were no "collective" effects due to particle-particle and particle-flow interactions. The following particles were used in the experiments:

- Stainless steel spheres 3 mm in diameter (SSs_S3) with density $\rho_{p,SS3} \cong 7.8\ \mathrm{g/cm^3}$;
- Glass spheres 3 mm in diameter (GLs_S3) with density $\rho_{p,GL3} \cong 2.6\ \mathrm{g/cm^3}$;
- Stainless steel spheres 1.5 mm in diameter (SSs_S1.5) with density $\rho_{p,SS1.5} \cong 7.8\ \mathrm{g/cm^3}$.

Particles reaching the pool bottom were collected by several catchers. The catchers were designed to be accessible from the outside of the tank. A single catcher consists of i) catcher wall separator, ii) small funnel (Figure 47b), iii) quick coupler (black components attached to the tank bottom in Figure 47a), and iv) 50 mm diameter hose in which the particles are accumulated. The longest hoses (0.5 m) were positioned near the gas injection chamber where the largest mass fraction of the particle material was expected. The distance between the catcher walls was 10 cm. The first catcher (Figure 47a) also collected particles which fell on the gas injection plate and, thus, it has the effective length of 30 cm.

Note that the main goal of the work is to provide data for code validation, therefore, selection of particle size and density was based not only on consideration of possible values in prototypic severe accident (SA) conditions, but on the merits of experimental data for validation of different models and for understanding of the effects of separate parameters. For instance, particle parameters were chosen to provide non-trivial particle spreading patterns, given the geometry of the facility and gas flowrates, and to provide data necessary to clarify the effects of particle size and density. For particles of 1.5mm and 3mm diameters (also expected as a mean sizes of the particles resulting from corium fragmentation in water), it was found that particle-flow interaction is sufficiently strong, so that significant particle spreading occurs, but, on the other hand, such particles are not suspended in the flow (as would be the case for sub-mm particles). The particle supply rates were maintained low in order to decrease the effect of particle-particle and particle-flow interactions in order to produce data for separate effect code validation.

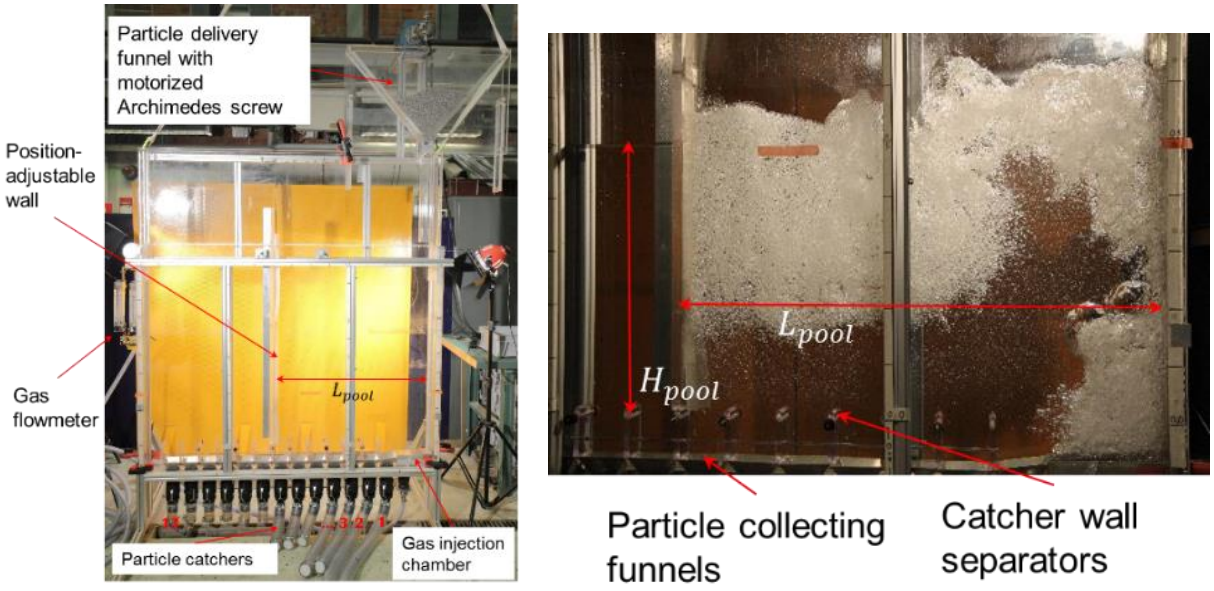

a) b)

Figure 47: PDS-P facility: general view (a) and test section in operation (b). The pool depth H_{pool} (b) is measured from the upper tip of the walls separating particles catchers.

Tests without particles

The comparison of the tests performed without particles and with gas injection in the center and near the side wall is shown in Figure 19. We followed image processing technique developed in [22] to determine the total void fraction α as an average from five snapshot images of the pool. Namely, each test has been recorded as a video clip. Video frames are randomly selected and analyzed by image processing. The void fraction from each frame is calculated based on the excess of the area occupied by the two-phase mixture with respect to the original water level. If the water surface edge is blurred then a middle curve is used to approximate the edge. Resulting data is shown in Figure 19. Note that relatively large error bars in Figure 19 can be attributed to the oscillations of the instantaneous void fraction in time. It is instructive to note that air injection near the side wall resulted in a more stable at macroscopic level (less subject to meandering and splashing) bubble plume than in the case of central injection, which is advantageous in view of providing numerical code validation data.

We found that the total void fraction in the pool is different for the tests where ratio H_{pool}/L_{pool} (ranging from 0.31 to 1.81, see Table II in [23]) is the same but the H_{pool} and L_{pool} values are different, e.g. $H_{pool}/L_{pool} = 0.5/0.497 \approx 0.9/0.894 \approx 1.01$. Therefore, we

approximate the total void fraction by the following formula where both dimensions of the pool are considered as separate variables:

$$\alpha = a \cdot L_{pool}^{b} \cdot H_{pool}^{c} \cdot Q_g^{d}, \tag{28}$$

$$a = 0.052, b = -0.818, c = -0.197, d = 0.474,$$

where $a \ldots d$ are fit constants, Q_g is expressed in g/s and pool dimension are in meters. The coefficient a has dimensionality of $\mathrm{m}^{-(b+c)} \cdot (\mathrm{g/s})^{-d}$. The quality of this fit is illustrated in Figure 20. As can be seen, the maximum deviation from the experimental values is below 10% of measured void fraction. The gas mass flow rate exponent d is comparable to the value of 0.5 determined previously [39] for the symmetric pool-centered gas injection.

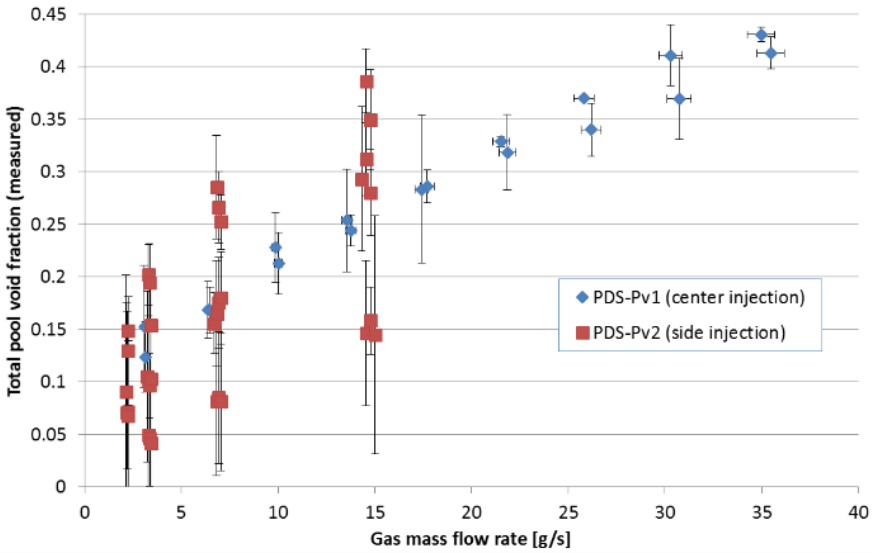

Figure 19: Measured total void fraction in the pool for tests without particles (two-phase flow). The measurement error of the gas flow rate does not exceeds 2%.

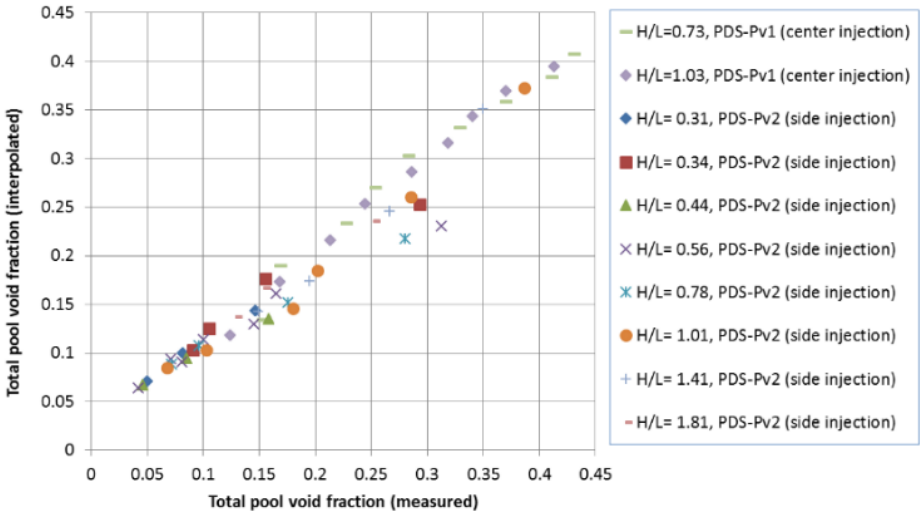

Figure 20: Approximate dependency for average void fraction Eq. (4.20) versus experimentally measured values. H/L is the ratio of the pool depth to its length H_{pool}/L_{pool}.

The estimated total void fraction α is an integral quantity characterizing the turbulent two-phase flow in the pool. Another characteristics which can be easily estimated is an effective void fraction α_{eff}. It is defined as the average void fraction within the active pool zone where two-phase flow (bubbles) is visually observed. Typically it is the upper half and right side (above the injection plate) of the pool as shown in Figure 47(b). The same image processing procedure (as for the determination of the total void fraction) has been applied to estimate the area of the active zone. The comparison of the α_{eff} versus experimentally measured values of α is shown for all side-injection experiments in Figure 21. As is seen from the graph, the effective void fraction can be about10% higher than the total one in the pool. The highest values are observed for the lowest pool aspect ratio H_{pool}/L_{pool}. On the other hand, high gas flow rate causes $\alpha_{eff} \rightarrow \alpha$ i.e. void is present almost everywhere in the pool.

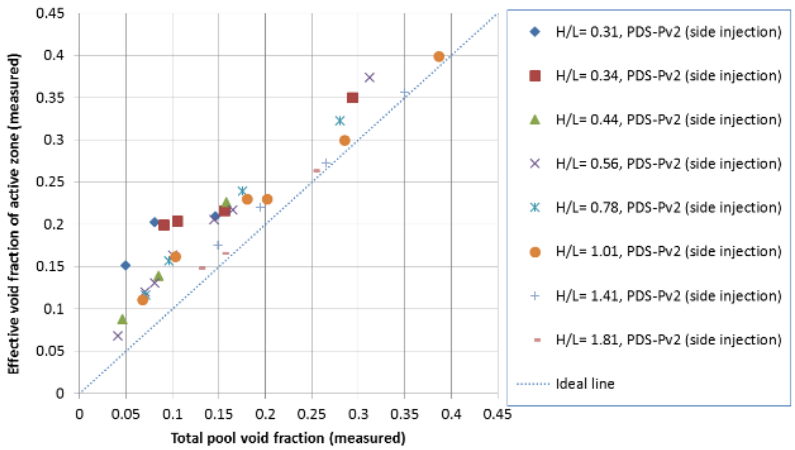

Figure 21: Comparison of the measured total versus effective void fractions in the pool.

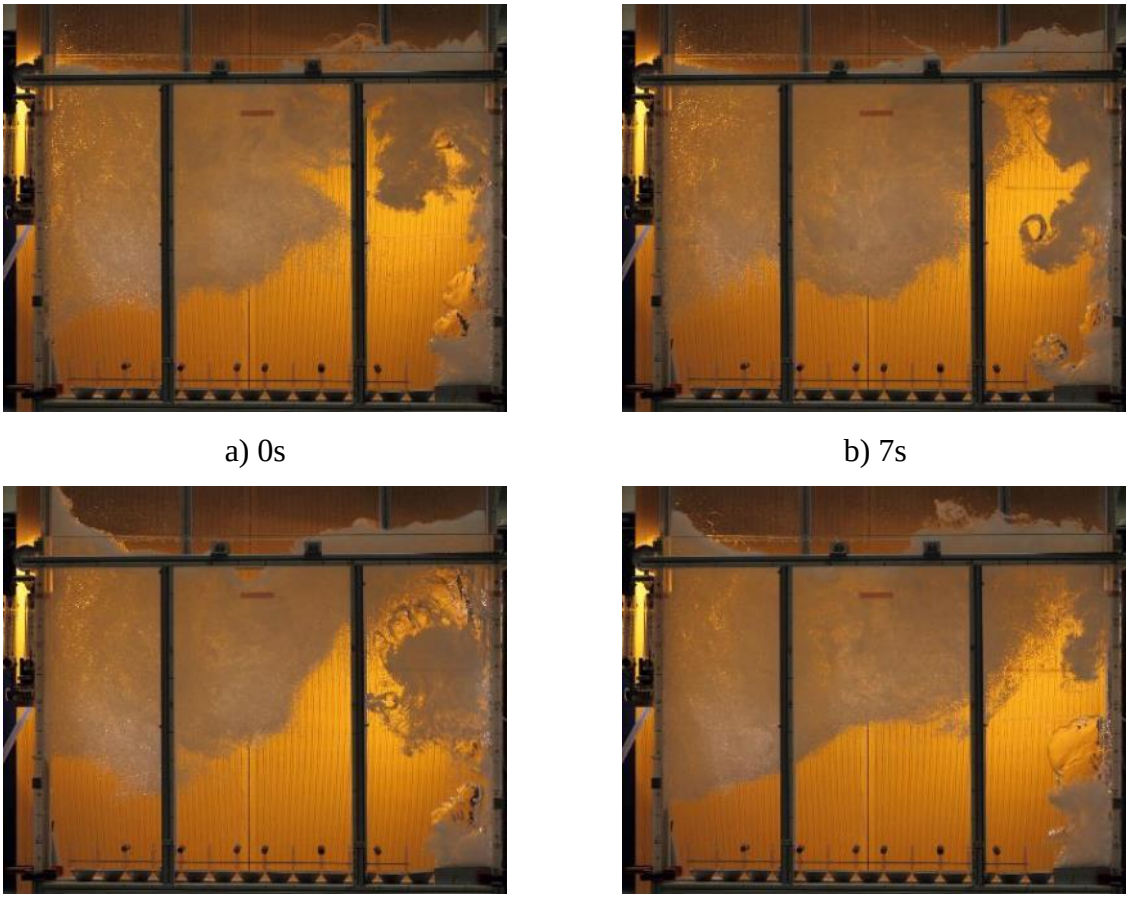

a) 0s b) 7s

c) 14s d) 22s

Figure 22: Snapshots of the test NOPs-28 with highest air flow rate of 15 g/s, $H_{pool} = 0.9$ m pool depth and $L_{pool} = 1.6$ m pool length. The relative to the first image (a) time offset in seconds for each snapshot is indicated below each figure.

Another remarkable feature of the flow is that at low gas injection rate a quasi-steady flow pattern and void distribution is observed whereas at high injection rates the pattern can change dynamically producing a quasi-periodic large scale void structures as shown in Figure 22. Large waves created by the large void structures disturb the water surface, and the flow in the pool experience erratic oscillations. Large regions with high void fraction above the injection chamber (Figure 22d) and regions with low void fraction can be formed for short periods of time. Such behavior is difficult to quantify in the experiment.

Tests with particles

In this work, we consider the effects (Figure 23 through Figure 25) of (i) gas injection flow rate, (ii) particle diameter: 3 or 1.5 mm; (iii) particle density: glass or stainless steel; on particle spreading. Conditions of the tests were changed one parameter at a time in order to

analyze separate effects. The legend of the tests includes particle material ("NOP" – no particles; "SS" – stainless steel; "GL" – glass), location of the gas injection ("c" – injection in the center; "s" – gas injection at the side), particle shape and size (e.g. "SSs_S3" – stainless steel sphere 3 mm in diameter, side injection), test number, height and length of the pool and gas injection flow rate. On the horizontal axis the particle catcher position r_i is normalized to the total length of the pool as r_i/L_{pool}. The non-dimensional mass fraction per catcher area on the vertical axis is defined as:

$$\tilde{m}_i = \left(\frac{m_i}{M_{tot}}\right) / \left(\frac{A_i}{A_{tot}}\right), \text{ where } M_{tot} = \sum_i m_i\,,\ A_{tot} = \sum_i A_i, \tag{29}$$

where the i^{th} catcher has the area A_i, the particle mass is m_i. As is seen from the figures, small 1.5 mm (Figure 25) or light glass (Figure 53) particles are spread more effectively to farther locations than the largest 3 mm stainless steel particles (Figure 23).

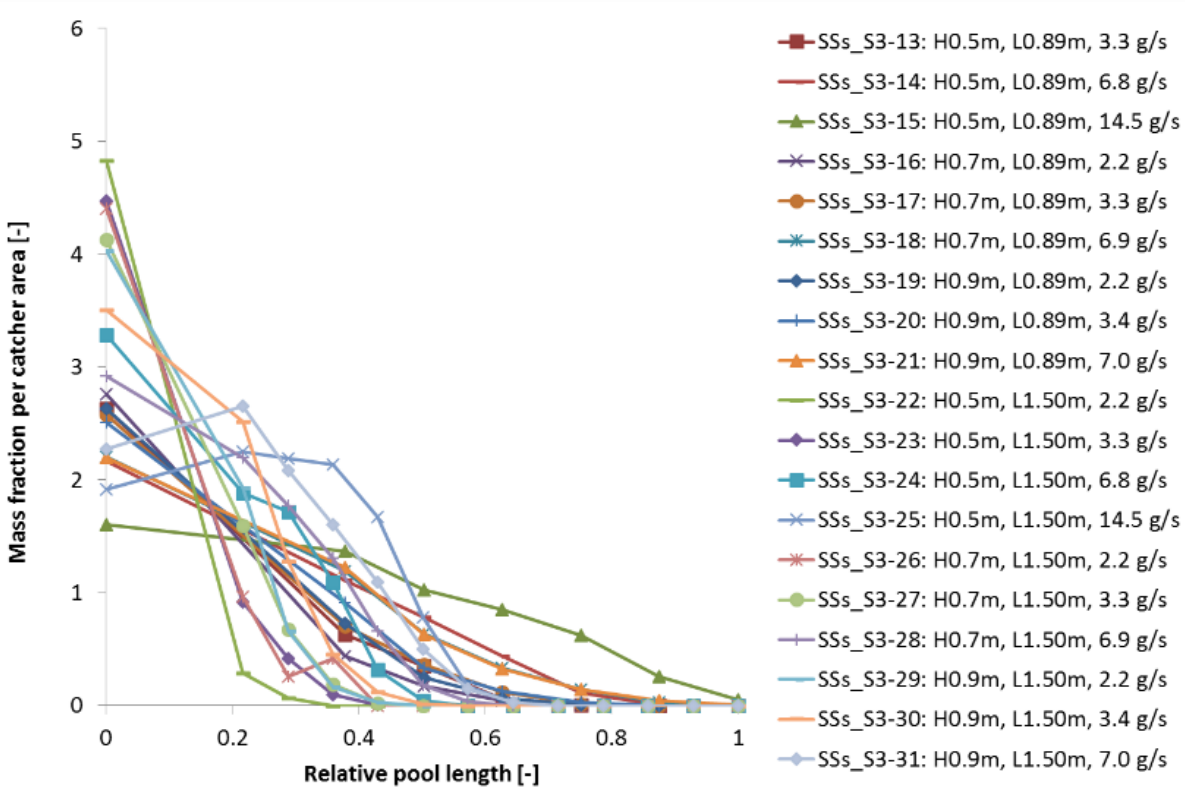

Figure 23: Spatial distribution of normalized particle mass fraction: 3 mm stainless steel particles.

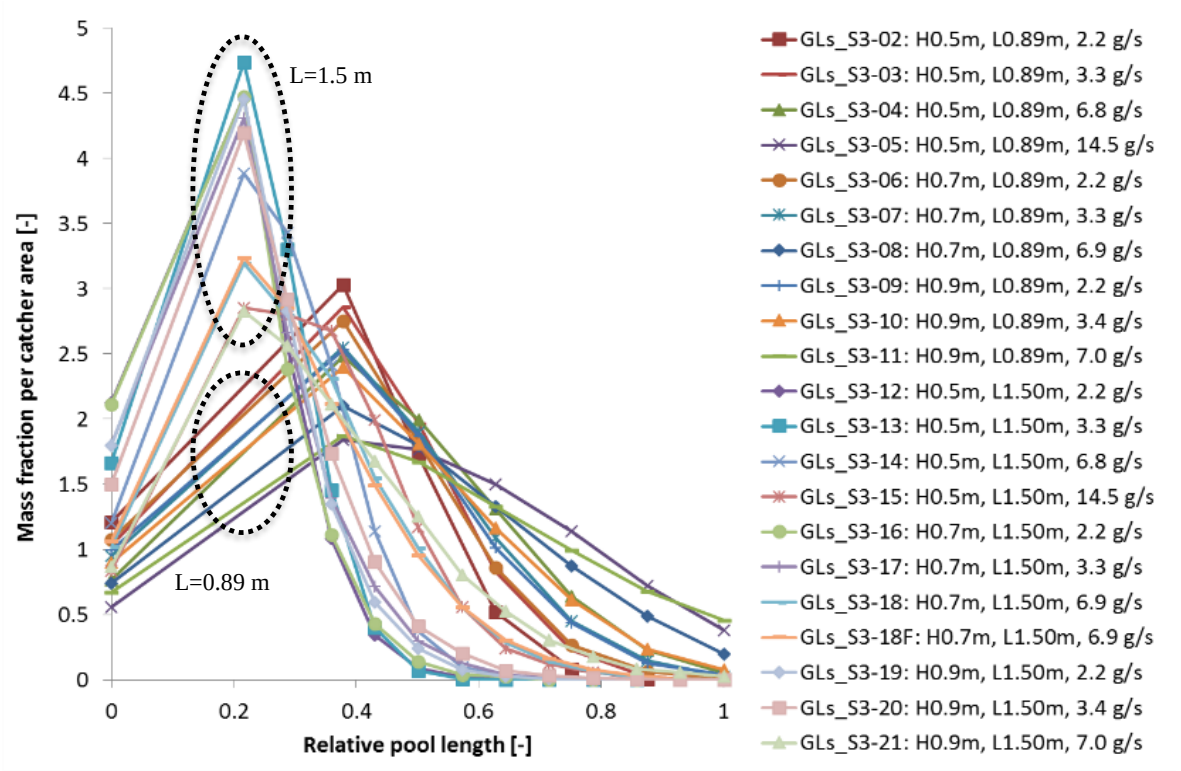

Figure 53: Spatial distribution of normalized particle mass fraction: 3 mm glass particles.

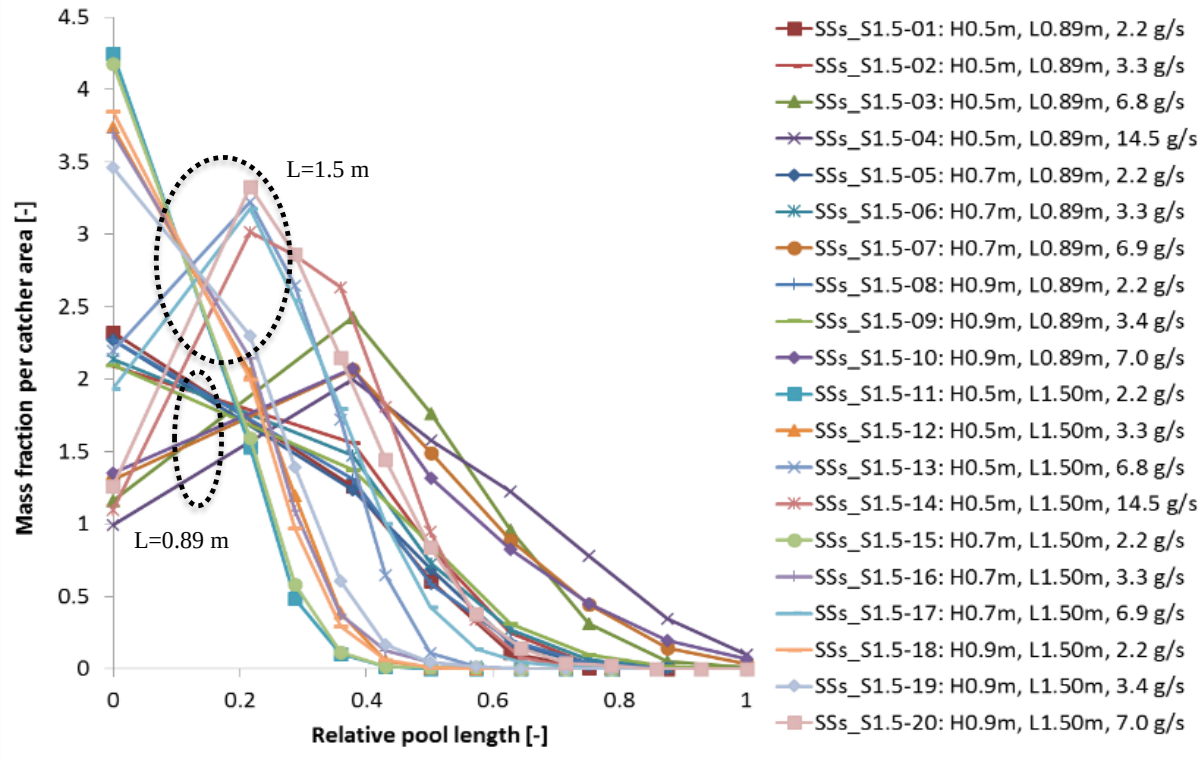

Figure 25: Spatial distribution of normalized particle mass fraction: 1.5 mm stainless steel particles.

Figure 55 illustrates the influence of the gas flow rate for fixed dimensions of the pool and particles of different diameters and materials. It is clear that lighter and smaller particles are spread more efficiently. However, at higher flow rates, the difference between the shapes of the beds becomes less significant (Figure 55c).

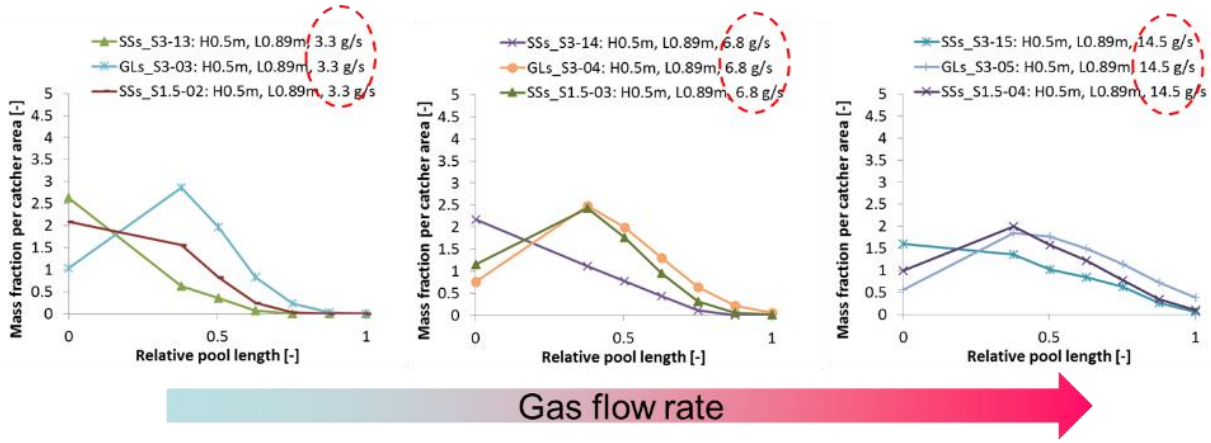

a) b) c)

Figure 55: Spatial distribution of normalized particle mass fraction obtained at different gas flow rates.

Semi empirical scaling approach for PDS-P

In order to characterize effectiveness of particle spreading we introduce the tangent of characteristic spreading angle $\tan\phi$ (see Figure 56)

$$\tan\phi = \frac{R_c}{H_{pool}} \tag{30}$$

where R_c is an average spreading distance defined as the distance from the axis of the particle source (funnel) to the center of mass of the debris collected in all catchers:

$$R_c = \frac{\sum_i m_i \cdot r_i}{\sum_i m_i}. \tag{31}$$

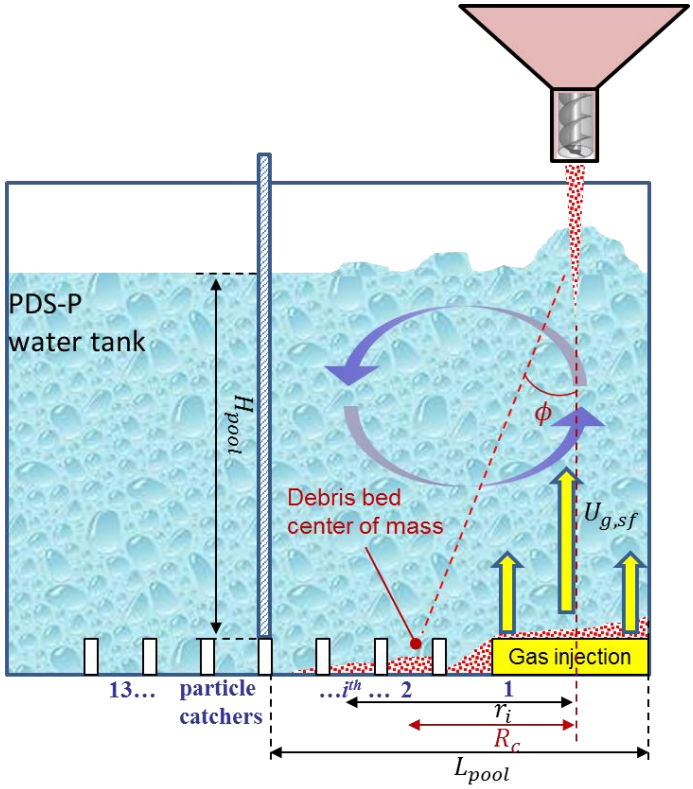

Figure 56: Schematics of the particle spreading in the PDS-P pool and definition of characteristic spreading angle $\phi = \tan^{-1}\frac{R_c}{H_{pool}}$.

In Figure 57, tests with the 3 mm in diameter glass and stainless steel particles are compared to show the effect of particle material density. The effect of particle size is illustrated in Figure 58. At low gas flow rates (few points lying near the diagonal at $\tan\phi \cong 0.21..0.25$ in Figure 58) the effect of changing particle size from 1.5 to 3 mm becomes small. This can be explained by the fact that at low gas flow rate gravity force has dominant effect on spreading. At high gas flow rates (upper right part of the plots in Figure 57 and Figure 58) all experimental points start to gravitate toward the diagonal again, indicating diminishing effects of the size and density on the mass averaged spreading distance (see also Figure 55). This can be considered as an indication of the increasing dominance of large scale two-phase circulation flow structure and geometrical configuration of the facility. Comparing Figure 57 and Figure 58 one can conclude that particle density has stronger influence on particle spreading than particle size for the selected ranges of sizes and densities. The complete tests matrix with main test conditions and resulting R_c are given in Table III of the APPENDIX A in [23].

In order to describe spreading of non-interacting particles by large scale turbulent two-phase flows in the pool, we propose a semi-empirical scaling approach. Consider a particle of diameter d_p falling in the water pool of depth H_p. The terminal velocity of falling particle U_t is evaluated from the balance of gravity and drag forces:

$$U_t = \sqrt{\frac{4}{3C_d}\frac{\rho_p - \acute{\rho}_c}{\acute{\rho}_c} g d_p}, \tag{32}$$

where ρ_p is particle density, $\acute{\rho}_c$ is modified coolant density $\acute{\rho}_c = (1-\alpha)\rho_c + \alpha\rho_g \approx (1-\alpha)\rho_c$ and the drag coefficient C_d is a function of particle Reynolds number Re_p. The void fraction α is determined from the analysis of the tests without particles depending on pool dimensions and gas flow rate (4.20). For high particle Reynolds numbers it can be assumed that $C_d \approx 0.45$ (e.g. see Eq. (2.69) in [24] for $Re_p > 1000$ in the limit of small volume fractions of solid phase). The Reynolds number based on the terminal velocity in single phase water was estimated in the range from 830 to 2300 for the tests conditions. The particle-water interaction time in the pool is then proportional to $t_{int} \propto H_p/U_t$. For a plane pool, the characteristic flow circulation time t_{circ} can be estimated as the ratio of the flow path (perimeter) to gas superficial velocity $U_{g,sf}$:

$$t_{circ} \propto \frac{2\left(L_p + H_p\right)}{U_{g,sf}} = \frac{H_p}{U_{g,sf}}\left(1 + \frac{L_p}{H_p}\right). \tag{33}$$

On the other hand, the characteristic horizontal velocity of the flow is

$$v_{hor} \propto \frac{L_p}{t_{circ}}. \tag{34}$$

It can be assumed that the average horizontal distance R_{spr} by which a falling particle will be transported by the circulation flow is proportional to:

$$R_{spr} \propto v_{hor} \cdot t_{int} \propto U_{g,sf} \cdot \frac{L_p}{L_p + H_p} \cdot \frac{H_p}{U_t} = \left(\frac{U_{g,sf}}{U_t}\right) \cdot \frac{L_p H_p}{L_p + H_p} \tag{35}$$

or, the average tangent of the “spreading cone” angle ϕ (see Figure 56) is:

$$\tan\phi = \frac{R_{spr}}{H_p} \propto \frac{U_{g,sf}}{U_t} \cdot \frac{L_p}{L_p + H_p} = \left(\frac{U_{g,sf}}{U_t}\right) \cdot \frac{1}{1+\chi}\ , \tag{36}$$

where $\chi = H_p/L_p$ is the ratio of the pool dimensions. We use the following regression formula

$$\tan\phi = F\left(\frac{U_{g,sf}}{U_t}\right) \cdot G\left(\frac{1}{1+\chi}\right), \tag{37}$$

where, for the sake of simplicity, we choose both unknown functions $F()$ and $G()$ to follow the power law with proportionality constant c_1 and exponents c_2, c_3:

$$\tan\phi = c_1 \cdot \left(\frac{U_{g,sf}}{U_t}\right)^{c_2} \cdot \left(\frac{1}{1+\chi}\right)^{c_3}. \tag{38}$$

To validate the approach given by Eq. (38), we analyzed the experimental data and assumed that the center of mass of the debris bed (31) can be used as the average lateral particle spreading distance (35), i.e. $R_{spr} = R_c$. By performing the regression analysis, we determined the unknown fit coefficients used in (38):

$$c_1 = 1.0000,\ c_2 = 0.4814,\ c_3 = 0.8537. \tag{39}$$

Remarkably, the exponent c_2 of the velocities ratio is close to the exponent of the gas flow rate in the empirical expression for the total void fraction of the pool (4.20), both values being very close to 0.5. The scaling expression (38) with the determined fit coefficients (39) is tested for prediction of the effects of particle density and size (see Figure 57 and Figure 58 solid and dashed lines). It is in reasonable agreement with the available experimental data, though for larger values of $\tan\phi > 0.8$ (i.e. high gas flowrates in a pool having the depth relatively small with respect to the spreading distance) further experiments are necessary to evaluate the scaling formula performance.

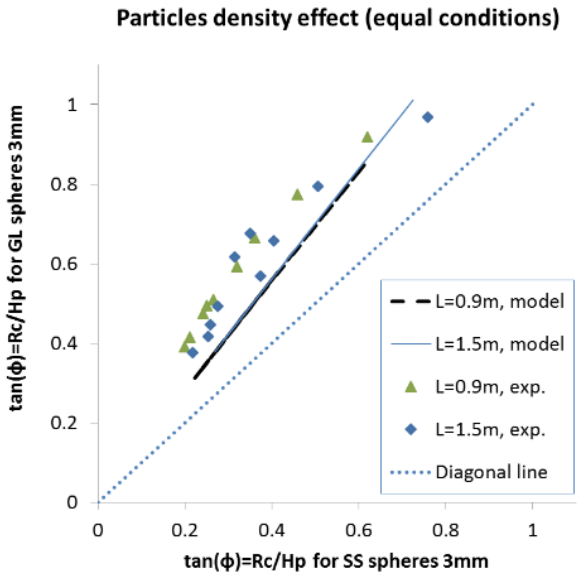

Figure 57: Particle density effect: comparison of the average spreading angle of the corresponding experiments (symbols) performed at equal test conditions except for the density of the particles (glass versus stainless steel). The modelling data (lines) are also provided for comparison.

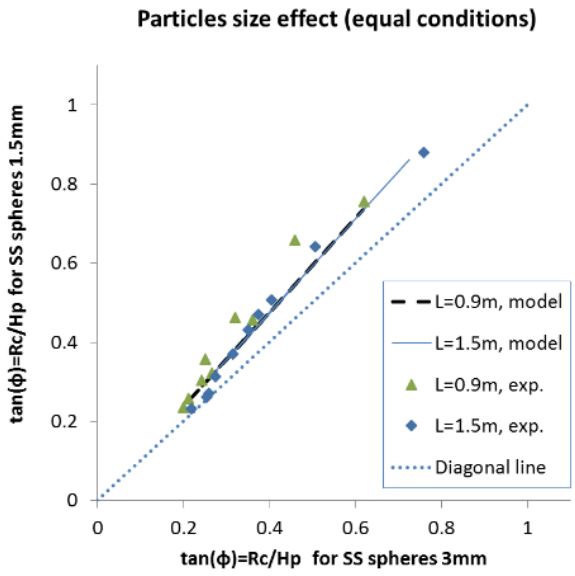

Figure 58: Particle size effect: comparison of the average spreading angle of the corresponding experiments (symbols) performed at equal test conditions except for the size of the particles (1.5 mm versus 3 mm). The modelling data (lines) are also provided for comparison.

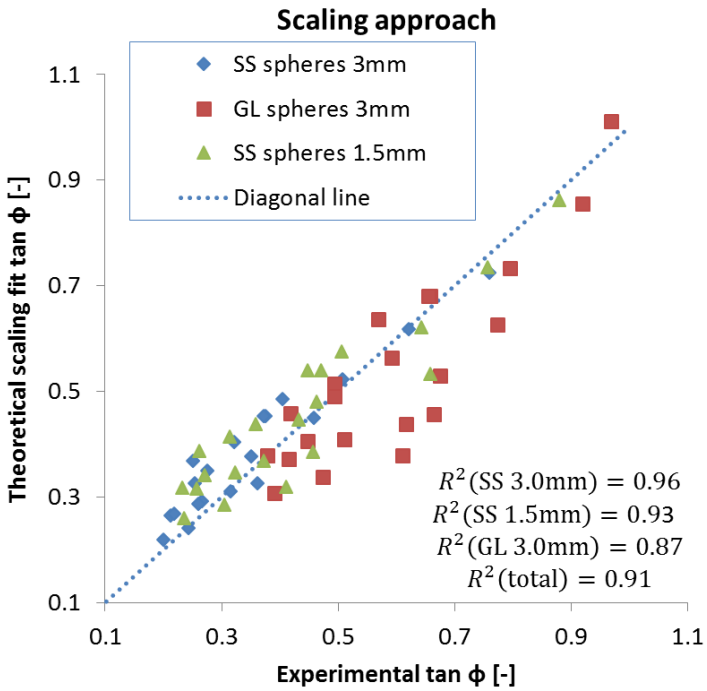

Figure 59: Validation of the scaling fit against experimental data.

The results of the regression analysis are shown in Figure 59. The average spreading of the stainless steel particles having 1.5 and 3 mm diameter is predicted reasonably well by (38),

with coefficient of determination $R^2_{SS1.5} = 0.93$ and $R^2_{SS3.0} = 0.96$. However, for the glass particles (red squares in Figure 59) the resulting coefficient of determination is lower, $R^2_{GL3.0} = 0.87$. This type of particles is spread on average better than Eq. (38) predicts. We observed in the experiments that glass particles residing in the pool can be entrained by the turbulent flow for a long time ranging from tens of seconds up to few minutes after particles delivery is stopped. Further analysis and tests are necessary in order to clarify this effect as well as to improve the proposed semi-empirical model.

4.4 Summary of Particulate Debris Spreading Research

4.4.1 Summary of PDS-C tests and scaling analysis

A set of PDS-C experiments has been carried out with different types of stainless steel particles and their mixtures in order to quantify particle flow rate in debris bed self-leveling phenomenon.

A scaling approach has been proposed for generalization of the experimental data on the non-dimensional particulate debris spreading rate. Application of proposed scaling approach to different PDS-C tests results in dense clustering of the data from different tests suggesting that the most important physical phenomena are captured properly.

Despite some remaining uncertainties, developed scaling method provides a viable approach to development of experimental closures universal for different types of particles, gas and coolant properties and flow characteristics.

More tests will be carried out in the future with particles made of different materials, mixtures of particles with different sizes and irregular shapes, etc. in order to extend the database for validation of the proposed closures and scaling approaches.

Obtained correlation has been used to predict evolution of the debris bed shape in time for reactor accident conditions. A comprehensive sensitivity and uncertainty analyses of the spreading efficiency is ongoing activity.

4.4.2 Summary of PDS-P tests and preliminary analysis

Experimental data and preliminary scaling approaches on particulate debris spreading driven by large scale turbulent flow in the pool are reported. The work is motivated by the need to provide separate effect validation data for the models which can assess effectiveness of the spreading of fragmented corium debris over the pool basemat in prototypic severe accident conditions.

The preliminary post-test analysis of the experimental data (in the case center-of-pool air injection) on particles spreading indicated that gas injection rate in the pool has strong influence on particle spreading and debris bed formation. The effectiveness of particle spreading has been introduced in order to compare the tests between each other.

Post-test analysis of the experimental data (in the case of side-pool air injection) suggests that the gas injection rate, pool dimensions, and particle properties have strong influence on debris bed formation. A semi-empirical scaling for the generalization of the data has been proposed demonstrating fairly good agreement with experimental data.

Further experimental work is required in order to develop a database of particle spreading in the pool with wider ranges of pool configuration, particle properties and debris release conditions. Improved scaling, such as inclusion of bubble-particle, turbulence-particle, particle-particle interactions into the scaling expression, might be helpful for further generalization of the data. The validation of the DECOSIM code for prediction of the influence of turbulent flow on falling particles trajectory is ongoing.

5 Analysis of ex-vessel steam explosion

Release of core melt from failed reactor vessel into a pool of water is adopted in several existing designs of light water reactors (LWRs) as an element of severe accident mitigation strategy. Corium melt is expected to fragment, solidify and form a debris bed coolable by natural circulation. However, energetic fuel-coolant interaction (steam explosion) can threaten containment integrity potentially leading to large early release of radioactive products to the environment.

The goal of this work is to develop a numerical computationally efficient tool for assessment of ex-vessel steam explosion risk in Nordic BWRs. The outcome of such assessment is foreseen as a map that denotes conditional failure probability of the containment in terms of input scenario parameters. For the assessment of the conditional (i.e. scenario wise) containment failure probability due to ex-vessel steam explosion the SEIM (Steam Explosion Impact Map) framework is being developed. The framework links melt ejection and pool characteristics with resulting explosion loads and containment structural fragility. SEIM combines deterministic analysis with Monte Carlo based sampling to provide values of failure frequency which are then used to estimate conditional containment failure probabilities and failure domains as a function of model input parameters.

SEIM utilizes the TEXAS-V code for prediction of steam explosion energetics and an impulse propagation method to calculate explosion loads at sensitive locations in the containment. Together TEXAS-V and impulse propagation model define what we call the Full Model (FM).

Large number of calculations required by the framework makes direct application of the FM unfeasible. To improve numerical efficiency of the framework TEXAS-V code is substituted with a fast counterpart - Surrogate Model (SM) that reproduces TEXAS-V results.

In this report we present (i) overview of the TEXAS-V code and choice of sub-models, (ii) implementation of the model for steam explosion study in the reference Nordic BWR, (iii) definition of the response function for the characterization of the steam explosion energetics; (iv) development of the surrogate model, (v) current approach to the calculation of the conditional failure probability and some examples of the mapping of the failure domain.

5.1 TEXAS-V code

The Texas-V is a 1D 3-field transient code with Eulerian fields for gas and liquid and Lagrangian field for fuel particles. It comprises two modules: one for calculation of premixing and another one for calculation of steam explosion.

The **premixing model** is based on conservation equations and two key constitutive models: the *fragmentation model for mixing* and the *phase change model*. All of them are applied in three flow regimes: bubbly flow, droplet flow and transition flow.

The fuel fragmentation is due to the following mechanisms:

- Rayleigh-Tailor instability
- Boundary layer stripping
- Kelvin-Helmholtz instability

Kelvin-Helmholtz instability and boundary layer stripping are considered to have minor effect with vapor film present and are reduced rapidly with rise of void fraction.

The Rayleigh-Tailor instability model is thus the key constitutive relation in TEXAS describing fuel fragmentation. It was developed by Chu and Corradini [74] based on Pilch's [47] original concept of a multi-step fragmentation theory for liquid particles. The model considers the fuel particles to be deformed and dynamically fragmented into a discrete number of particles from its initial diameter to smaller sizes. The implemented equations are as follows:

$$D_f^{n+1} = D_f^n \left(1 - C_o \Delta T^+ We^{0.25}\right)$$

$$We = \frac{\rho_c U_{rel}^2 D_f^n}{\sigma_f}$$

$$\Delta T^+ = \frac{U_{rel}\left(t^{n+1} - t^n\right)}{D_f^n}\left(\frac{\rho_c}{\rho_f}\right)^{1/2}$$

$$C_o = 0.1093 - 0.0785\left(\frac{\rho_c}{\rho_f}\right)^{1/2}$$

where n is time iteration index; D_f is fuel particle diameter; ΔT^+ is dimensionless time step; U_{rel} is relative velocity; t is time; σ_f is fuel surface tension; ρ_f, ρ_c are densities of fuel and coolant respectively.

The melt jet is represented in the form of discreet master particles that fall into water pool sequentially. It is further assumed that coherent fuel jet will not breakup until the fuel particle at the leading edge exposed to the oncoming coolant is fragmented (and swept away from the interface), that is only master particle at the leading edge of the jet can be subject to fragmentation. Two alternative mechanistic approaches are implemented in TEXAS-V as driving the onset of leading particle breakup:

- Leading edge breakup.
- Trailing edge breakup.

The trailing edge algorithm forces leading master particle to fragment at the tail of the fragmented debris, i.e. at the beginning of the premixing region. *Leading edge* algorithm implies start of the leading master particle fragmentation at the leading front of the fragmented debris, i.e. at the end of the premixing region. The trailing edge regime provides very slow jet propagation (limited by sedimentation of fragmented particles) and high rate of primary breakup. It is intended to predict fragmentation rates of small jets prone to sinusoidal instability. Differences in the prediction of jet propagation and void generation (as an indicator of fragmentation rate) are provided in Figure 60.

Given characteristic scales of melt release in reactor case we consider leading edge regime to provide adequate prediction of jet breakup and propagation velocity; this is also in line with MC3D calculations of jet front propagation in water.

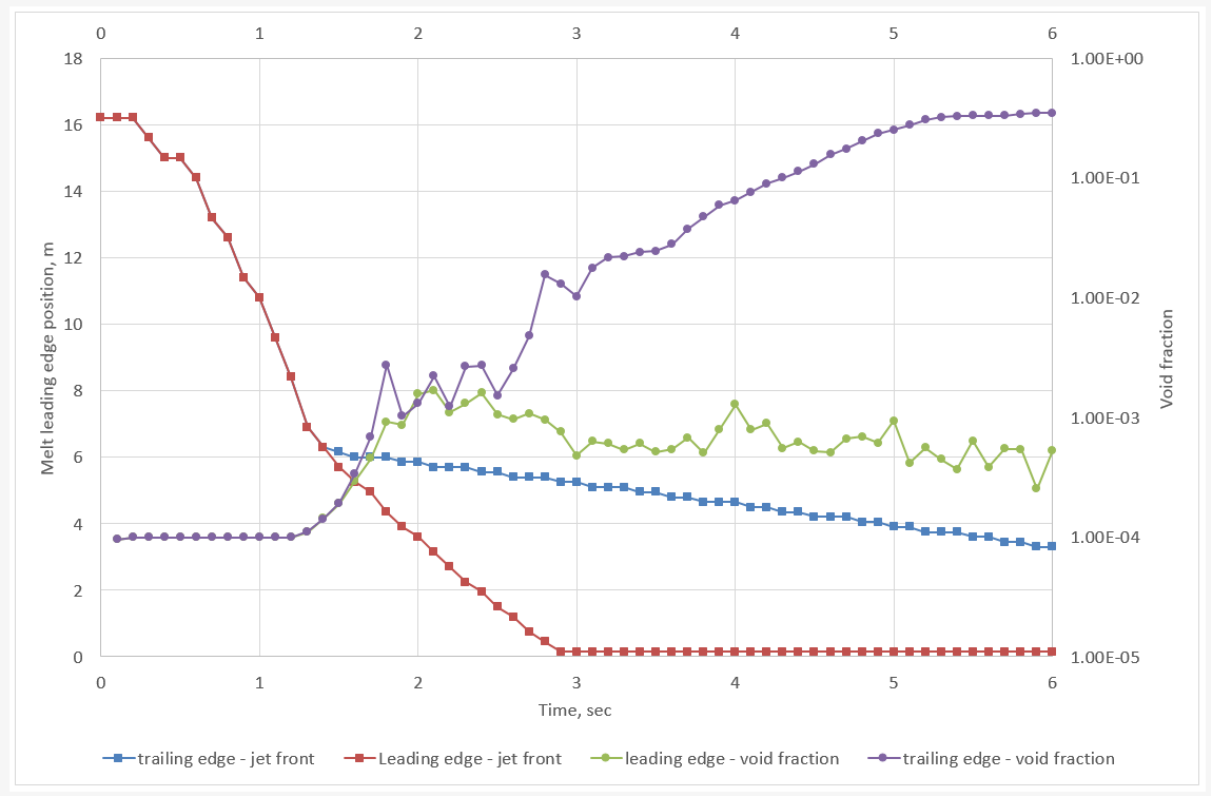

Figure 60: Trailing edge breakup vs leading edge breakup mechanisms.

The phase change model (in continuous liquid field) comprises of two primary equations that define:

1. Heat loss from fuel particles $\dot{q}_{fuel}$:

$$-\dot{q}_{fuel} = \pi D_f^2 h_{film}\left(T_f - T_{sat}\right) + \pi D_f^2 \sigma F\left(T_f^4 - T_{sat}^4\right),$$

where the first term (on the right hand side of the equation) describes convection heat transfer rate from fuel particle to the liquid vapor interface, and the second term is the radiation heat transfer rate from the fuel particle to the saturated liquid-vapor interface. Temperature profile inside a particle is solved in simplified way using steady state approach: it is assumed spatially constant in the bulk and linearly decreasing within a thin thermal layer δ.

The corresponding steam generation rate $\dot{\mathrm{M}}_{\mathrm{s,p}}$ is then deduced from:

$$-\dot{q}_{fuel} = \pi\left(D_f + 2\delta_{film}\right)^2 h_{lg}\left(T_f - T_{sat}\right) + C_{rad}\pi D_f^2 \sigma F\left(T_f^4 - T_{sat}^4\right) + \dot{\mathrm{M}}_{\mathrm{s,p}} h_{fg},$$

where the first term on the r.h.s. is convection heat transfer rate from the liquid-vapor interface around the fuel particle to bulk liquid field and the second term is the fraction C_{rad} of radiation heat flux that is absorbed in the subcooled liquid; h_{fg} is the latent heat of steam.

2. Heat flux balance around steam bubbles and resulting steam generation rate $\dot{\mathrm{M}}_{\mathrm{s,b}}$:

$$A_{gL}K_g\frac{\left(T_g - T_{sat}\right)}{\delta_g} = A_{gL}h_{L.sL}(T_{sat} - T_L) + \dot{\mathrm{M}}_{\mathrm{s,b}}h_{fg}$$

where the term on the l.h.s. of the equation is the vapor bubble-side heat transfer rate; the first term on the r.h.s. is the bulk liquid-side heat transfer rate; A_{gL} is the surface area of the interface between the liquid field and the vapor field as determined from the vapor bubble radius and the flow regime.

The net rate of steam generation $\dot{m}_s$ per unit volume is thus can be expressed in terms of the net heat flux $\dot{q}_{net,f}$

$$\dot{m}_s = \frac{\dot{q}_{net,f}}{h_{fg}V_{cell}}$$

$$\dot{q}_{net,f} = \dot{q}_{fuel} - \dot{q}_l - \dot{q}_v$$

where $\dot{q}_l$ and $\dot{q}_v$ are the heat received by coolant liquid and coolant vapor respectively, which becomes the internal energy of the coolant; and V_{cell} is cell volume.

The **dynamic fine fuel fragmentation** (upon steam explosion) is due to the fragmentation model proposed by Tang and Corradini [63] which is largely based on the original Kim's model [19]. It is a combination of thermal and hydrodynamic effects, which conceptually can be summarized as:

1. Film boiling around a molten fuel particle
2. Film collapse by external pressure pulse
3. Coolant micro-jets impingement on the surface of and possibly inside fuel particle
4. Rapid coolant expansion and fragmentation of the fuel into droplets

Being computationally expensive it is replaced in TEXAS with a semi-empirical equation where fragmentation rate $\dot{m}_f$ expressed as:

$$\dot{m}_f = Cm_p \cdot \left(\frac{P - P_{th}}{\rho_c R_p^2}\right)^{0.5} F(\alpha) g(\tau)$$

where m_p is mass of the initial particle; R_p is radius of the initial particle; P_{th} is the threshold pressure necessary to cause film collapse; P is ambient pressure; $F(\alpha)$ is the compensation factor for coolant void fraction; and $g(\tau)$ is the factor for available fragmentation time.

The factor $F(\alpha)$ is introduced to keep the correlation consistent with mechanism of the model because film collapse and coolant jet impingement become less likely to occur as vapor fraction increases. The factor $F(\alpha)$ decrease from 1 to 0 at $\alpha = 0.5$. In the TEXAS input file this limit is named ALPHAS.

The threshold pressure P_{th} is evaluated based on theoretical work by Kim and experimental data. At ambient pressure 1 Bar the threshold pressure is in the range from 2 to 4 Bars. As the ambient pressure increases threshold pressure also increases, however no definite quantitative values have been suggested. In the TEXAS input file this parameter is designated as POLD. *In this study we define threshold pressure as* $P_{th} = P + 1bar$.

The integral fragmentation mass depends on the duration of the fragmentation process which in case of the Kims model for a single droplet is of cyclic manner with sequential events of film collapse, fine fragmentation of drop surface, reestablishment of the vapor film followed again by film collapse etc. In reality due to concurrent fragmentation of many drops this process can continue only for a limited time. The factor $g(\tau)$ is introduced as empirical approach to account for the characteristic fragmentation time τ during which Kims mechanism is considered to be operative. The factor $g(\tau)$ decreases from 1 to 0 as this characteristic time is exceeded. At ambient pressure (1Bar) the recommended value for it is 4 ms but often values on the order of 10 ms have been used. It is indicated that as ambient pressure increases the fragmentation limit time decreases. In the TEXAS input file this parameter is designated as TFRAGLIMT; we optimize its value between 10 to 0 ms during explosion calculations to obtain maximum explosion impulse.

The heat generated due to dynamic fine fragmentation is expressed in TEXAS as:

$$\dot{q}_{frag} = \dot{m}_f \cdot (C_{pf} \cdot (T_f - T_s) + i_f)$$

where i_f is fuel latent heat; T_f is fuel temperature; T_s is saturation temperature of the coolant; C_{pf} is specific heat for the fuel. Due to extremely fine fragmentation of the fuel the rate of heat transfer is so fast that it is assumed to generate steam only giving the following equation for steam generation rate $\dot{m}_s$ per unit volume:

$$\dot{m}_s = \frac{\dot{q}_{net,f} + \dot{q}_{frag}}{h_{fg} V_{cell}}$$

It is stated in the Tangs thesis that the current model reflects the key features of the "chain-reaction" required for the rapid escalation and propagation of the vapor explosion, i.e.:

- The pressure shock wave directly contributes to rapid fuel fragmentation;
- The fragmented fuel is quenched by the coolant, generating more vapor;
- The increased vapor mass raises the local pressure and sustains the shock wave propagation to neighboring fuel-coolant mixture regions.

Further details on the implemented models in TEXAS can be found in the original thesis by Chu [74] for premixing model and by Tang [63] for propagation model.

TEXAS-V code generates several output files for premixing and explosion. Data on Lagrangian particles is also provided.

All computational results reported hereafter were obtained using the leading edge breakup mechanism and the coherent jet release model. The model for hydrogen generation is not used: it is believed, though yet to be verified, that hydrogen generation model will decrease explosion impulses if activated. TEXAS-V does not model crust formation; consequently, effect of the crust on the fine fragmentation during explosion propagation is neglected.

5.2 Full Model (FM)

Modelling of steam explosion was implemented assuming release of a single melt jet. In the calculations the jet diameter was varied in the range between 70 to 600 mm; initial system

pressure between 1 and 4 bars; water subcooling in the range from 10 to 128 K, water pool depth between 5 and 9 m. The height of the computational domain, from the point of melt release to the bottom of the water pool, was 13.0 m.

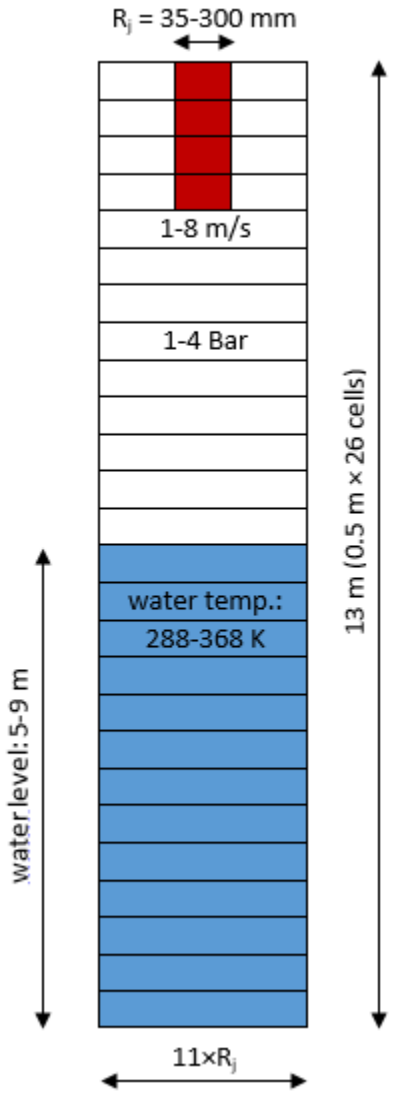

The computational domain was vertically divided onto 26 cells, each 0.5 m high with the same cross section area. The effect of the cell height on TEXAS-V calculations was separately studied. Results suggest that with the decrease of the cell height in the range from 0.2 to 0.4 m explosion impulses get weaker and the number of failed calculations increases; explosion impulses were not affected when mesh cell height was varied from 0.4 to 0.6 m.

The mesh cell cross section area has profound effect on the dynamic pressure and consequently on the explosion pressure impulse. A robust approach to defining the cell cross section area would require application of a 2D FCI code to determine the minimal radial extent of the premixing region where averaged 2D solution remains independent from the radial extent. This is a tedious and complex task. However, it was found that in TEXAS-V for the chosen ranges of input parameters the product of the pressure impulse and cell cross section area [m^2] is practically independent from the cell cross-section area (see **Figure 61**). Considering further that TEXAS-V was extensively validated against KROTOS experimental data, we set the ratio of the jet radius (R_{jet}) to cell radius (R_{cell}) approximately the same as in the KROTOS experiments. In this work the following relation has been used:

$$R_{cell} = 11.0 \cdot R_{jet} \qquad (5.1)$$

Reduced time steps were chosen to decrease the number of failed calculations, specifically, the time step for premixing calculations was set from 10^{-8} to 10^{-6} s and the time step for explosion was in the range between 10^{-8} and $5 \cdot 10^{-7}$s.

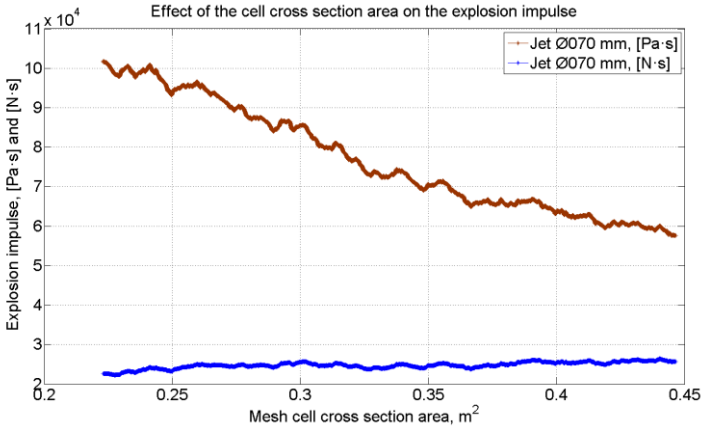

Figure 61: Effect of the mesh cell cross section area on the explosion impulse

Two functions were derived from the TEXAS-V calculations: one for the characterization of the steam explosion, i.e. explosion impulse (F_{expl}); and one for the characterization of the premixing, i.e. total surface area of liquid melt droplets in water (F_{prmx}).

Explosion impulse was integrated from the dynamic pressure history:

$$F_{expl} = \max\left(\sum_i \left(P_{ij} - P_{0j}\right)\delta t_i\right) \cdot A_{cell},\ [N \cdot s] \tag{5.2}$$

where P_{ij} is pressure in the cell j at the time instance i; P_{0j} is pressure in the cell j at time 0; δt_i is the time step at the time instance i, A_{cell} – mesh cell cross section area.

The total surface area of liquid melt droplets in water was approximated as:

$$F_{prmx} \propto \sum_k \begin{cases} n_k R_k^2, & \left[Vs_{i(k)} < 0.5,\ T_k > T_{melt}\right] \\ 0, & otherwise \end{cases},\ [m^2] \tag{5.3}$$

where k is Lagrangian particle group number; R_k is particle radius in the k particle group; n_k is number of particles in k particle group; T_k is particle bulk temperature in the k particle

group; T_{melt} is melting temperature of the fuel; $Vs_{i(k)}$ is steam fraction in the cell i where k particle group is located.

The explosion impulse in eq. (5.2) is in [N·s]. In order to make it meaningful for risk analysis one must refer it to a specific area (provide explosion pressure impulse [Pa·s]), and apply an appropriate impulse propagation method to estimate the explosion impulse at relevant locations in the containment.

It is assumed that the explosion pressure impulse I [Pa·s] (similar to pressure distribution in a propagating spherical shock wave) is a decaying function of distance r from the center of the explosion:

$$I = \tilde{c} \cdot r^{\nu}, \nu \cong -1, \tilde{c} = const \tag{5.4}$$

The constant $\tilde{c}$ in eq.(5.4) can be estimated assuming explosion impulse F_{expl} to be distributed over the complete area of the containment base A_b and considering the point source of the explosion to be located in the center of the corresponding cell in TEXAS:

$$I_b = F_{expl}/A_b \tag{5.5}$$

$$I_b = \frac{2}{r_b^2}\int_0^{r_b} \frac{\tilde{c}}{(h_c^2 + r^2)^{0.5}} \cdot r dr \tag{5.6}$$

$$I(r) = I_b \cdot \frac{r_b^2}{2 \cdot ((r_b^2 + h_c^2)^{0.5} - h_c)} \cdot \frac{1}{r} \tag{5.7}$$

where r_b is the radius of the containment; h_c is elevation of the computational cell above the bottom of the domain. The impulse $\bar{I}_0$ at the center of the containment floor, i.e. at $r = h_c$, is then:

$$\bar{I}_0 = I_b \cdot \frac{r_b^2}{((r_b^2 + h_c^2)^{0.5} - h_c)} \cdot \frac{1}{2 \cdot h_c} \tag{5.8}$$

5.3 Response Function for steam explosion characterization

The deterministic model of steam explosion must provide a well-posed characterization of the explosion energetics. Above we have defined explosion impulse as the key characteristics of the explosion energetics. In the following we address the well-posedness of the explosion impulse.

The time dependences of normalized premixing F_{prmx} and explosion F_{expl} functions are provided in Figure 62. The data was obtained given fixed melt release conditions. The first ~1.4s of melt release correspond to the jet propagation above the water pool. The following ~300 ms of melt-water interaction occur with no apparent correlation between the two functions. Then the two response functions develop correlated and periodic behavior. The latter is most likely driven by the periodic arrival of jet particles and the competing nature of the secondary fragmentation rate and rate of fine particles solidification. Note that if the premixing function was defined as liquid melt volume / mass, i.e. taken proportional to $\sum n_k R_k^3$ the corresponding curve in Figure 62 would be monotonously rising.

Figure 62 demonstrates that small variations in the triggering time lead to large changes in the explosion energetics. For example, between 1.90 and 2.01 s, i.e. within 110 ms time window, the explosion impulse changes almost 50 times, i.e. from 377 kPa·s to 8 kPa·s.

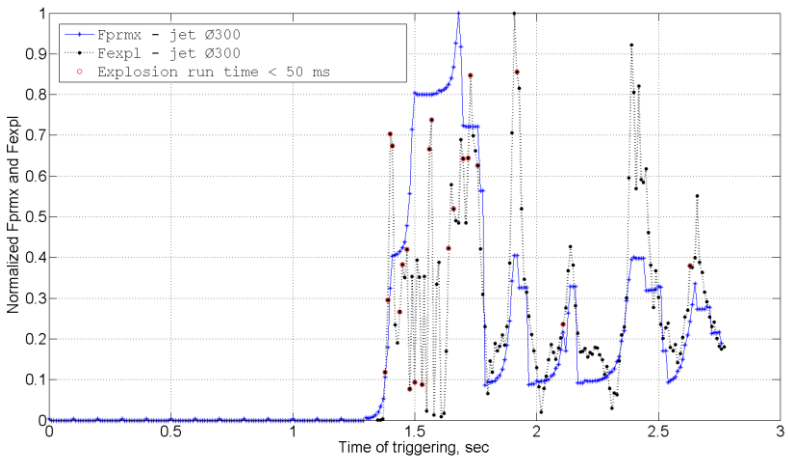

Figure 62: Dependence of premixing and explosion criterions on the triggering time (release of oxidic corium melt with jet Ø300 mm into a 7 m deep water pool)

High sensitivity of the explosion impulse to the triggering time has far-reaching consequences which are not necessarily TEXAS specific. First, it demonstrates physical ill-posedness of FCI codes, i.e. chaotic nature of the steam explosion impulse with respect to the discreet triggering time. If triggering time is reluctantly treated, interpretation of FCI code results and code parametric studies becomes a subject of considerable uncertainty.

Second, from the risk perspective, the choice of the triggering time given specific conditions of melt release can alter containment failure from physically unreasonable to physically unavoidable. In this sense choice of the triggering time should be driven by probabilistic or statistic considerations and should not be leveled by conservative or best estimate arguments.

Third, in FCI experiments the chaotic nature of steam explosion is expected to manifest in a stochastic way. The reason is the aleatory variability of the triggering time and melt release conditions that are not controlled or measured. Considering impulse ranges in Figure 62, the expected magnitude of the aleatory uncertainty in the experimental steam explosion impulses can potentially exceed the effect of other parameters controlled or intentionally varied in experiments.

The above results demonstrate that explosion impulse is ill-posed, i.e. exhibits chaotic behavior with respect to the triggering time. Aleatory variability of the explosion impulse can be encompassed by establishing its statistical characterization. For example, evolution of the explosion impulse in Figure 63a can be considered as aleatory and characterized in the form of the cumulative distribution shown in Figure 63b. In this case explosion impulses can be characterized in probabilistic terms:

– Probability of explosion impulse to exceed 80 kPa·s is 0.25% (or the confidence that explosion impulse will not exceed 80 kPa·s is 99.75%).
– Probability of explosion impulse to exceed 50 kPa·s is 5.0% (or the confidence that explosion impulse will not exceed 50 kPa·s is 95.0%)
– Probability of explosion impulse to exceed 25 kPa·s is 14.0% (or the confidence that explosion impulse will not exceed 25 kPa·s is 86.0%)

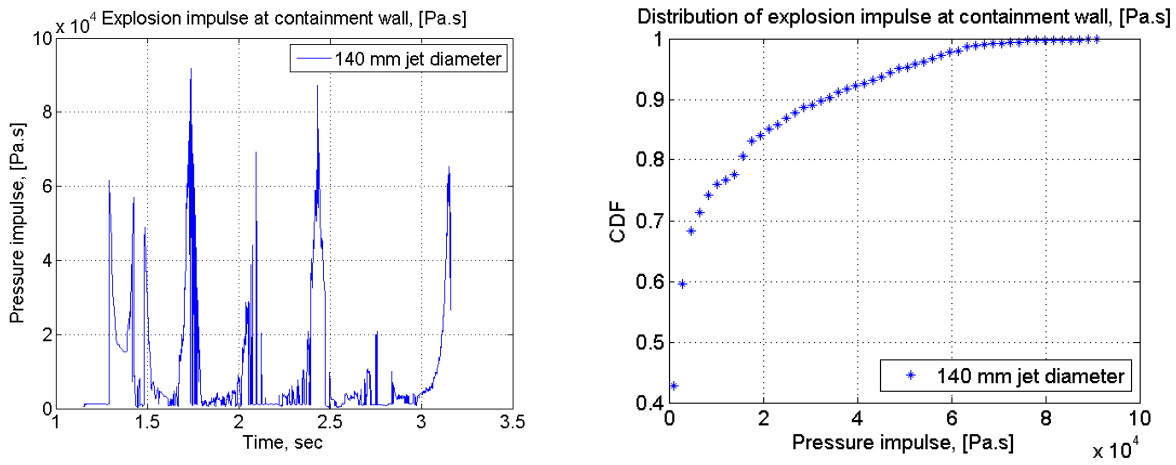

a b

Figure 63: Evolution of the explosion impulse as a function of triggering (a) and respective exposion impulse distribution (b)

For simplicity we estimate mean $\bar{F}_{expl}$ and standard deviation $\bar{F}_{std}$ of the explosion impulses obtained varying the triggering time:

$$\bar{F}_{expl} = \frac{1}{N}\sum_{m=1}^{N} F_{expl_m} \tag{9}$$

$$\bar{F}_{std} = \left[\frac{1}{N}\sum_{m=1}^{N}\left(F_{expl_m} - \bar{F}_{expl}\right)^2\right]^{\frac{1}{2}} \tag{10}$$

where m is index for the discreet triggering time $t_{trig} = t_0 + dt_{trig} \cdot m$.

It can be demonstrated that the group $\{\bar{F}_{expl}, \bar{F}_{std}\}$ is well-posed and therefore can be used for implementation in the SEIM framework. Formulation of the response function as a combination of mean and standard deviation allows interpretation of loads in terms of confidence intervals and confidence levels.

Note that in general aleatory variability of the explosion impulse is not normally distributed and actual confidence levels are expected to be lower. While we hold to this assumption only temporarily it remains valid for impulses below 90-100 kPa·s (see **Figure** 64).

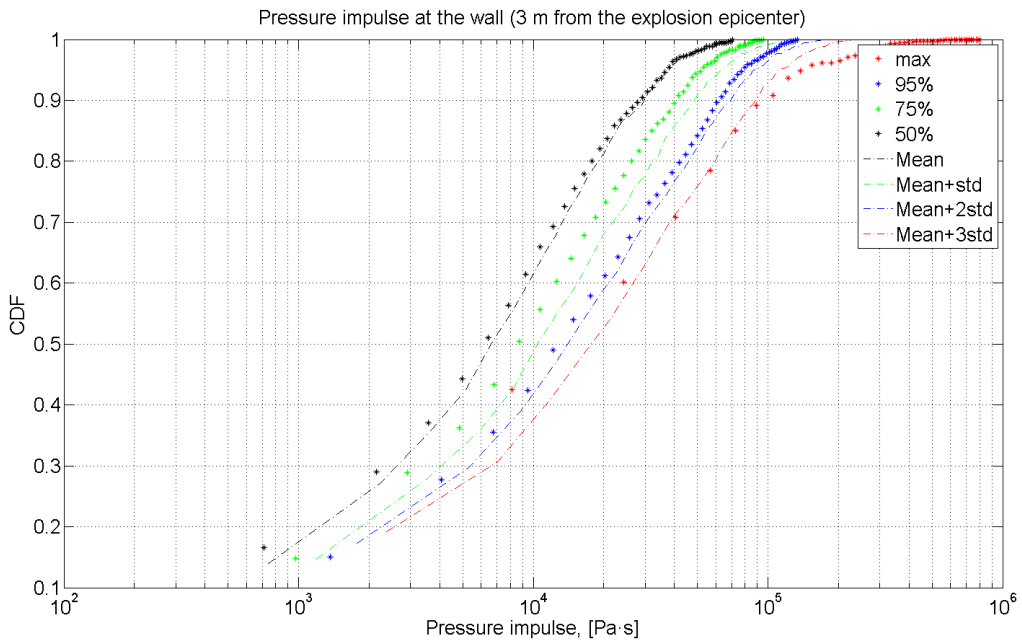

Figure 64: Distribution of the explosion load at the containment wall

5.4 Surrogate Model (SM)

Development of the SEIM Surrogate Model (SM) requires extended sampling of the Full Model (FM) to generate a high fidelity database of FM solutions. Minimization of the number of varied FM input parameters is necessary to make computational costs affordable. The complete set of tasks includes:

- definition of the list of important input parameters of TEXAS-V, i.e. FM sensitivity study followed by a screening exercise;
- generation of the database of TEXAS-V solutions in the space of important input parameters and verification of its physical consistency;
- choice of a method for development of the SM;
- implementation and validation of the SM.

Out of about 160 TEXAS-V input parameters 23 were selected for the sensitivity study. The complete list is provided in Table 16. Ranges of parameters used in the sensitivity study address scenario of oxidic melt release and were partially affected by TEXAS-V numerical stability. Parameters not mentioned in the Table 16 were set either in accord with TEXAS-V manual or according to recommendations in literature.

Table 16: Selected TEXAS-V parameters and their ranges

Parameter	Units	Range	Description
PO	**Pa**	**1÷4 E05**	**Initial pressure**
TLO	**K**	**288-366**	**Water temperature**
XPW	**m**	**3.2-8.2**	**Water level in the containment**
TGO	K	TLO	Cover gas temperature
TWO	K	TLO	Wall temperature
RPARN	m	0.07	Fuel injection radius
		0.15	
CP	**J/kg·K**	**400÷570**	**Fuel capacity**
RHOP	**kg/m3**	**7600-8600**	**Fuel density**
PHEAT	**J/kg**	**260÷360 E03**	**Fuel latent heat**
TMELT	K	2850	Fuel melting temperature
TPIN	**K**	**2850÷3150**	**Fuel injection temperature**
UPIN	**m/sec**	**1.5÷2.5**	**Fuel injection velocity**
KFUEL	**W/m·K**	**2÷11**	**Fuel thermal conductivity**
C(32)	**J/m2**	**0.4÷0.6**	**Fuel surface tension**
C(18)	**-**	**0.6÷0.9**	**Fuel emissivity**
DXI	m	0.5	Cell height
ARIY	**m^2**	**0.7÷1.8**	**Cell cross-section area**
		3.8÷8	
TMAX	sec	-	Premixing time
CFR	**-**	**2.0÷2.7 E-03**	**constant for rate of fuel fine fragmentation**
RFRAG	**m**	**8÷1.2 E05**	**Initial size of fragmented particles**
POLD	Pa	2×PO	Threshold pressure for film collapse
TFRAGLIMT	**s**	**0.0005÷0.0030**	**Fuel fragmentation time interval**
PTRIG	Pa	3E05	Trigger pressure

The sensitivity study was performed using Morris method [46], [50] and addressed 16 input parameters (written in bold in the Table 17). The mean pressure impulse ($\bar{F}_{expl}/A_{cell}$, [Pa·s]) has been used as the response function. The results in Figure 65 are provided for 140 mm jet diameter. The elements in the legend are sorted in descending order of Morris μ value. The error bars demonstrate the spread of the results established in 3 consecutive sensitivity studies that used slightly different number of trajectories.

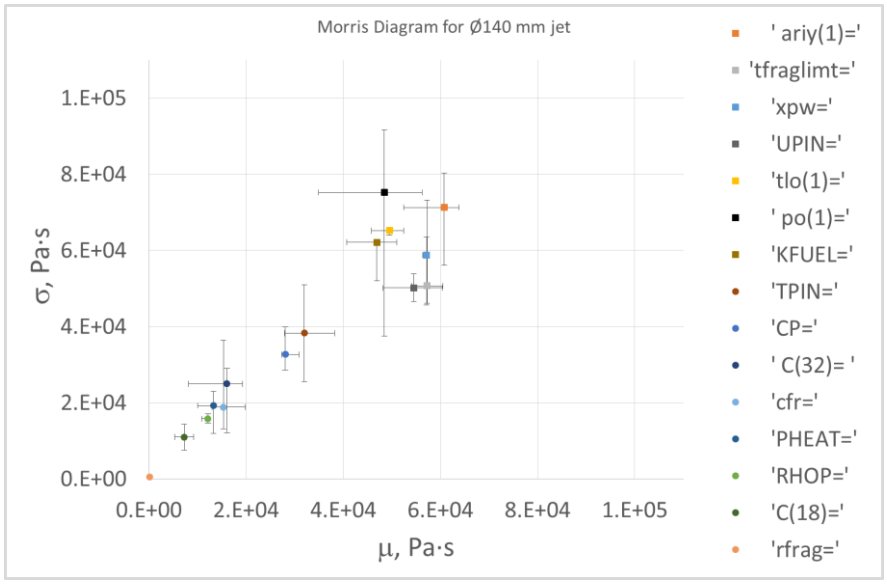

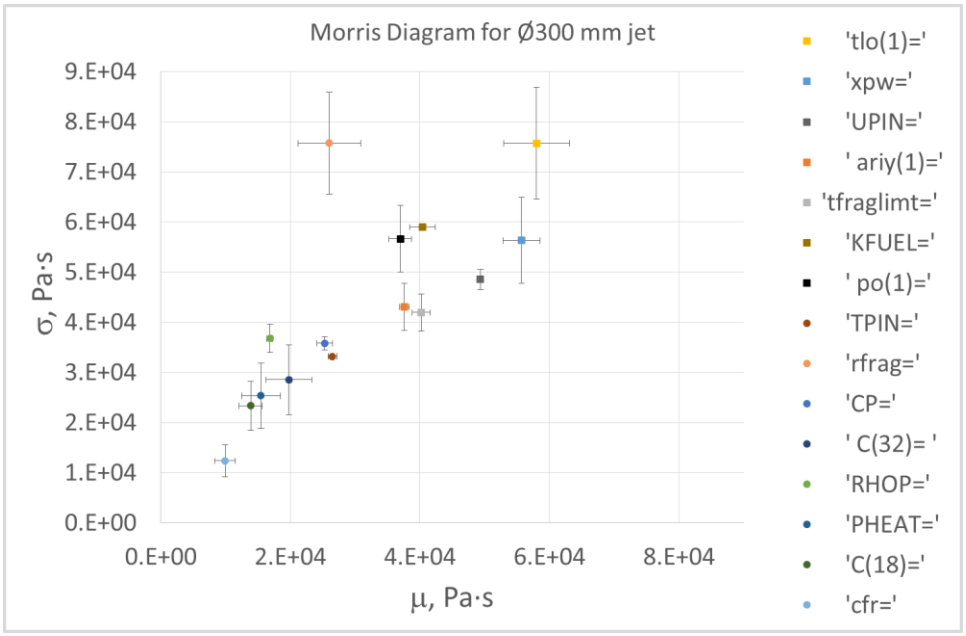

Figure 65: Morris diagrams for mean pressure impulse
(a – Ø140 mm jet; b - Ø300 mm jet)

Discrepancies in the two diagrams are due to TEXAS-V numerical failures which are more frequent in the case of Ø300 mm jet. Given rather high values of Morris σ we could justifiably screen out only three parameters: RFRAG, C(18) and ARIY.

The list of input parameters and their ranges used to generate the database of FM solutions is provided in the Table 17. Note that database is formulated to cover both oxidic and metallic releases, specifically extended ranges for melt superheat and thermal properties were applied.

Table 17: Ranges of input parameters used for generation of the database of FM solutions

#	Parameter	Units	Range		Explanation
			min	max	
1	XPW	m	5	9	Water level
2	PO	Bar	1	4	System pressure
3	TLO	K	288	368	Water temperature
4	RPARN	m	0.035	0.3	Initial jet radius
5	CP	J/kg·K	350	650	Fuel heat capacity
6	RHOP	kg/m3	7500	8500	Fuel density
7	PHEAT	J/kg	260 000	400 000	Fuel thermal conductivity
8	TMELT	K	1600	2800	Fuel melting point
9	TPIN	K	1620	3150	Melt superheat
10	UPIN	m/s	-8	-1	Melt release velocity
11	KFUEL	W/m·K	2	42	Fuel thermal conductivity
12	CFR	-	0.002	0.0027	Proportionality constant of fine fragmentation rate
13	TFRAGLIMT	ms	0.5	2.5	Fragmentation time

In order to evaluate the data for consistency of physical behavior and identify possible numerical ill-posedness the database has been extensively studied.

In the Figure 66 we provide Spearman correlation coefficients to three SRQs: explosion impulse (Ix), liquid melt surface area (LMSA), explosion runtime (ER).

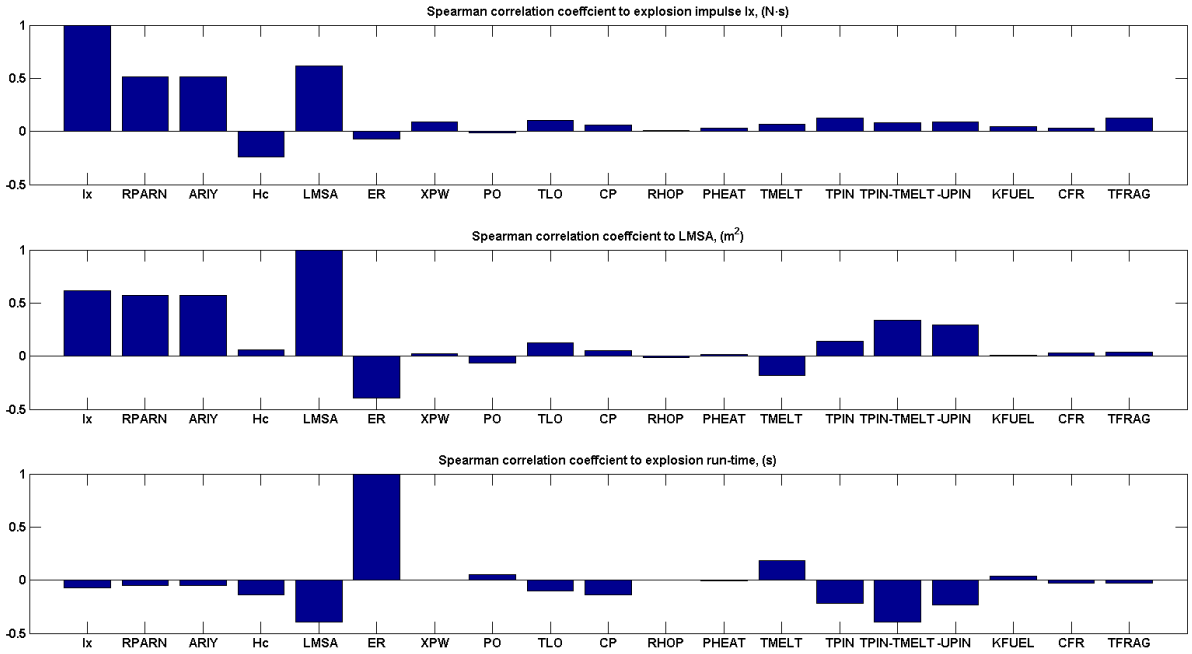

Figure 66: Spearman ranking of FM input parameters to three SRQs: Explosion Impulse [N·s], Liquid Melt Surface Area (LMSA), Explosion Runtime (ER)

We further derive Morris sensitivity measures for the same SRQs; those are demonstrated in the respective Morris diagrams in Figure 67-Figure 69.

Note that the database is obtained assuming linear correlation between cell cross section radius and jet radius, for that reason the two parameters have similar sensitivity measures. Jet diameter is influential input parameter and this is artificially reflected on the cell cross section area.

As it follows from provided diagrams the explosion impulse is most strongly correlated and is most sensitive to jet radius (RPARN/Rj), liquid melt surface area (LMSA), explosion run time (ER) and fine fragmentation time (TFRAGLIMT). (Pronounced correlation of cell elevation (Hc) with explosion impulse (Ix) is not yet clear, but that parameter is not in the list of actual FM input.) The liquid melt surface area is an inherent characteristic of the premixture development and therefore positive correlation is not surprising. Effect of jet radius (RPARN/Rj), also agrees with our expectations since it is proportional to the total amount of energy available for energetic interaction. The same argument applier for parameter TFRAGLIMT that defines the duration the energy is extracted from the melt during explosion. Interestingly, among three parameters: melt temperature, melt solidification point and melt superheat, melt temperature is the most influential towards explosion impulse.

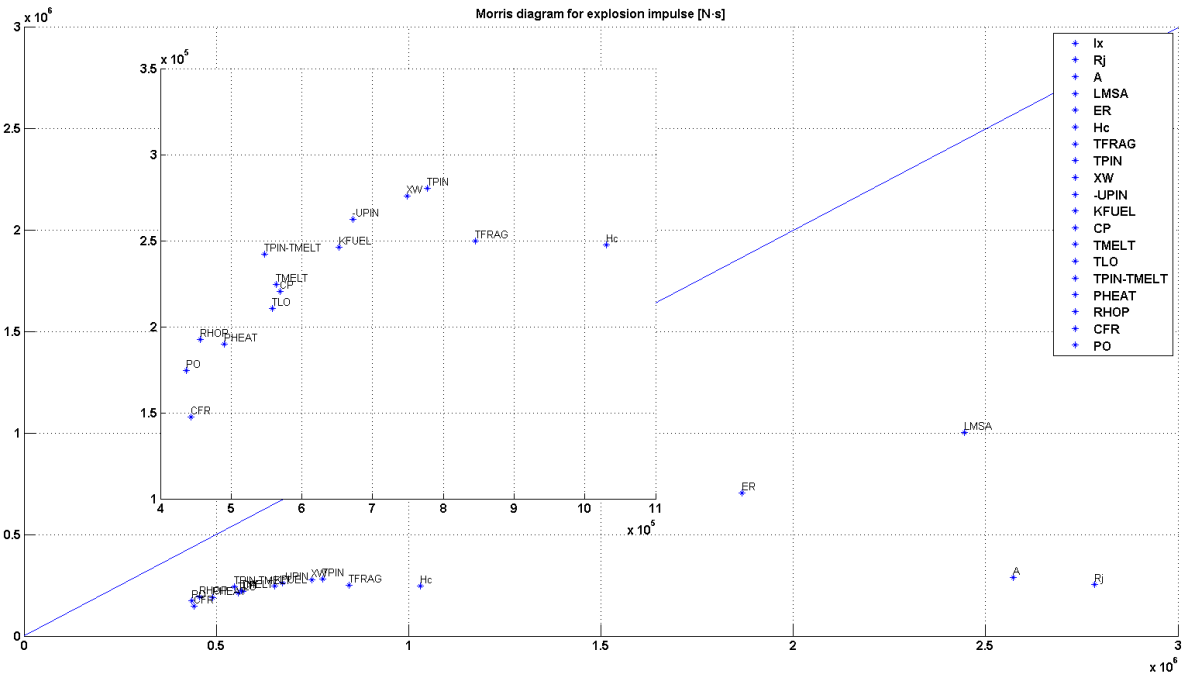

Figure 67: Morris diagram for Explosion Impulse [N·s]

According to the Morris diagram for the liquid melt surface area (see Figure 68), 3 most influential input parameters are jet diameter, melt superheat, melt release velocity. (High importance of the melting temperature and initial melt temperature is an artefact of data sampling: both affect the range of melt superheat, though in opposite ways). Remarkably, water temperature does not have pronounced effect. While this parameter is not water subcooling, its low influence suggests that the FM predicts rather low void fractions.

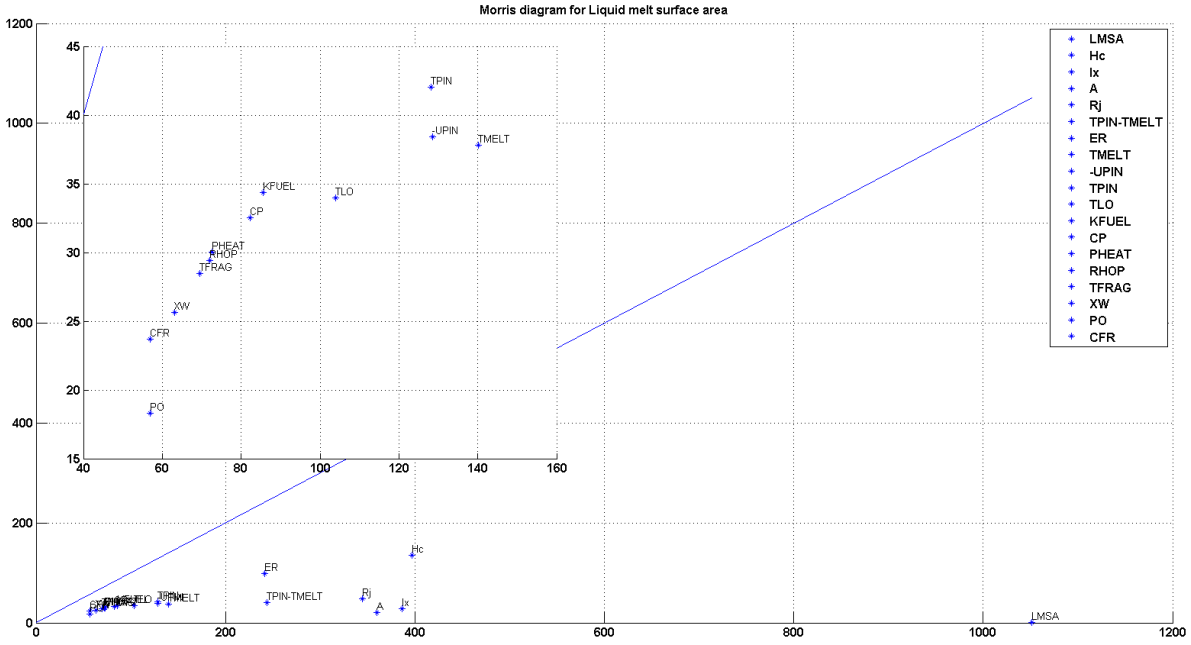

Figure 68: Morris diagram for Liquid Melt Surface Area (LMSA)

Above consideration confirm physical well-posedness of the generated database. However, largely non-zero sensitivity measures of explosion run time (clarify Figure 69) indicate that there are noticeable numerical issues. Indeed, as it follows from the Figure 70 at least 23% of performed calculations constitutes unfinished explosion cases, i.e. cases where explosion run time is less than user defined 50 ms.

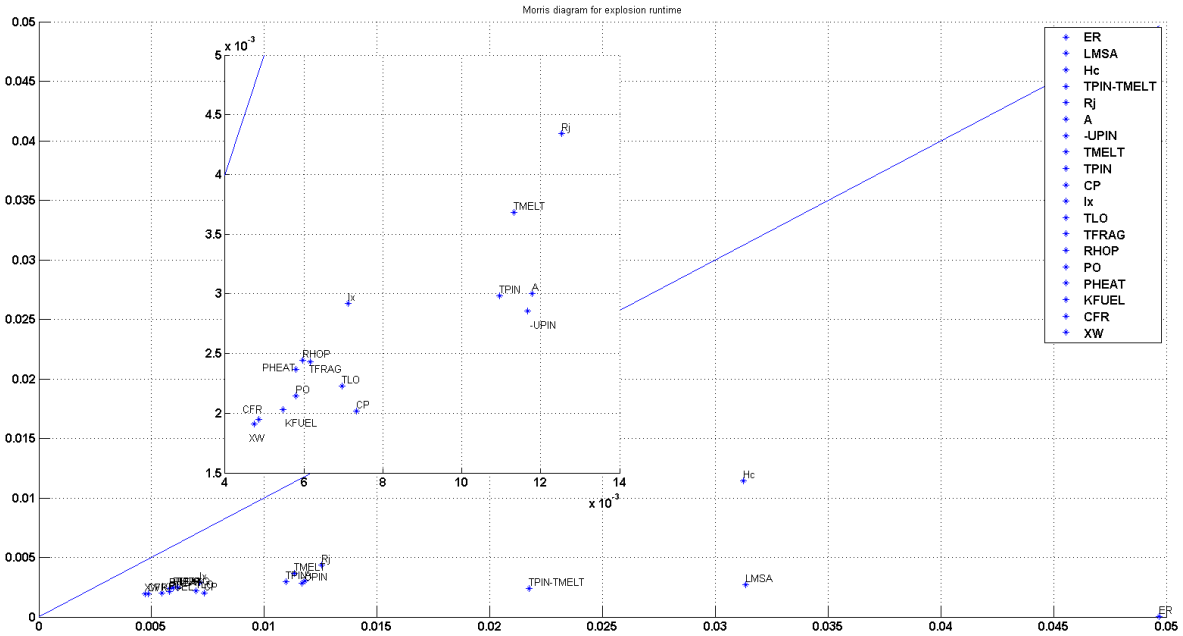

Figure 69: Morris diagram for Explosion Runtime

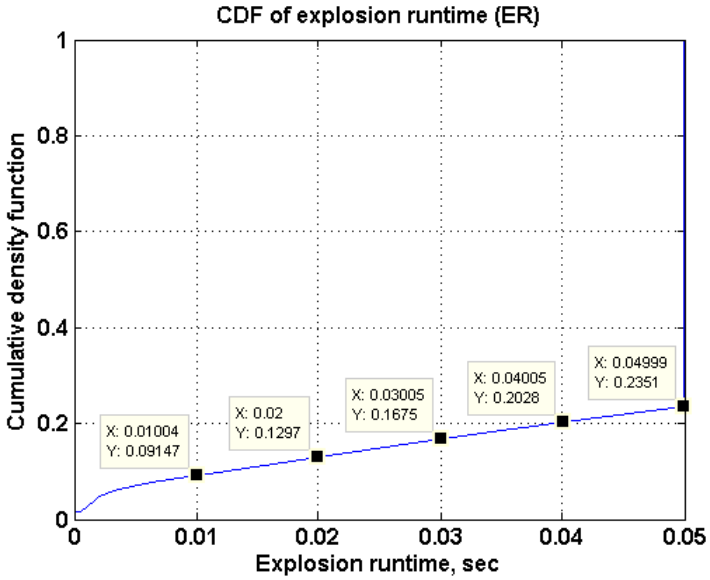

Figure 70: CDF of explosion runtime

The Morris diagram in the Figure 69 suggests that the higher the development of the premixing (LMSA) the higher is possibility of code failure during calculations of the explosion phase; that is further demonstrated in the Figure 71d. The most influential input parameters (driving LMSA) are melt superheat, jet radius and melt release velocity. Their effect is shown in Figure 71a-c. Limiting the ranges of melt superheat and release velocity could be beneficial to decrease the number of failed explosion calculations.

In order to provide FM solutions database that is not affected by failed explosion calculations we developed the following two step approach:

1. Premixing set, i.e. set of explosion cases that differ only in the triggering time, is removed from the database if number of cases with runtime below 40 ms exceeds 20%.
2. Estimation of the mean and standard deviation of the explosion impulse from the remaining premixing sets is performed excluding those cases that have explosion runtime below 10 ms, i.e. cases that most likely have produced zero or close to zero impulses due to failure of the calculation.

482 premixing sets have been removed from the original data set of 1500 premixing cases. The issue of filtering is that frequency of failed calculations grows with potential "explosivity" of the premixture. This makes filtering "selective" towards premixing sets with potentially high energetics and thus can undermine explosively of an input subspace.

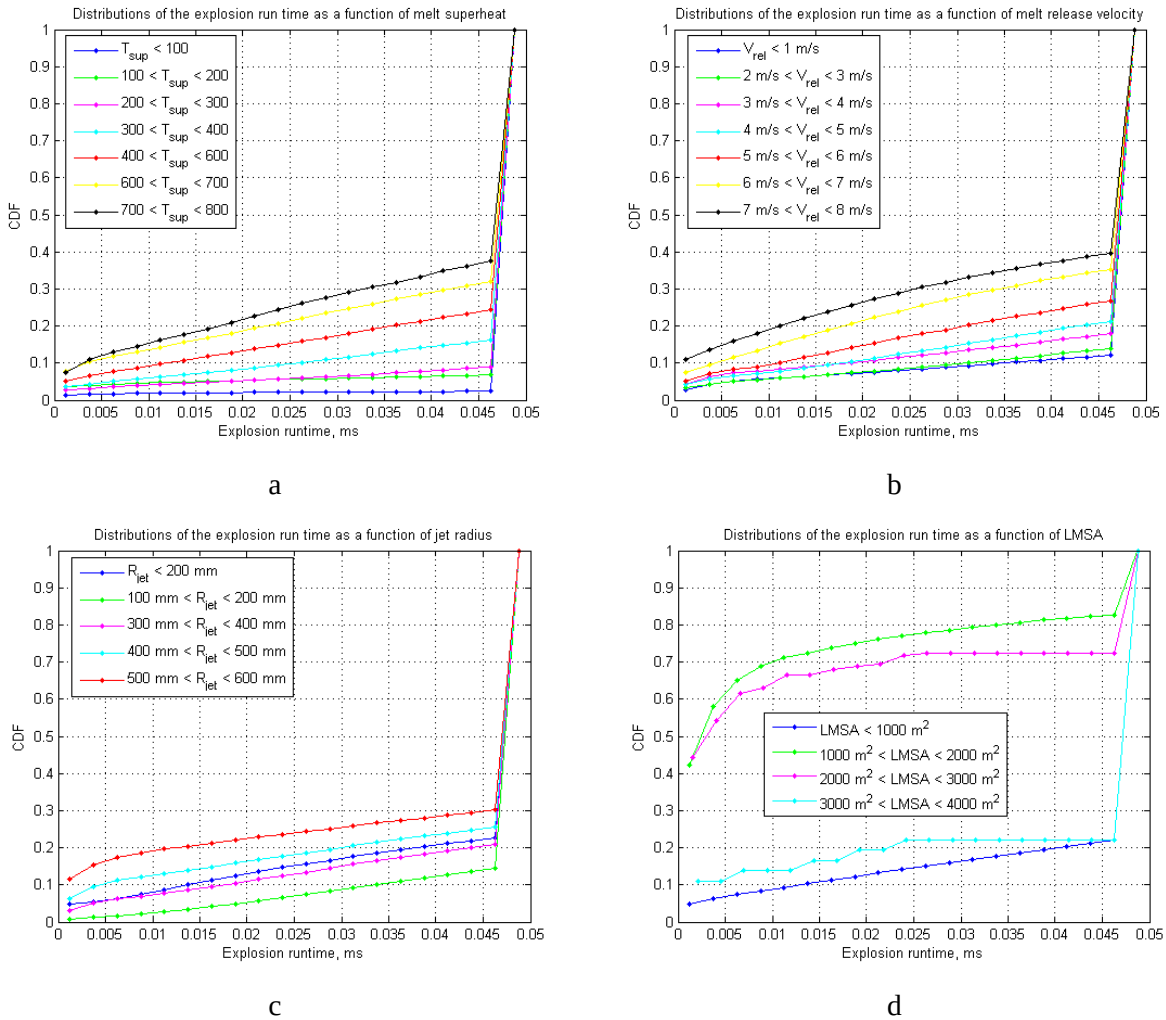

Figure 71: Distributions of the explosion runtime as a function of melt superheat (a), melt release velocity (b), jet radius (c) and LMSA (d)

The surrogate model has been developed using Artificial Neural Networks (ANNs) and filtered FM solution database. The ANN is trained to predict the mean and standard deviation of the impulse at the center of the containment floor and the containment wall (i.e. 3 m away from the explosion location) given 13 TEXAS-V parameters in the input: XPW, PO, TLO, RPARN, CP, RHOP, PHEAT, TMELT, TPIN, UPIN, KFUEL, CFR, and TFRAGLIMT.

The parity plots provided in the Figure 72and Figure 73 demonstrate good agreement between SM predictions and FM calculations. Though, extension of the current database of FM solutions and improvement of fidelity are necessary.

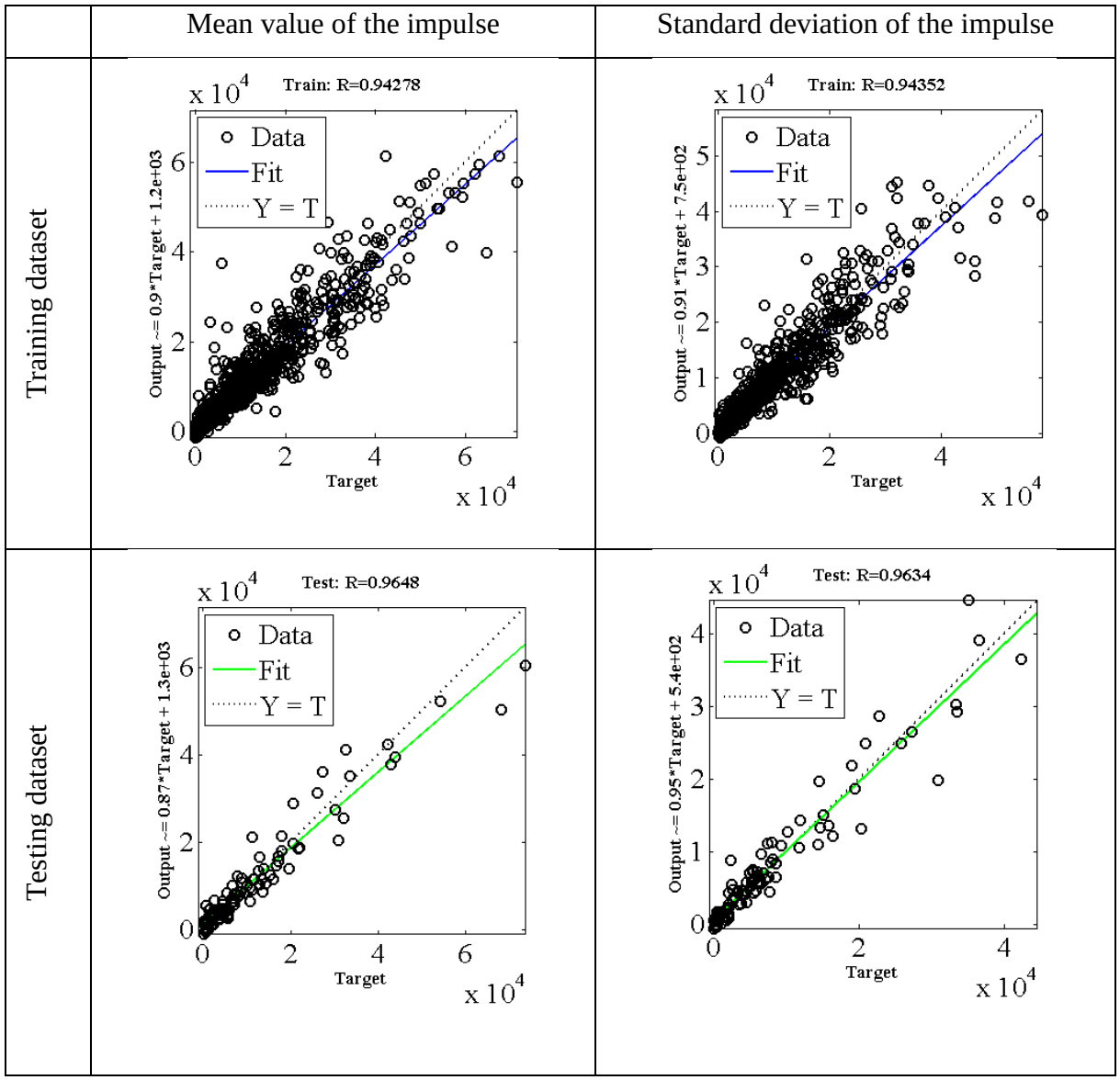

Figure 72: Parity plots for the explosion impulse at the drywell wall

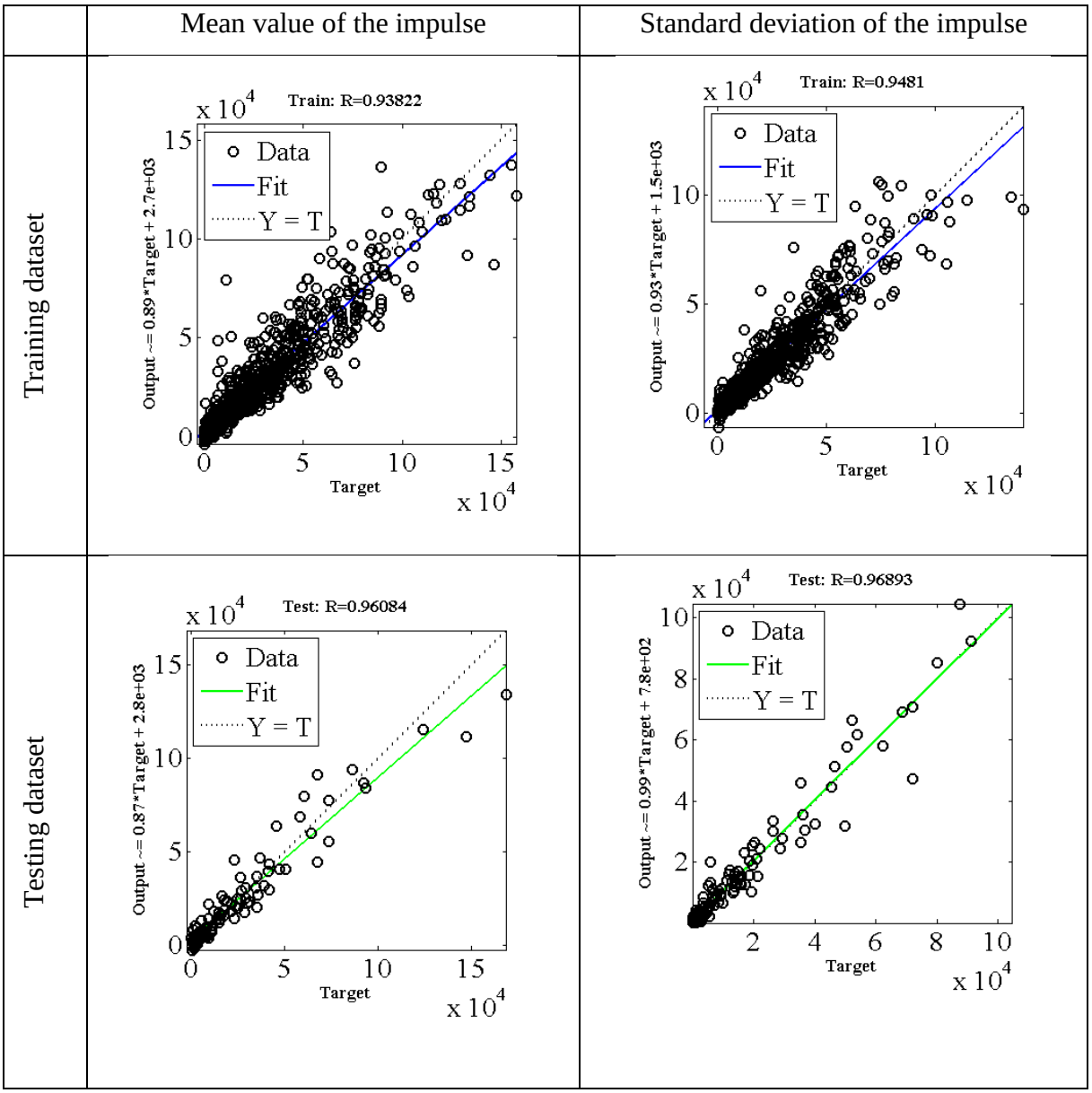

Figure 73: Parity plots for the explosion impulse at the drywell wall

5.5 Comparison of SM and FM

Comparison of CDFs of explosion impulse at the pedestal wall and at the base of the containment for two inputs: (i) training set, filtered from numerically failed cases, and (ii) prediction set obtained with random sampling are shown in the Figure 20. There is a good agreement between TEXAS and SM for the same training input dataset. However, for a randomly generated input data the SM predicts on average higher impulses. This is attributed to the combined effect of slightly larger mean values of the three most influential parameters in the random dataset: jet radius, melt superheat and melt release velocity (see Table 18).

In order to further verify that developed SM has properly captured physical behavior of the full model we provide a comparison of dependences of predicted impulses on separate parameters (Figure 21). The SM demonstrates a physically sensible response to the changes in the input parameters. Remarkably, the SM has captured the expected dependence between melt superheat (TPIN-TMELT) and explosion impulse in the ranges of parameters which were only sparsely covered in the filtered training data set.

Table 18: Mean values of input parameters in different input datasets

Parameter	**Units**	**Training dataset**		**Random**
		before filtering	**after filtering**	
RPARN	m	167.4	157.9	167.5
TPIN-TMELT	ºC	475.1	343.1	475.5
UPIN	m/s	4.498	4.183	4.496

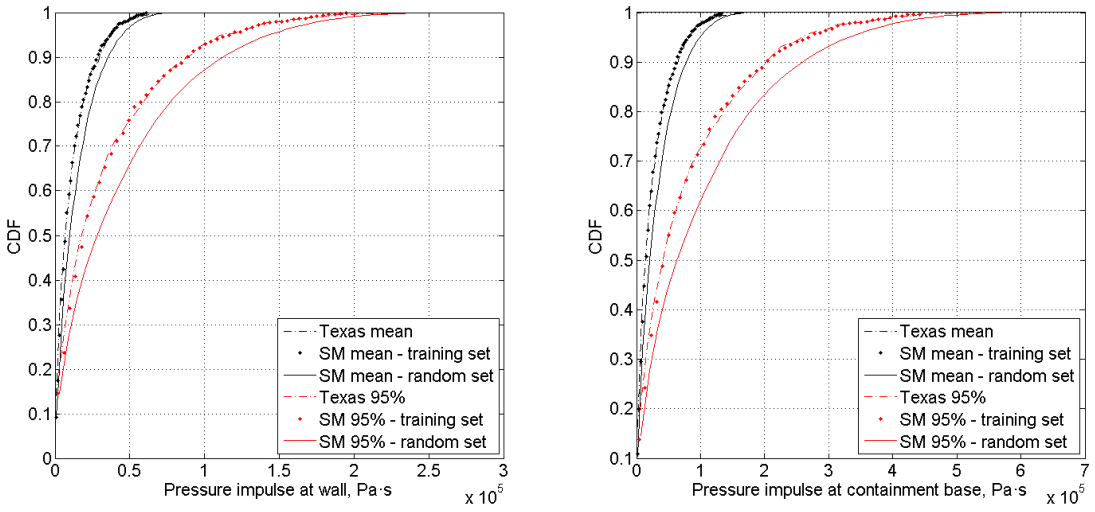

a b

Figure 20: CDFs of explosion pressure impulse at wall (a) and at containment base (b) by TEXAS, SM with the training input and SM with a random input

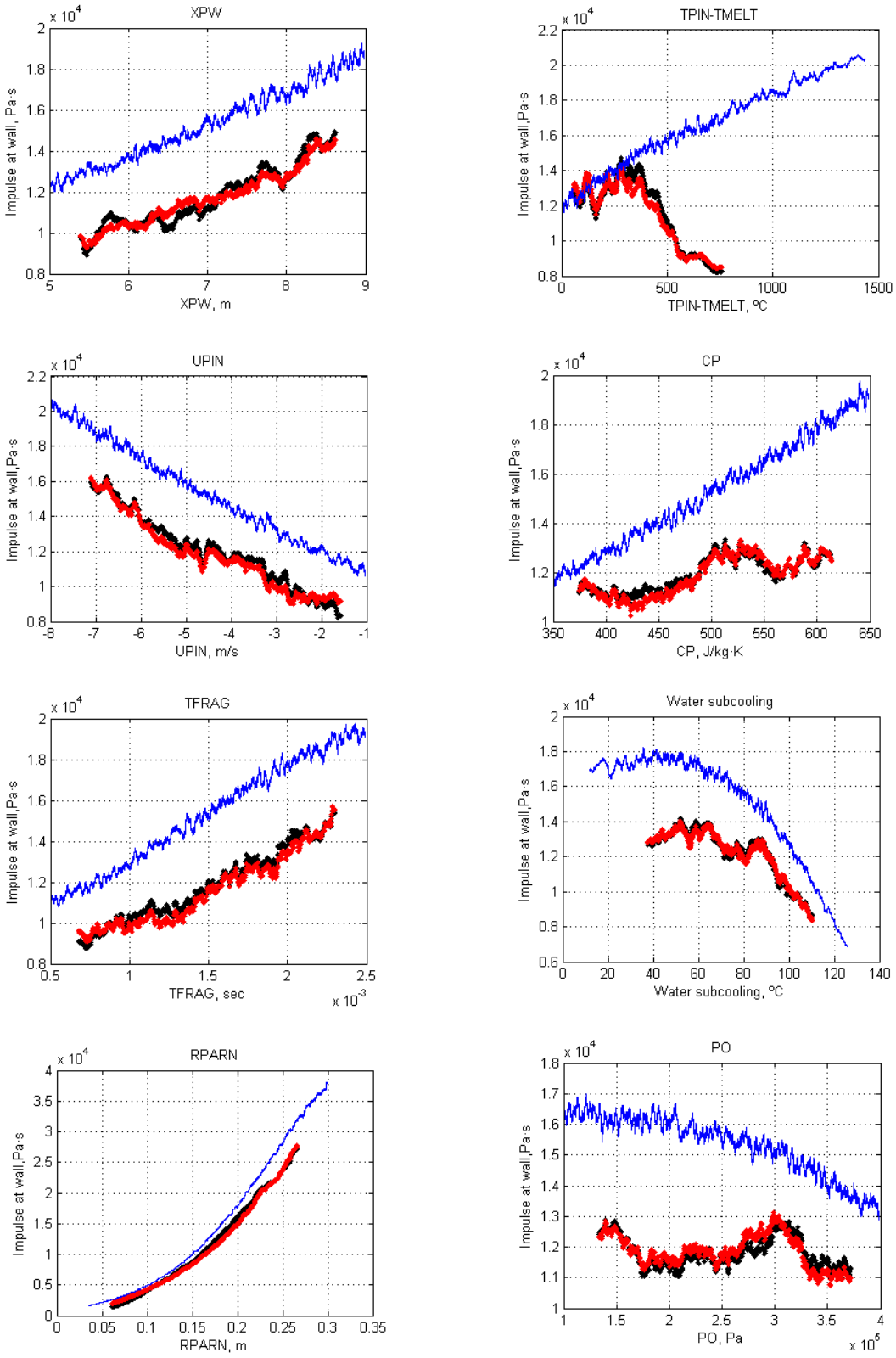

Figure 21: Parametric comparison of SM and FM predicted impulses at the wall (blue – SM with random input; red – SM with training input; black – TEXAS with training input)

5.6 Approach to risk assessment: definition of failure domains and their interpretation

The risk is defined as a triplet [16]: scenario, its frequency and probability of failure. The triplet introduces a natural separation between epistemic (failure probability) and aleatory (scenario frequency) uncertainties.

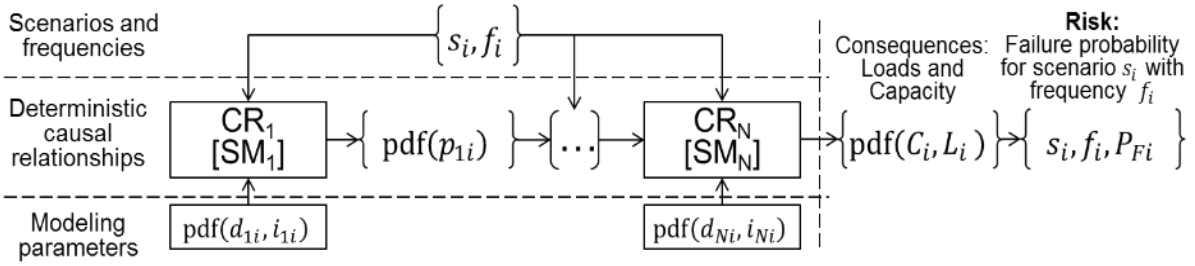

Figure 74. Parameters in the ROAAM+ framework [31].

For each plant damage state $\{D_i\}$ there is a set of respective scenarios $\{s_{ij}\}$ characterized by frequencies (f_{ij}). For the sake of brevity, in the future we will omit second index when referring to scenarios (s_i) and their probabilities (f_i) considering them as a whole set of all scenarios relevant to all initial damage states. Scenarios (s_i) introduce specific combinations of initial and boundary conditions for causal relationships (CR_k) and structure of the probabilistic framework (Figure 74). A set of surrogate models (SM_k) is used to approximate the CR_k. In the multistage framework output of CR_k is determined as multidimensional probability density function $\text{pdf}(p_{ki})$ that provides initial input parameters for the next model CR_{k+1}. Timing is explicitly included as one of the p_{ki} parameters. Epistemic uncertainty in prediction of the failure probability is introduced by multidimensional probability density function $\text{pdf}(d_{ki}, i_{ki})$ of intangible (i_{ki}) and deterministic (d_{ki}) modeling parameters. These distributions determine the probability of containment failure (P_{Fi}) for scenario (s_i).

Steam explosion model is the last model in the framework (CR_N) and has input parameters that are determined by

(i) modelling at the previous stages of the accident progression ($p_{N-1,i}$) (e.g. melt release conditions such as jet diameter, release velocity, melt temperature etc., melt properties: density, thermal conductivity, solidification temperature), or

(ii) stochastic accident scenarios (s_i) (e.g. water pool depth, temperature, system pressure etc. at the time of melt release).

(iii) Internal model parameters (that are determined neither by the previous models nor by accident scenarios) and are referred as *deterministic* (d_{Ni}) parameters if

information about probability distribution is available *and intangible* (i_{Ni}) *parameters,* if such information is not available. In case of the steam explosion model the intangible parameters are: time of fine fragmentation and coefficient of proportionality in the equation for the melt fine fragmentation rate.

Note that separation of parameters into *scenario* (s_i), *initial input parameters* ($p_{k,i}$), *deterministic* (d_{ki}) *and intangible* (i_{ki}) modelling parameters, depends on the formulation of the problem and respective structure of the framework. Some parameters, for example, water level, can be treated as a *scenario parameter* (i.e. conditional failure probability will be estimated for given water level in specific scenario), modelling parameter (e.g. obtained by a containment code and characterised by a range and a distribution), deterministic modelling parameter (defined by range and distribution) or intangible parameter (defined only by its range).

The calculation of the conditional failure probability is performed in the space of the scenario parameters. For each distribution of the input parameters, output distribution of the steam explosion load is produced. Containment fragility is currently taken as a fixed value. Juxtaposition of the load and fragility allows estimation of the conditional failure probability. Note that arbitrary scale of probability is employed in ROAAM [65]. If the conditional failure probability exceeds 0.001, then the failure cannot be excluded as physically unreasonable and mitigation strategy for a considered scenario is assumed to be ineffective.

Probability distribution of an intangible parameter is not known. In order to demonstrate both (i) the effectiveness of the mitigation strategy and (ii) the effect of the distributions of deterministic and intangible parameters we apply the following approach. For every point in the space of initial input and scenario parameters we estimate failure probability for different possible distributions of *deterministic and intangible parameters*. We introduce additional parameters that define those distributions. In such way for every point in the space of initial input and scenario parameters we estimate a distribution of the conditional failure probability. If conditional failure probability is above/below the user defined threshold only for a small fraction of possible distributions, e.g. 5%, we consider that such scenario belongs to the failure/safe domain respectively and is not sensitive to the distributions. If percentile of the distributions becomes larger, conclusions about success or failure of the mitigation strategy are sensitive to the knowledge about the distributions.

Failure domain maps are plotted in the space of initial input and scenario parameters. Failure and success domains are colored in red and green respectively. Example of the failure domain and complimentary cumulative distribution functions (CCDFs) of the conditional failure probability are provided in the Figure 75. In-depth discussion of the ROAAM+ methodology for risk analysis is provided in [31].

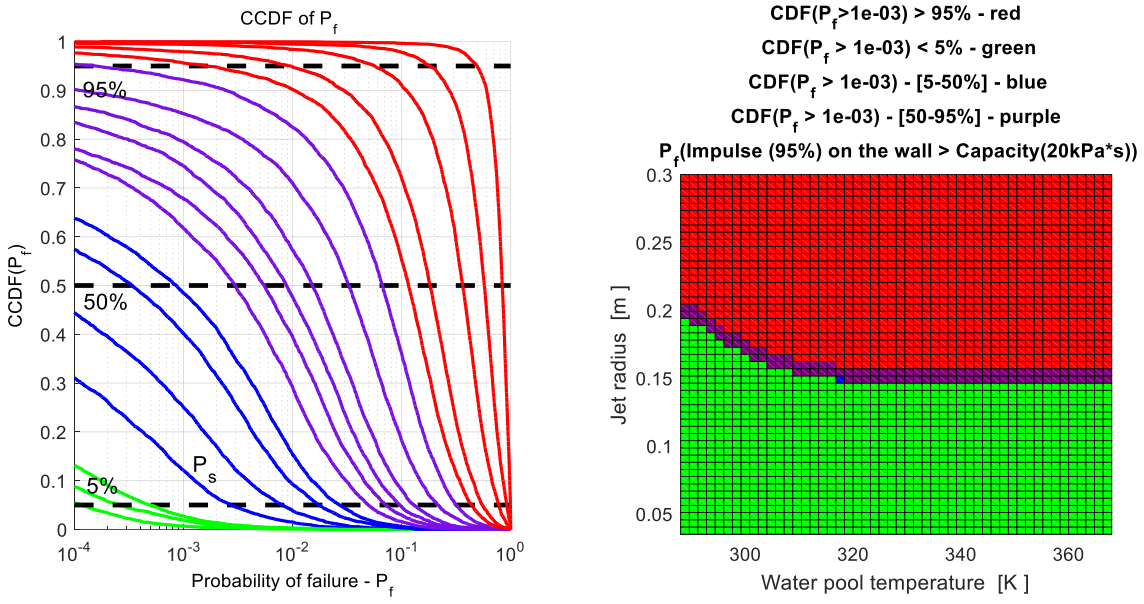

A b

Figure 75: Example of the CCDFs of failure probability (a) taken from the first vertical line in failure domain map (b).

5.7 Failure Domain in SEIM SM Input Parameters

Results of SEIM reverse analysis are provided in Figure 76 for three different modes of containment failure and two groups of scenario parameters. The data confirms the results of the sensitivity analysis that jet radius is the most influential parameter dominating failure domain boundaries; other parameters such as water pool depth (XPW) and water temperature (TLO) demonstrate much smaller effect on the failure domain.

Comparison of the failure domain for 20 and 50 kPa*s suggest that reinforcement of the hatch-door has significant positive effect on the failure domain. Safe domain estimated for the containment base is smaller than that for the pedestal wall, even though assumed fragility limit for the containment base is higher (80 kPa*s). This is due to the fact that statistically the

magnitude of the explosion impulses at the containment base is higher than at the pedestal wall.

As it follows from the obtained results the “safe region” does not exceed about 1/3 of the failure domain map. In case of 20 kPa*s fragility limit (assumed to be an order of magnitude for a non-reinforced hatch-door) the safe domain is negligible. This means that unless there is a mechanism which can limit the size of the jet dimeter to

- ~70mm (initial size of the IGT) for 20 kPa*s fragility limit on the wall;
- ~180mm for 50 kPa*s limit on the wall;
- ~140mm (inial size of CRGT) for 80 kPa*s fragility limit at the base

it is not possible to demonstrate that fragility limits in case of containments with non-reinforced door will not be exceeded (given uncertainties in the steam explosion impulse estimations).

Potential source of such limiting factors are the accident scenarios and phenomena at the previous stages of the accident progression.

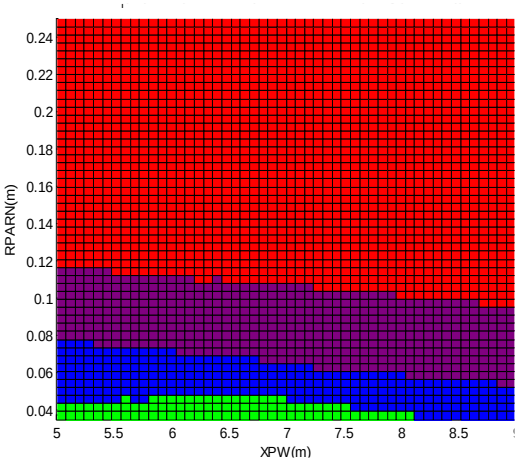

a (20 kPa*s)

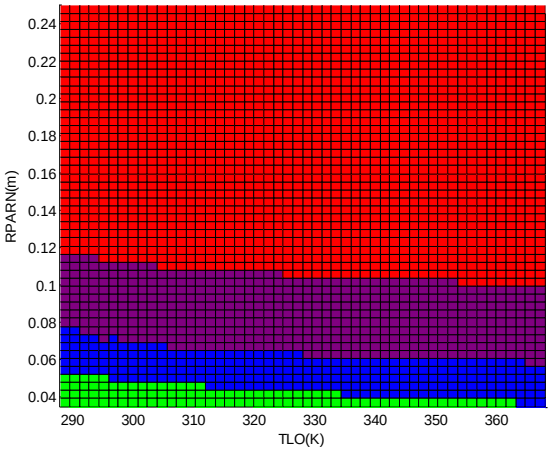

f (20 kPa*s)

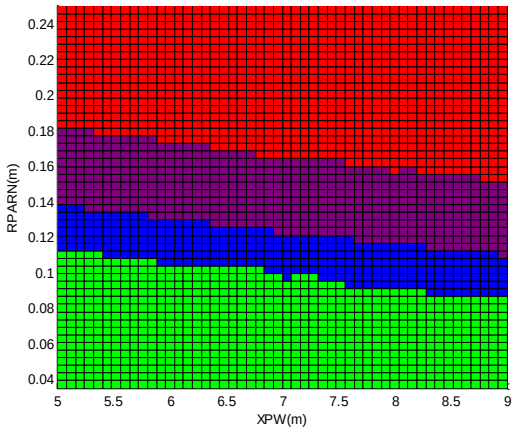

b (50 kPa*s)

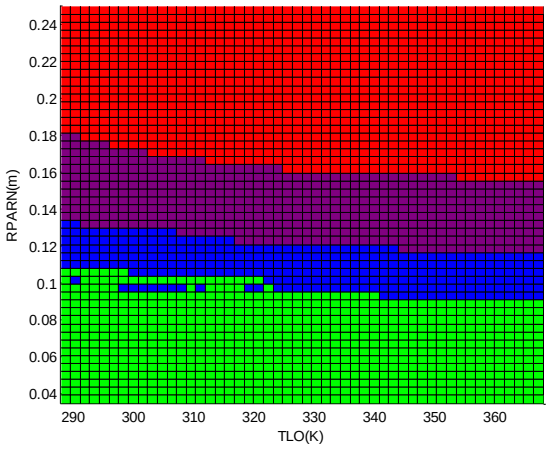

g (50 kPa*s)

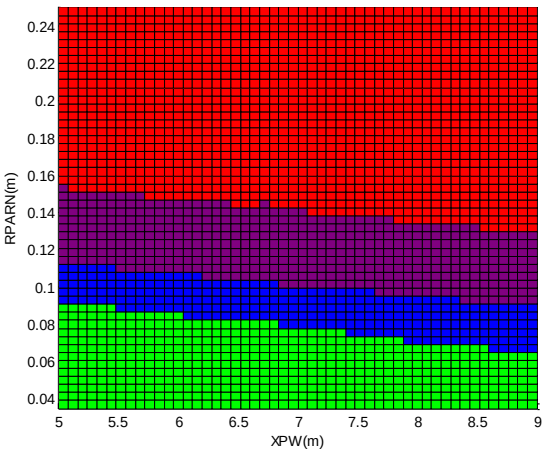

c (80 kPa*s)

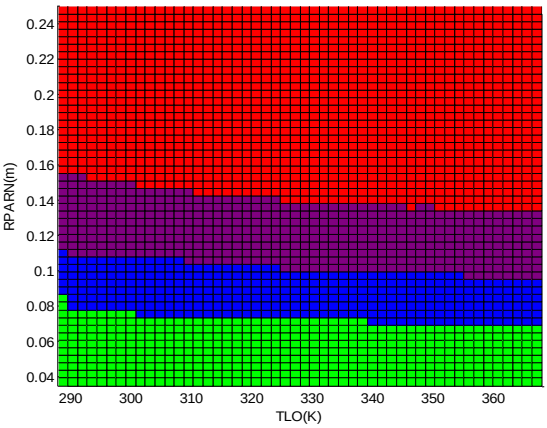

h (80 kPa*s)

Figure 76. SEIM Failure domains for two groups of scenario parameters RPARN vs XPW (a-c) and RPARN vs TLO (f-h) and different fragility limits: on the wall (a,b,f,g) and at the base (c,h).

5.8 Summary and Outlook

The goal of this work was development of a fast numerical tool (surrogate model) that can be used for the assessment of the risk of containment failure in Nordic type BWR due to steam explosion. Three primary tasks have been accomplished: (i) development of the Full Model, (ii) generation of the Full Model solution database, and (iii) development of the surrogate model.

We utilized TEXAS-V to build the Full Model (FM) for the assessment of the steam explosion energetics in Nordic type BWRs and combine it with a simplified impulse propagation approach.

Extensive simulations using the TEXAS-V revealed that explosion impulse is a chaotic function of the triggering time – phenomena that has an important impact on both risk analysis and interpretation of experimental results. Specifically, it was found that explosion impulse can change 50 times within just a 110 ms time window. It is instructive to note that in the steam explosion experiments the aleatory uncertainty due to the influence of the triggering time is also expected to be significant. Proper statistical treatment with multiple repletion of the tests at the same melt release conditions is necessary in order to measure the effects of the other experimental parameters.

We have further, implemented an approach to encompass the chaotic nature of the explosion impulse by characterizing its statistical distribution. The objective is double fold, first it imposes well-posedness on the response function and second allows characterization of the explosion impulse in terms of confidence intervals and confidence levels – approach highly beneficial for risk assessment.

After ensuring model physical well-posedness we proceed with detailed sensitivity study followed by parameter screening leaving 13 most important parameters. The model was then sampled to generate a large database of solutions (1500 premixing sets comprised of 455K of premixing/explosion calculations). Numerically failed calculations were filtered from the database. Physical sensibility of the FM model response to variation of the input parameters

was verified in a statistical sense. The database was used for the development of the surrogate model. The surrogate model was implemented using ANN. SM and FM were then systematically compared and results were found to be in a satisfactory agreement.

The SM was then integrated in to the SEIM framework and failure domains were constructed for a set of melt release scenarios. The results suggest that in cases with non-reinforced hatch door there are high chances of containment failure even for small jet release diameters (Ø0.08 m). However, if hatch doors are reinforced to the level of the pedestal wall (50 kPa·s) failure of the containment becomes dependent on the melt release scenario: failure is unlikely when jet release diameter is below 0.2 m.

Future tasks include:

- Melt releases with multiple jets.
- Multiple consecutive steam explosions.
- Effect of crust formation around melt particles on the energetics of the steam explosions.
- Generation of non-condensable gases during premixing.
- Validation of the explosion propagation model.
- Improvement and verification of the impulse propagation model.
- Development of an SM capable to predict impulse value given desired confidence level not relying on any assumptions about actual impulse distribution.

6 Summary and Outlook

This work is motivated by the severe accident management strategy adopted in Nordic type BWRs. The goal of the project is to reduce uncertainties in assessment of (i) debris bed properties and coolability, (ii) steam explosion impact. In the experimental part of the project we investigate key physical phenomena of the debris bed formation and coolability, and producing experimental data for validation of simulation tools. Analytical approaches are employed to assess the uncertainties in modelling of debris bed coolability and steam explosion impact.

Analysis of debris bed coolability

In this work we further develop DECOSIM code to address (i) debris bed coolability in post-dryout regime; (ii) particulate debris spreading with possible feedbacks between dryout and spreading effectiveness. An analytical model is proposed based on the analysis of DECOSIM calculations for prediction of the maximum temperature of the debris if the size of the dry zone is known. Excellent agreement with the DECOSIM data is demonstrated.

The DECOSIM was validated against new COOLOCE data for different spatial configurations: (i) cylindrical debris bed with open side walls (COOLOCE-10), (ii) conical bed on a cylindrical base (COOLOCE-12). The dependence of DHF on system pressure from COOLOCE experiments can be reproduced quite accurately if either the effective particle diameter or debris bed porosity is increased, which is consistent with MEWA simulation results reported in [59]. It is interesting to note that, despite the difficulty in predicting the absolute values of dryout heat flux due to high sensitivity of results to the values of debris bed porosity and particle diameter, the relative improvement of debris bed coolability for conical debris bed in comparison with flat (or cylindrical, behaving effectively as a flat) debris bed is captured quite well in the simulations. Further work would be necessary in order to utilize recently produced COOLOCE data for validation of the DECOSIM.

An analytical model based on observations of the solutions for the structure of the dry zone has been proposed in order to predict the maximum temperature reached at the top boundary of the debris bed. Comparison of the DECOSIM simulations carried out for conical and mound-shaped debris beds suggest that the analytical formula predicts quite well the maximum temperature rise in the debris bed. Importantly, the results are practically

independent of debris bed shape and involve only few parameters, which reduce the uncertainties in the estimation of post-dryout behavior of debris beds. Further development and verification of the computationally efficient and sufficiently accurate simplified (surrogate) models would be necessary in order to employ the models in the uncertainty and risk analysis for different plant accident scenario conditions.

Empirical closures obtained in PDS-C experiments were implemented in DECOSIM in order to enable simulations of debris beds with evolving (due to particle spreading) geometry. Implementation of particle spreading algorithm in DECOSIM was verified against the 1D numerical model which solves the equation for debris bed height which is, essentially, a debris mass conservation equation. Good agreement between the maximum debris bed heights as functions of time calculated by DECOSIM and that from 1D model was demonstrated, as well as the shapes of debris bed at selected times were found to practically coincide. Few preliminary fully coupled DECOSIM simulations of debris bed were performed in which the superficial gas velocity and gas parameters involved in the correlation for the lateral particle flux were obtained from the two-phase flow model. Simulations were carried out and maximum temperatures of solid material were compared in the cases with and without particle spreading. Results suggest that spreading can enhance coolability for particles larger than 1.5 mm. Further studies are necessary in order to quantify the effect of the dry zone on debris bed spreading and coolability.

Investigation of particulate debris spreading

Boiling and two-phase flow inside the bed is a source of mechanical energy which can help to spread the debris bed by so called “self-leveling” phenomenon. The goal of this work is to quantify time scale for particulate debris spreading. Experimental studies have been carried out in PDS-C facility with air injection from the bottom of the debris bed. Based on the experimental data an analytical approach is developed by KTH to simulate particulate debris spreading.

Previously exploratory tests were carried out in PDS facilities in order to identify governing phenomena of particulate debris spreading. Also we addressed potential effect of the mockups of the COOLOCE heaters and TCs on the particle self-leveling process. Results suggested that there is no significant influence on the self-leveling for the considered ranges of the air injection velocities [38].

In this work a set of PDS-C experiments has been carried out with different stainless steel particles in order to quantify particle flow rate in debris bed self-levelling phenomenon. A scaling approach for particulate debris spreading has been proposed. Application of proposed scaling approach to generalization of the PDS-C tests results in dense clustering of the non-dimensional data suggesting that the most important physical phenomena are captured properly in the approach. Based on the scaling and on the PDS-C experimental data a universal semi-empirical closure has been developed for prediction of the debris mass flux as a function of local slope angle, gas flowrate, and debris bed properties. More tests would be necessary with particles made of different material, mixtures of particles with different sizes and irregular shapes, etc. in order to extend empirical database for validation of the proposed closure.

Analysis of steam explosion in a Nordic BWR containment

In this work we develop an approach for analysis of steam explosion sensitivity to the modeling and scenario parameters using TEXAS code. The approach is based on sampling of the input parameters within selected ranges in order to obtain statistical characteristics of the model response. Preliminary analysis helps to identify the most and the least important parameters. Obtained database of solutions for the impulse and pressure as a function of the TEXAS input parameters is used for development of a computationally efficient surrogate model. Further work is necessary for (i) selection and justification of the parameter ranges and clarification of their potential inter-dependencies; (ii) continuation of the sensitivity study in order to cover remaining cases of melt ejection scenarios; (iii) refinement and generalization of the surrogate model; (iv) development of robust approach to demonstrate failure domain in a multidimensional space of input parameters; (v) development of methodology for grouping and classification of failure scenarios considering the failure domain and interdependences between scenario and input modelled parameters.

7 Nomenclature

Ar_{lg}	Air phase Archimedes number with liquid-buoyed solids, [-]
d_p	Equivolume sphere diameter, [mm]
F_B	Buoyancy force, [N]
F_D	Aerodynamic drag force, [N]
F_{Fr}	Inter-particle friction force, [N]
F_G	Gravity force, [N]
k_{Fr}	Friction coefficient [-]
L	Facility total length, [mm]
Q_g	Non-dimensional superficial gas velocity, [-]
Q_p	Particle mass flow per unit width, $[\mathrm{kg/(m \cdot s)}]$
Q_p^*	Non-dimensional normalized Q_p, [-]
Re_{gmf}	Air Reynolds number at minimum 3-phase Fluidization, [-]
U_g	Superficial gas velocity, [m/s]
U_{mf}	Superficial gas velocity at minimum 3-phase fluidization, [m/s]
	Greek letters
ε	Bed porosity, [-]
μ_g	Air viscosity, [Pa s]
ρ_g	Air density, [kg/m^3]
ρ_l	Liquid density, [kg/m^3]
ρ_p	Solid particle density, [kg/m^3]
θ_{rep}	Repose angle, [degree]
ϕ	Heap slope angle, [degree]
Φ	Normalized slope angle [-]

8 Acknowledgement

The work is carried out with support of the MSWI-APRI-9 project at KTH.

NKS conveys its gratitude to all organizations and persons who by means of financial support or contributions in kind have made the work presented in this report possible.

9 Disclaimer

The views expressed in this document remain the responsibility of the author(s) and do not necessarily reflect those of NKS. In particular, neither NKS nor any other organization or body supporting NKS activities can be held responsible for the material presented in this report.

10 REFERENCES

[1] Adams, B.M., Bauman, L.E., Bohnhoff, W.J., Dalbey, K.R., Ebeida, M.S., Eddy, J.P., Eldred, M.S., Hough, P.D., Hu, K.T., Jakeman, J.D., Swiler, L.P., and Vigil, D.M., "DAKOTA, A Multilevel Parallel Object-Oriented Framework for Design Optimization, Parameter Estimation, Uncertainty Quantification, and Sensitivity Analysis: Version 5.4 User's Manual," Sandia Technical Report SAND2010-2183, December 2009. Updated April 2013.

[2] Alpine Hosokowa supplier of the powerbeads, http://www.alpinehosokawa.com.

[3] Alvarez D. and M. Amblard, “Fuel leveling”, Information Exchange Meeting on Post Accident Debris Cooling, Karlsruhe, July 28-30, (1982).

[4] Basso S., A. Konovalenko and P. Kudinov “Sensitivity and uncertainty analysis for predication of particulate debris bed self-leveling in prototypic SA conditions”, International Congress on Advances in Nuclear Power Plants (ICAPP), Charlotte, USA April 6-9 Paper 14329 (2014).

[5] Basso S., A. Konovalenko and P. Kudinov, "Development of scalable empirical closures for self-leveling of particulate debris bed," in Proceedings of ICAPP-2014, Charlotte NC, USA, Paper 14330, April 6-9, (2014).

[6] Budu A., “Debris Bed Formation at Low Temperature (DEFOR-LT experiment): Coolant flow influence on debris packing,” SARNET mobility research report, Division of Nuclear Power Safety KTH, Stockholm, 2008.

[7] Bürger M., Buck M., Schmidt W., and Widmann W., “Validation and Application of the WABE code: Investigations of Constitutive Laws and 2D effects on Debris Coolability,” Nuclear Engineering and Design, Vol. 236, pp. 2164–2188 (2006).

[8] Cheng S., H. Tagami, H. Yamano, T. Suzuki, Y. Tobita, B. Zhang, T. Marsumoto and K. Morita, “Evaluation of debris bed self-leveling behavior: A simple empirical approach and its validations”, Annals of Nuclear Energy, vol. 63, 188 (2014).

[9] Cheng S., Y. Tanaka, Y. Gondai, T. Kai, B. Zhang, T. Matsumoto, K. Morita, K. Fukuda, H. Yamano, T. Suzuki and Y. Tobita, “Experimental Studies and Emipirical Models for the Transient Self-Leveling Behavior in Debris Bed”, Journal of Nuclear Science and Technology, vol. 48, 10, 1327 (2011).

[10] Dombrovsky L.A., Davydov M.V., Kudinov P., “Thermal radiation modeling in numerical simulation of melt-coolant interaction,” Comp. Therm. Sci. 1 (1) 2009, pp. 1-35.

[11] Dombrovsky L.A., Davydov M.V., and Kudinov P., Thermal radiation modeling in numerical simulation of melt-coolant interaction, Proc. Int. Symp. Adv. Comput. Heat Transfer (CHT-08), May 11–16, 2008, paper 155.

[12] Ergün S., "Fluid Flow through Packed Columns," Chemical Engineering Progress, Vol. 48, 2, pp. 89-94 (1952).

[13] Eames, I., Gilbertson, M., "Aerated granular flow over a horizontal rigid surface", J. Fluid Mech. 424, 169-195, (2000).

[14] Frid W. and Kudinov P., "Ex-Vessel Melt Coolability Issue in BWRs with Deep Water Pool in Lower Drywell," OECD/NEA MCCI Seminar 2010, Cadarache, France, 15th - 17th November, 2010.

[15] Hu K. and Theofanous, T.G., "On the Measurement and Mechanism of Dryout in Volumetrically Heated Coarse Particle Beds," Int. J. Multiphase Flow, Vol. 17, No. 4, pp. 519–532 (1991).

[16] Kaplan S. and Garrick B. J., "On The Quantitative Definition of Risk," Risk Analysis, 1: pp.11–27, (1981).

[17] Karbojian A., Ma W.M., Kudinov P., Davydov M. and Dinh N., "A scoping study of debris formation in DEFOR experimental facility", 15th International Conference on Nuclear Engineering, Nagoya, Japan, April 22-26, 2007, Paper number ICON15-10620.

[18] Karbojian A., Ma W., Kudinov P., and Dinh T.-N., "A Scoping Study of Debris Bed Formation in the DEFOR Test Facility", Nuclear Engineering and Design, 239, 2009, 1653-1659.

[19] Kim, B.J., "Heat transfer and fluid flow aspect of small-scale single droplet fuel-coolant interaction," 1985, University of Wisconsin-Madison.

[20] Kim E., J. H. Park, M. H. Kim and H. S. Park, "The influence of two-phase flow on pore clogging by fine particle settlement during ex-vessel debris bed formation in severe accident," in Proceedings of the 2014 22nd International Conference on Nuclear Engineering (ICONE22), Prague, Czech Republic, July 7-11, (2014).

[21] Konovalenko A., Basso S., Karbojian A. and Kudinov P., "Experimental and Analytical Study of the Particulate Debris Bed Self-leveling," Proceedings of The 9th International Topical Meeting on Nuclear Thermal-Hydraulics, Operation and Safety (NUTHOS-9), Kaohsiung, Taiwan, September 9-13, N9P0305, 2012.

[22] Konovalenko A., Basso S., and Kudinov P. "Experiments and Characterization of the Two-Phase Flow Driven Particulate Debris Spreading in the Pool," The 10th

International Topical Meeting on Nuclear Thermal-Hydraulics, Operation and Safety (NUTHOS-10), Okinawa, Japan, December 14-18, 2014, Paper 1257, 2014.

[23] Konovalenko A., S. Basso and P. Kudinov, S. E. Yakush, “Experimental investigation of particulate debris spreading in a pool”, accepted for publication in NED, paper NED-D-15-00556R1. 2016.

[24] Kolev N., Multiphase Flow Dynamics, Vol. 2, Ch. 2, Springer, Berlin, Heidelberg, NY (2005).

[25] Kubasch J. H., ”Bubble Hydrodynamics in Large Pools,” Swiss Federal Institute of Technology, Zurich, PhD thesis, (2001).

[26] Kudinov P. and Davydov M., “Approach to Prediction of Melt Debris Agglomeration Modes in a LWR Severe Accident,” Proceedings of ISAMM-2009, Böttstein, Switzerland, October 26 - 28, 2009.

[27] Kudinov P. and Davydov M., “Development of Ex-Vessel Debris Agglomeration Mode Map for a LWR Severe Accident Conditions,” Proceedings of the 17th International Conference on Nuclear Engineering, July 12-16, 2009, Brussels, Belgium, Paper ICONE17-75080.

[28] Kudinov P. and Davydov M., “Development and Validation of the Approach to Prediction of Mass Fraction of Agglomerated Debris,” The 8th International Topical Meeting on Nuclear Thermal-Hydraulics, Operation and Safety (NUTHOS-8), Shanghai, China, October 10-14, N8P0298, 2010.

[29] Kudinov P. and Dinh T.-N., “A Computational Study of Debris Bed Formation,” ANS Transactions, 2008, paper 193463.

[30] Kudinov P. and Dinh T.-N., “An analytical study of mechanisms that govern debris packing in a LWR severe accident”, The 12th International Topical Meeting on Nuclear Reactor Thermal Hydraulics (NURETH-12), Sheraton Station Square, Pittsburgh, Pennsylvania, U.S.A. September 30-October 4, 2007. Paper 247.

[31] Kudinov P., Galushin S., Yakush S., Villanueva W., Phung V.-A., Grishchenko D., Dinh N., “A Framework for Assessment of Severe Accident Management Effectiveness in Nordic BWR Plants,” Probabilistic Safety Assessment and Management PSAM 12, June 22-27, 2014, Honolulu, Hawaii, Paper 154, 2014.

[32] Kudinov P., Karbojian A., Ma W.M., Davydov M., and Dinh T.-N., “A Study of Ex-Vessel Debris Formation in a LWR Severe Accident”, Proceedings of ICAPP 2007, Nice, France, May 13-18, 2007, Paper 7512.

[33] Kudinov P., Karbojian A., Ma W., and Dinh T.-N. “The DEFOR-S Experimental Study of Debris Formation with Corium Simulant Materials,” Nuclear Technology, 170(1), April 2010, pp. 219-230, 2010.

[34] Kudinov, P., Karbojian, Tran, C.-T., Villanueva, W., 2013. Agglomeration and size distribution of debris in DEFOR-A experiments with Bi2O3-WO3 corium simulant melt. Nuclear Engineering and Design, 263, pp. 284-295.

[35] Kudinov P., Karbojian A., Tran C.-T., “Experimental Investigation of Melt Debris Agglomeration with High Melting Temperature Simulant Materials,” Proceedings of ISAMM-2009, Böttstein, Switzerland, October 26 - 28, 2009.

[36] Kudinov P., Karbojian A., Tran C.-T., Villanueva W., “The DEFOR-A Experiment on Fraction of Agglomerated Debris as a Function of Water Pool Depth,” The 8th International Topical Meeting on Nuclear Thermal-Hydraulics, Operation and Safety (NUTHOS-8), Shanghai, China, October 10-14, N8P0296, 2010.

[37] Kudinov P., Karbojian A., Ma W.M., and Dinh T.-N., “An experimental study on debris formation with corium simulant materials,” Proc. ICAPP’08, Anaheim, CA USA, June 8–12, 2008, paper 8390.

[38] Kudinov P., Konovalenko A., Grishchenko D., Yakush S., Basso S., Lubchenko N., Karbojian A., “Investigation of debris bed formation, spreading and coolability.” NKS-DECOSE Project Report NKS-287, 88p., June 2013.

[39] Kudinov P., Konovalenko A., Grishchenko D., Yakush S., Basso S., Lubchenko N., Karbojian A., “Analysis of Debris Bed Formation, Spreading, Coolability, and Steam Explosion in Nordic BWRs,” NKS-DECOSE Project, Report NKS-317, 177p., 2014.

[40] Kudinov P., Konovalenko A., Grishchenko D., Yakush S., Basso S., Lubchenko N., Karbojian A., “Analysis of Debris Bed Formation, Spreading, Coolability, and Steam Explosion in Nordic BWRs,” NKS-DECOSE Project, Report NKS-346, 125p., 2015.

[41] Kudinov P. and Kudinova V., “Influence of Water Subcooling on Fracture of Melt Debris Particle,” ANS Transactions, 2009, paper 210646.

[42] Kudinov P., Ma W.M., Tran C.-T., Hansson R., Karbojian A., Dinh T.-N. “Multiscale Phenomena of Severe Accident,” NKS-R and NKS-B Joint Summary Seminar, Armémuseum, Stockholm, 26th - 27th March 2009.

[43] Kudinov P., “Decomposition, Validation and Synthesis in Multiscale Problems of Severe Accident Analysis,” Verification and Validation for Nuclear Systems Analysis Workshop, Center for Higher Education, Idaho Falls, ID, July 21 - July 25, 2008.

[44] Kudinov P., Kudinova V., and Dinh T.-N., “Molten Oxidic Particle Fracture during Quenching in Water,” 7th International Conference on Multiphase Flow ICMF 2010, Tampa, FL USA, May 30-June 4, 2010.

[45] Lucas A, Arnaldos J, Casal J, Puigjaner L, “Improved equation for the calculation of minimum fluidization velocity”, Ind Eng Chem Process Des Dev, 25, 426-429 (1986).

[46] Morris M. D., “Factorial sampling plans for preliminary computational experiments,” Technometrics, Vol. 33, No. 2, 1991, pp. 161–174.

[47] Pilch, M., “Acceleration induced fragmentation of liquid drops,” 1981, University of Virginia.

[48] Reed A.W., “The Effect of Channelling on the Dryout of Heated Particulate Beds Immersed in a Liquid Pool,” Ph.D. Thesis, Massachusetts Institute of Technology, Cambridge, 1982.

[49] Robinson D. and S. Friedman, “Observations of the effects of particle shape and particle size distribution on avalanching of granular media”, Physica A: Statistical Mechanics and its Applications, vol. 311, 1, 97 (2002).

[50] Saltelli A., Tarantola S., Campolongo F., Ratto M., Sensitivity Analysis in Practice. John Wiley & Sons, Ltd, 2004, 94 p.

[51] Schmidt W., “Interfacial drag of two-phase flow in porous media,” Int. J. Multiphase Flow, Vol. 33, pp. 638–657 (2007).

[52] Shamsuzzaman M., B. Zhang, T. Horie, F. Fuke, T. Matsumoto, K. Morita, H. Tagami, T. Suzuki and Y. Tobita, "Numerical study on sedimentation behavior of solid particles used as simulant fuel debris," Journal of Nuclear Science and Technology, vol. 51, no. 5, pp. 681-699, (2014).

[53] Sudha A. Jasmin, S. S. Murthy, M. Kumaresan, G. Lydia, B. K. Nashine and P. Chellapandi, "Experimental analysis of heaping and self-levelling phenomena in core debris using lead spheres," Experimental Thermal and Fluid Science, vol. 68, pp. 239-246, (2015).

[54] Takasuo E., Kinnunen T. Pankakoski P.H., Holmström S., “The COOLOCE particle bed coolability experiments with a cylindrical geometry: Test series 3–5,” Research Report VTT-R-07099-11. Espoo, 2011. 27 p.

[55] Takasuo E., Kinnunen T. Pankakoski P.H., Holmström S., “The COOLOCE particle bed coolability experiments with a conical geometry: Test series 6–7,” Research Report VTT-R-07097-11. Espoo, 2011. 26 p.

[56] Takasuo E., Holmström S., Kinnunen T., and Pankakoski P.H., "The COOLOCE experiments investigating the dryout power in debris beds of heap-like and cylindrical geometries," Nuclear Engineering and Design 250 (2012), p. 687-700.

[57] Takasuo E., Kinnunen T., Lehtikuusi, T., and Holmström S., "COOLOCE coolability experiments with a cylindrical debris bed and lateral flooding: COOLOCE-10," Research Report VTT-R-00463-13. Espoo, 2013. 19 p.

[58] Takasuo E., Kinnunen T., Lehtikuusi, T., and Holmström S., "COOLOCE-12 debris bed coolability experiment: cone on a cylindrical base," Research Report VTT-R-07967-13. Espoo, 21 p.

[59] Takasuo E., "Debris Coolability Simulations with Different Particle Materials and Comparisons to COOLOCE Experiments," VTT report VTT0R-00257-13 (2013).

[60] Takasuo E., Kinnunen T., Lehtikuusi, T., and Holmström S., "COOLOCE debris bed coolability experiments with an agglomerate simulant: Test series 11," Research Report VTT-R-03316-13. Espoo, 28 p.

[61] Takasuo E., Kinnunen T., Pankkoski H. and Holmström S., "Description of the COOLOCE test facility – Conical particle bed", VTT report VTT-R-08956-10 (2010).

[62] Takasuo E., Kinnunen T., Pankkoski H. and Holmström S., reports VTT-R-07097-11 and VTT-R-02427-11 on experiments on coolability of conical particle bed, VTT (2011).

[63] Tang, J., "Modeling of the complete process of one-dimensional vapor explosions," 1993, University of Wisconsin-Madison.

[64] Thakre S., Ma W., Kudinov P., and Bechta S., "Study on Effective Particle Diameters and Coolability of Particulate Beds Packed with Irregular Multi-size Particles," APRI-8, NKS-DECOSE Project Report, NKS-288, 2013.

[65] Theofanous, T. G., "On Proper Formulation of Safety Goals and Assessment of Safety Margins for Rare and High-Consequence Hazards," Reliability Engineering and System Safety, 54, pp.243-257, (1996).

[66] Theofanous, T. G. and Dinh, T.-N., "Integration of multiphase Science and Technology with Risk management In Nuclear Power reactors: Application of the Risk-Oriented Accident Analysis Methodology to the Economic, Simplified Boiling Water Reactor Design," Multiphase Science and Technology, V20(2), 2008, Pages 81-211.

[67] Tung, V.X. and Dhir, V.K., "A hydrodynamic model for two-phase flow through porous media," Int. J. Multiphase Flow Vol. 14, No. 1, pp. 47–65 (1988).

[68] Yakush S. and Kudinov P., “Simulation of Ex-Vessel Debris Bed Formation and Coolability in a LWR Severe Accident,” Proceedings of ISAMM-2009, Böttstein, Switzerland, October 26 - 28, 2009.

[69] Yakush S. and Kudinov P., “Transient Phenomena of Ex-vessel Debris Bed Formation in a LWR Severe Accident,” ANS Transactions, 2009, paper 210830.

[70] Yakush S., Kudinov P., and Dinh T.-N., “Modeling of Two-Phase Natural Convection Flows in a Water Pool with a Decay-Heated Debris Bed,” Proc. ICAPP’08, Anaheim, CA USA, June 8–12, 2008, paper 8409.

[71] Yakush S., Kudinov P., and Dinh T.-N., “Multiscale Simulations of Self-organization Phenomena in the Formation and Coolability of Corium Debris Bed,” Proc. The 13th International Topical Meeting on Nuclear Reactor Thermal Hydraulics (NURETH-13), September 27-October 2, 2009. Kanazawa City, Ishikawa Prefecture, Japan, Paper N13P1143.

[72] Yakush S. and Kudinov P., “Effects of Water Pool Subcooling on the Debris Bed Spreading by Coolant Flow,” ICAPP Proc., Paper 11416, 2011.

[73] Yakush S.E., Lubchenko N.T., and Kudinov P., “Surrogate Models for Debris Bed Dryout,” Proc. 15th International Topical Meeting on Nuclear Reactor Thermalhydraulics (NURETH-15), paper NURETH15-278, 16 pp.

[74] Yakush S. and Kudinov P., “A Model for Prediction of Maximum Post-Dryout Temperature in Decay-Heated Debris Bed,” Proceedings of the 22th International Conference on Nuclear Engineering (ICONE-22), Prague, Czech Republic, July 7 –11, Paper 31214 (2014), 11 pp.

[75] Yakush S., Villanueva W., Basso S. and P. Kudinov, “Simulation of In-vessel Debris Bed Coolability and Remelting”, The 10th International Topical Meeting on Nuclear Thermal-Hydraulics, Operation and Safety (NUTHOS-10), Okinawa, Japan, December 14-18 (2014), paper NUTHOS10-1281, 12 pp.

[76] Yakush S., Lubchenko N., and Kudinov P., “Risk-Informed Approach to Debris Bed Coolability Issue,” Proceedings of the 20th International Conference on Nuclear Engineering (ICONE-20), Anaheim, CA, USA, July 30 - August 3, Paper 55186 (2012).

[77] Yang Wen-Ching, “Handbook of Fluidization and Fluid-Particle Systems”, Taylor & Francis Group, ISBN 9780824702595, Chapter 26, p.712, (2003).

[78] Zhang B., T. Harada., D. Hirahara, T. Matsumoto, K. Morita., K. Fukuda, H. Yamano, T. Suzuki, Y. Tobita, ”Self-Leveling Onset Criteria in Debris Beds”, J. Nuclear Science and Technlogy, vol. 47, 384 (2010).

[79] Zhang B., T. Harada., D. Hirahara, T. Matsumoto, K. Morita., K. Fukuda, H. Yamano, T. Suzuki, Y. Tobita, “Experimental investigation on self-leveling behavior in debris beds”, Nuclear Engineering and Design, vol. 241, 1, 366 (2011).

Bibliographic Data Sheet **NKS-370**

Title	Experimental and Analytical Investigations of Debris Bed Formation, Spreading, Coolability, and Steam Explosion in Nordic BWRs
Author(s)	Pavel Kudinov[1], Alexander Konovalenko[1], Dmitry Grishchenko[1], Sergey Yakush[2], Simone Basso[1], Nazar Lubchenko[3], Aram Karbojian[1]
Affiliation(s)	[1]Division of Nuclear Power Safety (NPS), Royal Institute of Technology (KTH), Stockholm [2]Institute for Problems in Mechanics of the Russian Academy of Sciences, Moscow, Russia [3]Massachusetts Institute of Technology, Cambridge, Massachusetts, USA
ISBN	978-87-7893-455-0
Date	June 2016
Project	NKS-R / DECOSE
No. of pages	149
No. of tables	18
No. of illustrations	76
No. of references	79

Abstract
max. 2000 characters

In case of severe accident in Nordic type BWRs core melt is fragmented in a deep water pool. There is uncertainty if formed bed if core debris will be coolable or if energetic steam explosion can threaten containment integrity. The goal of the project is to reduce uncertainties in debris coolability and steam explosion impact.

DECOSIM code has been developed for analysis of porous debris coolability and further validated against COOLOCE data. Debris bed cooling in post-dryout regime was addressed. Analytical models for prediction of the maximum temperature of the debris and relative size of the dry zone as a function of overheating parameter is proposed and validated against DECOSIM simulations. DECOSIM code was extended to in-vessel coolability analysis. The parameter ranges corresponding to coolable and non-coolable configurations were obtained for initially dry and quenched debris configuration.

Scaling approach and universal semi-empirical closure have been developed for prediction of particulate debris spreading using PDS-C tests. The approach has been validated against experimental data with different particle mixtures. The model for prediction of particulate debris spreading was implemented in the DECOSIM code.

An approach for analysis of steam explosion in Nordic BWR and sensitivity of steam explosion impulse to the uncertain modeling and scenario parameters has been proposed. TEXAS-V code is used for analysis. Obtained database of impulses TEXAS is used for development of a computationally efficient surrogate model that can be used in extensive uncertainty analysis.

Key words Nordic BWR, severe accident, debris bed formation, coolability, steam explosion

Available on request from the NKS Secretariat, P.O.Box 49, DK-4000 Roskilde, Denmark.
Phone (+45) 4677 4041, e-mail nks@nks.org, www.nks.org